ABSTRACT

Title of Dissertation:	EXCITON PHOTOPHYSICS IN FLUORESCENT QUANTUM DEFECTS
	Mijin Kim, Doctor of Philosophy, 2018
Dissertation directed by:	Professor YuHuang Wang Department of Chemistry and Biochemistry

Fluorescent quantum defect is an emerging synthetic structure that can be covalently attached to a semiconducting single-walled carbon nanotube. Incorporation of fluorescent quantum defect breaks the symmetry of carbon nanotubes at a defect center, creating new optically allowed, low-lying states in the electronic structure of carbon nanotube. Exciting electronic and optical properties arise from the defects, including the generation of new photoluminescence features, which can be used for applications, such as chemical sensing, bioimaging, and quantum light source. As excitons dominate the optical properties of carbon nanotubes, understanding the exciton photophysics in a defect-tailored carbon nanotube is essential to efficiently harness the emission properties of fluorescent quantum defects.

In this dissertation, I aim to understand the exciton photophysics in fluorescent quantum defects in order to explain the origins and behavior of novel phenomena arising from them. First, the structure-property relationships of fluorescent quantum

defects are discussed; these guide the systematic tuning of defect-induced emission and the binding energy of defect-trapped excitons. Then, the discussion moves to the exciton dynamics at fluorescent quantum defects. Particularly, I describe how the chemical nature of defects or the density of defects influences the thermal detrapping energy of excitons. The exciton-electron interaction at a fluorescent defect is also discussed. Our results suggest that a fluorescent quantum defect colocalizes an exciton and an electron as a tri-charge carrier and the brightening at the defect can be chemically tuned. Finally, I introduce super-resolved, hyperspectral photoluminescence spectroscopy, enabling both direct probing of a single fluorescent defect and the quantitative evaluation of the brightening of dark excitons.

EXCITON PHOTOPHYSICS IN FLUORESCENT QUANTUM DEFECTS

by

Mijin Kim

Dissertation submitted to the Faculty of the Graduate School of the
University of Maryland, College Park, in partial fulfillment
of the requirements for the degree of
Doctor of Philosophy
2018

Advisory Committee:
Professor Wang, YuHuang, Chair
Professor Blough, Neil
Professor Fourkas, John T.
Professor Alexander, Millard H.
Dean's Representative: Professor Ouyang, Min

Acknowledgments

First of all, I would like to express my gratitude to my advisor, Prof. YuHuang Wang for his support in my Ph.D. study. I appreciate giving me an opportunity to work on the exciting research in Wang Research Group. I enjoyed working with all the Wang group members and appreciate their advice and helpful discussion. Especially, I thank Dr. Xiaojian Wu, Dr. Hyejin Kwon, Dr. Lyndsey Scammell, Dr. Alexandra Brozena, and Peng Wang for their help along my Ph.D. I thank Benjamin Barnes and Jacob Fortner for their feedback on my thesis.

I would like to appreciate Prof. Milliard H. Alexander, Prof. John T. Fourkas, Prof. Neil Blough, and Prof. Min Ouyang for serving on my committee and for their support on my research and graduation.

I am grateful to all my collaborators for their work and support. Especially, I thank Prof. Jacek Kłos and Prof. Milliard H. Alexander for their guidance and collaboration in quantum chemical modeling. I thank Dr. Stephen K. Doorn, Dr. Nicolai F. Hartmann, and Dr. Xiaowei He for the lifetime studies. I thank Dr. Ao Geyou and Dr. Ming Zheng for the preparation of high-purity carbon nanotube samples. I thank Prof. Laurent Cognet, Dr. Daniel Heller, and Prof. Matteo Pasquali for the collaborations on carbon nanotube imaging.

I thank my friends who are always on my side and make unforgettable memories during the past five years.

Lastly, I would like to thank my family for their unconditional love and supports.

Table of Contents

List of Tables

List of Figures

List of Abbreviations

0D: Zero-dimensional
1D: One-dimensional
2D: Two-dimensional
3D: Three-dimensional
MWCNT: Multi-walled carbon nanotube
SWCNT: Single-walled carbon nanotube
PL: Photoluminescence
UV: Ultraviolet
vis: Visible
NIR: Near-infrared
OD: Optical density
FWHM: Full width at half maximum
DOC: Sodium deoxycholate
SDS: Sodium dodecyl sulfate
SDBS: Sodium dodecylbenzenesulfonate
ATP: Polymer aqueous two-phase separation
DZ: Diazonium salts
DZE: Diazoether
DFT: Density functional theory
TD-DFT: Time-dependent density functional theory
PS: Polystyrene
NA: Numerical aperture
RWI: Read while integrate mode
ROI: Region of interest

1 Introduction

Carbon is one of the most abundant and stable elements in the world. The bonding configuration and crystal structure of carbons produce various allotropes, including diamond, graphite, graphene, and carbon nanotube. Among these carbon allotropes, carbon nanotube has peculiar properties, which arise from its one-dimensional (1D) structure and the hexagonal configuration of sp^2 carbons. Since the discovery of hollow graphitic carbon fibers by Radushkevich and Lukyanovich in 1952,[1] researchers have been extensively investigating carbon nanotubes to understand the material properties. 39 years later, Iijima revealed the molecular structure of carbon nanotubes as multilayer graphitic tubular structures using electron microscopy.[2] The multi-walled carbon nanotube is analogous to graphite in terms of the electrical and electronic properties due to the interactions between inner and outer walls in the nanotube. Thus, the early stage of carbon nanotube research was primarily related to the structural singularity, for example, high mechanical strength, combined with high electrical and thermal conductivity of carbon nanotubes.[2-4]

In 1993, the NEC and IBM groups discovered the first synthesis processes for single-walled carbon nanotubes (SWCNTs), which can be described as a single layer of graphene, rolled up in a helical fashion.[5-6] This discovery has greatly expanded the field of nanoscience by enabling investigation of the fundamental properties and applications of carbon nanotubes. The interest in this new material is primarily due to the unique potential of SWCNTs in exploring the intriguing properties of quasi-1D materials. For example, metallic SWCNTs exhibit high ballistic electronic conduction

and behave as Luttinger liquids due to their 1D nature.[7] The large binding energy of excitons in semiconducting SWCNTs (two orders of magnitude larger than in 3D semiconductors)[8-9] enables elucidation at excitonic properties in 1D system through near-infrared photoluminescence (NIR PL) spectroscopy at room temperature.[10] Furthermore, the optical properties of semiconducting SWCNTs are beneficial for many optoelectronic and biological applications, including their use as a single-photon source[11] and in bioimaging.[12]

Even though the unique electronic and optical properties of semiconducting SWCNTs have been intensively studied, two critical limitations have blocked the broad use of SWCNTs: (1) Low PL quantum yields and (2) Difficulty in chemically controlling their optical properties.

Our group found that fluorescent quantum defects can help mitigate these challenges. Covalently bonding functional groups to semiconducting SWCNTs creates a whole new class of quantum emitters, called fluorescent quantum defects.[13-15] Fluorescent quantum defects introduce new optically allowed quantum states in the electronic structure of SWCNTs. As the defect-induced states reside lower in energy than the intrinsic excitonic states, an exciton can be trapped at a defect site and brightly fluoresce from there. As a result, the defect-incorporated SWCNTs can fluoresce an order of magnitude brighter than unfunctionalized SWCNTs. By varying the functional groups attached to SWCNTs, the defect-induced states are molecularly specific and chemically tunable.

However, complete solutions for the challenges have not been found. For instance, the brightening mechanism of fluorescent quantum defects, the control of

exciton traffic in defect-tailored SWCNTs, and the origin of the defect-induced novel properties are issues requiring investigation.

In my Ph.D., I address these questions by spectroscopic studies as well as quantum chemical modeling of defect tailored SWCNTs. Chapter 2 begins with the introduction of the basic physical and electronic properties of the host material (SWCNT), the definition and features of fluorescent quantum defects, and challenges to be addressed in this thesis.

In this dissertation, I introduce some of my Ph.D. works particularly relevant to exciton photophysics in fluorescent quantum defects. In Chapter 3, I discuss the structure-property relationships of fluorescent quantum defects. This work explores the systematic tuning of defect-induced emission and the electronic coupling between fluorescent quantum defects and SWCNT host by chemically tailoring the functional groups and choice of the host structure. Chapter 4 describes how the exciton dynamics at fluorescent quantum defects can be probed by temperature dependent PL spectroscopy and quantum chemical modeling.

Chapter 5 discusses how the defect system can trap a tri-charge carrier (trion) in a fluorescent quantum defect and how the brightening of the trion can be chemically tuned. Chapter 6 presents a direct measurement of quantum yield of a single fluorescent defect using super-resolved hyperspectral PL spectroscopy and investigates the origin of brightening and the contribution of dark excitons.

Finally, in the conclusion and outlook, I summarize the work discussed in the dissertation and look into the potential underlying fluorescent quantum defects, experiments to be performed, and what novelty we should seek for.

2 Fluorescent Quantum Defects in Single-Walled Carbon Nanotubes

Adapted from a manuscript by Brozena, A.; Kim, M.; Scammell, L.; Wang, Y.

Fluorescent quantum defects are an emergent class of quantum emitters that can be incorporated by covalent attachment of a functional group onto a semiconducting SWCNT. As their name indicates, fluorescent quantum defects exhibit local quantized energy levels that deviate from the extended electronic structure of the SWCNT host. This system is fundamentally important to the study of optical properties in 0D-1D hybrid materials. Furthermore, these types of synthetic quantum defects feature molecularly tunable near-infrared PL emission, and thus hold vast potential for photonic, sensing and optoelectronic applications. In this chapter, I will provide information on our model system, carbon nanotubes, fluorescent quantum defects, and exciton dynamics in defect-tailored SWCNTs.

2.1 Single-Walled Carbon Nanotubes

Graphite is composed of multi-layered hexagonal sp^2 carbons conjugated with π orbitals in a 3D manner (Figure 2-1a). Isolating a single layer of graphite produces graphene. As electrons can move freely on a graphene sheet in any direction, its physical structure and electronic properties represent those of a 2D material (Figure 2-1b). Connecting two lattice points in a single graphene layer creates a SWCNT. A SWCNT is a hollow cylindrical structure with a sp^2 hybridized hexagonal lattice of carbons (Figure 2-1c). Due to their 1D structure, SWCNTs have distinct optical and

electronic properties and can be differentiated from multi-walled carbon nanotubes (MWCNTs). MWCNTs are analogous to 3D graphite in terms of the dimensionality of charge carrier and the absence of strong quantum confinement. Even though the curvature of a SWCNT significantly influences its electronic structure and optical properties, the physical and chemical behavior of graphene can explain some properties of SWCNTs. Here I begin with the physical structure and symmetry of graphene, extend SWCNT properties from those of graphene, and explain how the 1D nature and curvature effects influence the unique properties of SWCNTs.

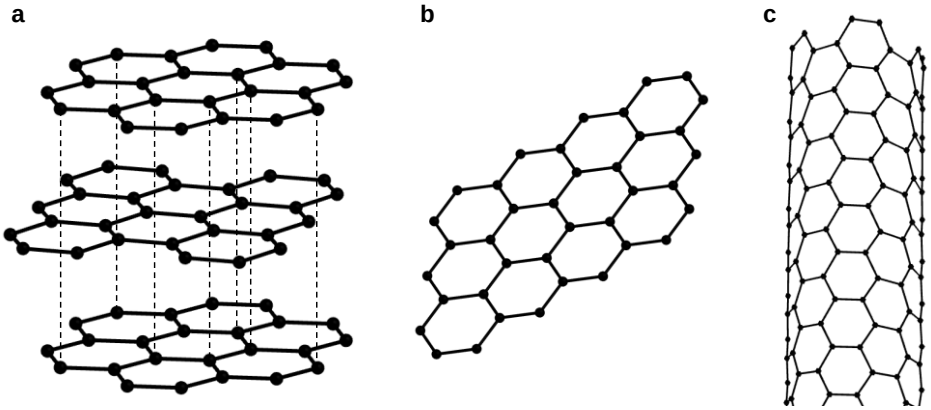

Figure 2-1 Graphical illustration of **a,** graphite, **b,** graphene, and **c,** carbon nanotube.

2.1.1 Physical Structure of Carbon Nanotubes

As graphene is rolled up to form a SWCNT, its diameter, roll-up angle, and enantiomerism can widely vary depending on which two graphene lattice points are connected. The typical diameter range of SWCNTs is 0.6–1.5 nm and the roll-up angle varies from 0 to π/6. This roll-up configuration can be described by the 'chiral vector' $\vec{C}$, a vector wrapped about the SWCNT circumference connecting two carbon atoms, (0,0) and (*n*,*m*) on the graphene sheet. The chiral vector is defined in terms of the primitive lattice vectors of a graphene unit cell, $\overrightarrow{a_1}$ and $\overrightarrow{a_2}$, shown in Figure 2-2: $\vec{C} = n\overrightarrow{a_1} + m\overrightarrow{a_2}$. Here *n* and *m* are integers and the pair of integers (*n*,*m*) denotes the chirality of a particular SWCNT structure. One can derive the diameter and chiral angle from the following correlations with n and m:

$$\text{Diameter, } d = \frac{\sqrt{3}a_{cc}}{\pi}\sqrt{n^2 + nm + m^2} \qquad \text{Eqn. 2-1}$$

$$\text{Chiral angle, } \theta = \tan^{-1}\frac{\sqrt{3}m}{2n+m} \qquad \text{Eqn. 2-2}$$

in which a_{cc} is the distance between two sp^2 carbons in the lattice (1.44Å). To study structure dependence of SWCNTs, (*n*,*m*) chirality is categorized by mod and family. (*n*–*m*) mod categorizes SWCNTs with similar chiral angle but varying diameter. (2*n*+*m*) family groups SWCNTs with similar diameter but varying chiral angle. The structure variation is closely related to the electronic structure of SWCNTs, because this rolling of the graphene sheet imposes specific boundary conditions on the electronic wavefunction in the direction of rolling.

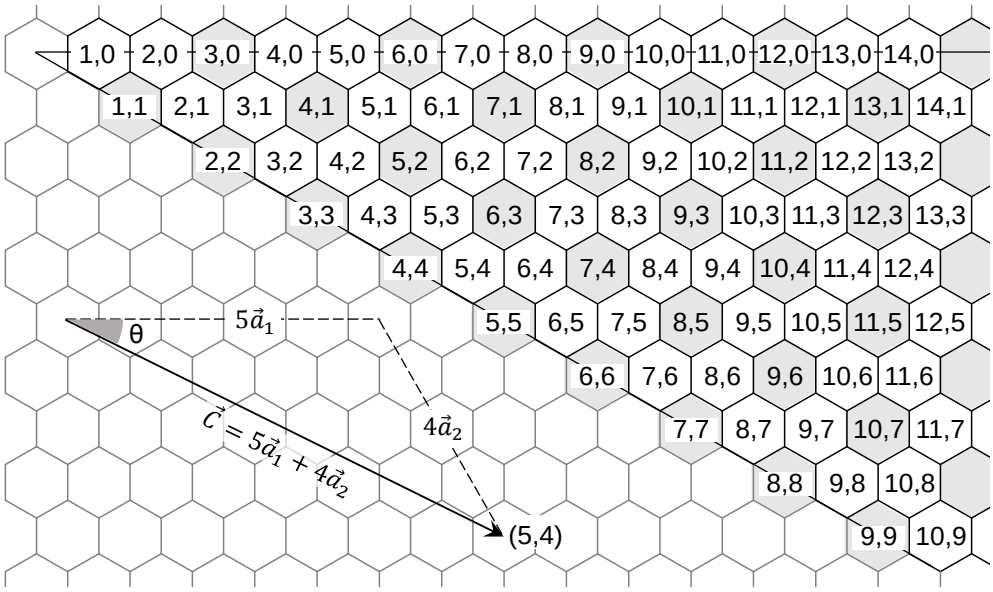

Figure 2-2 Carbon nanotube chiral indices, (*n*,*m*) mapped onto a graphene sheet. Filled lattice represents metallic SWCNTs. All other species are semiconducting SWCNTs. Depending on the chiral vector, $\vec{C}$, the diameter (*d*) and chiral angle (θ) are determined. As a demonstration of chirality, the chiral vector of a (5,4)-SWCNT is shown in the left bottom.

2.1.2 Electronic Structure of Single-Walled Carbon Nanotubes

Because the building block of SWCNTs is graphene, we start from the electronic structures of graphene. Figure 2-3 shows the band structure of graphene near the Fermi level. In the 2D Brillouin zone, the Fermi level lies at the crossing points between an occupied π band and an empty π* band, denoted by K and K'. The π and π* bands have a linear dispersion around the K and K' points, and the valence and conduction bands meet at the Fermi level at the K and K' points. Hence, graphene is a zero-gap semiconductor.

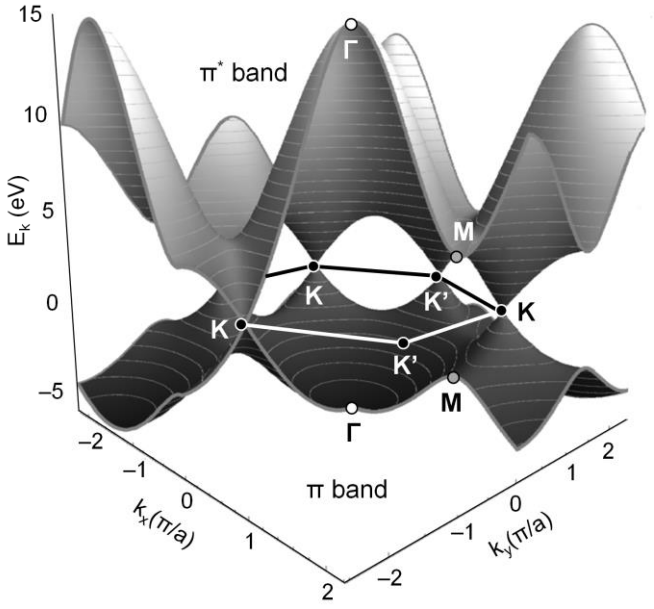

Figure 2-3 Graphene Brillouin zone and electronic energy dispersion.

In contrast, SWCNTs can be metallic or semiconducting with different energy gaps, depending on the diameter and chiral angle. The physics behind this variation of the electronic structures can be explained by trigonal wrapping effects.[16] While the

electron wavevector of parallel direction is continuous, SWCNTs have quantization of the electron wavevector along the circumferential direction because of the periodic boundary conditions on the electron wavefunction. This leads to the formation of energy sub-bands associated with cutting lines of allowed wavevectors (*k* lines), separated from one another by a distance, 2/(diameter of SWCNT)$^{-1}$ and quantized along the chiral vector, shown in Figure 2-4. As the *k* line crosses the K or K' point, it is metallic with linear dispersion whre with a non-vanishing density of states at the Fermi level (Figure 2-5a). If the *k* line does not cut through the K point, the nanotube's dispersion does not cross its apex, which describes a semiconducting SWCNT with a finite band gap (Figure 2-5b). Based on the correlation between the SWCNT chiral angle and the dispersion band structure, it is possible to deduce the electronic structure of SWCNTs. An (*n*,*m*)-SWCNT is metallic, (*n* – *m*) = 3*p*, where *p* is an integer. If (*n* – *m*) is 3*p*+1 or 3*p*+2, the SWCNT is semiconducting with non-zero bandgap at room temperature.

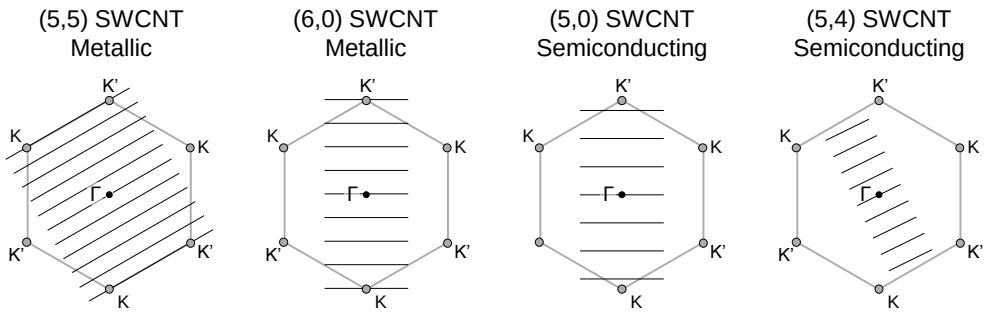

Figure 2-4 Brillouin zone of SWCNTs. The solid cutting lines denote the *k* lines which create sub-bands in SWCNT. The *k* line crossing the K point (left two) results in zero band gap in the density of states therefore a metallic SWCNT. When the *k* lines do not cross the K point (right two), the SWCNT

dispersion band structure has a finite band gap, indicating a semiconducting SWCNT.

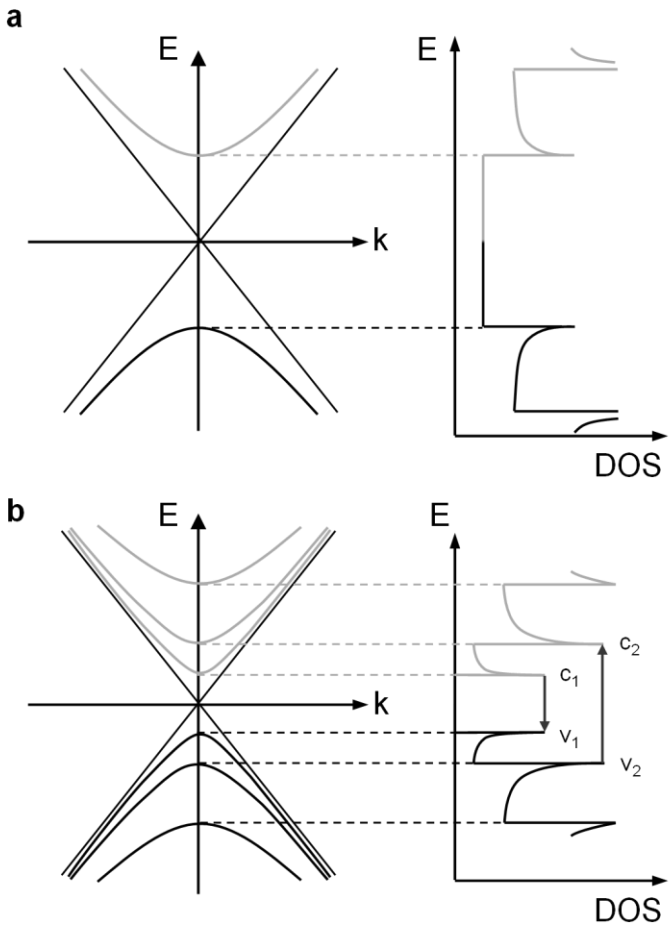

Figure 2-5 Band structures (left) and density of states (right) of **a,** metallic and **b,** semiconducting SWCNTs. The vertical arrows in the density of states of semiconducting SWCNT denote E_{22} excitation ($v_2 \rightarrow c_2$, the second sub-band transition) and E_{11} relaxation ($c_1 \rightarrow v_1$, the first sub-band transition).

In the electronic structure of SWCNTs, one can find singular points, called van Hove singularities (Figure 2-5). Each (*n*,*m*)-SWCNT has its unique set of transition energies between the conduction and the valence bands, which are closely related to van Hove singularities in the density of states. The optical properties of SWCNT mainly arise from a series of allowed E_{ii} transitions, indicating the electronic transitions between *i*th van Hove singularities of conduction and valence bands (Note that the E_{ij} ($i - j \neq 0$) excitation can occur but is optically forbidden due to strong depolarization). E_{ii} optical excitation of semiconducting SWCNTs promotes an electron from the valence band (v_i) to the conduction band (c_i), leaving a hole in valence band (v_i). The photo-excited electron and hole non-radiatively relax to c_1 and v_1 and then radiatively recombine, emitting E_{11} PL.[17]

As the curvature increases, these structure-dependent properties lead to significant changes in the electronic behavior of the SWCNT. However, the simple band structure cannot precisely predict the optical transitions and structure-property relationships of a SWCNT. In particular, a discrepancy between the bandgap energy of a SWCNT and the E_{11} optical transition exists (several hundred meV). The energy discrepancy is due to the fact that the optical transitions in SWCNTs are excitonic in nature. In the next section, I will take into account excitons in order to describe a more accurate picture of the optical properties of SWCNTs.

2.1.3 Excitons in Carbon Nanotubes

The strong quantum confinement in a SWCNT induces an electron in the conduction band and a hole in the valence band to be closely correlated by their Coulomb attraction. The tightly bound electron–hole pair is called an exciton. An exciton carries a quantum of energy and dominates the excited states in SWCNTs. The excitonic picture explains the discrepancy between the band structure model (Section 2.1.2) and experimental measurements of two-photon excitation energies (Figure 2-6).

Wang *et al.*[9] found that the two-photon absorption occur only when the two-photon excitation energies of SWCNTs were substantially greater than the one-photon PL emission energies. If the two-photon excitation energy was the same as the emission energy, none of the SWCNTs fluoresce (Figure 2-6a, red line). This behavior can not be explained by the simple band picture of the optical transitions (Figure 2-5b) and is an evidence of the existence of excitons at room temperature. The discrepancy between the PL emission energy and the excitation energy corresponds to the binding energy of excitons in SWCNTs. The binding energies of SWCNT excitons are unusually large (on the order of several hundred meV, accounting for a significant portion of the ~1 eV nanotube bandgap energy) compared to the exciton binding energies of bulk semiconductors (just a few meV). This enhanced binding energy results from the increased Coulomb interactions in reduced dimensions, as well as from the decreased dielectric screening effects typical of 1D materials.[9]

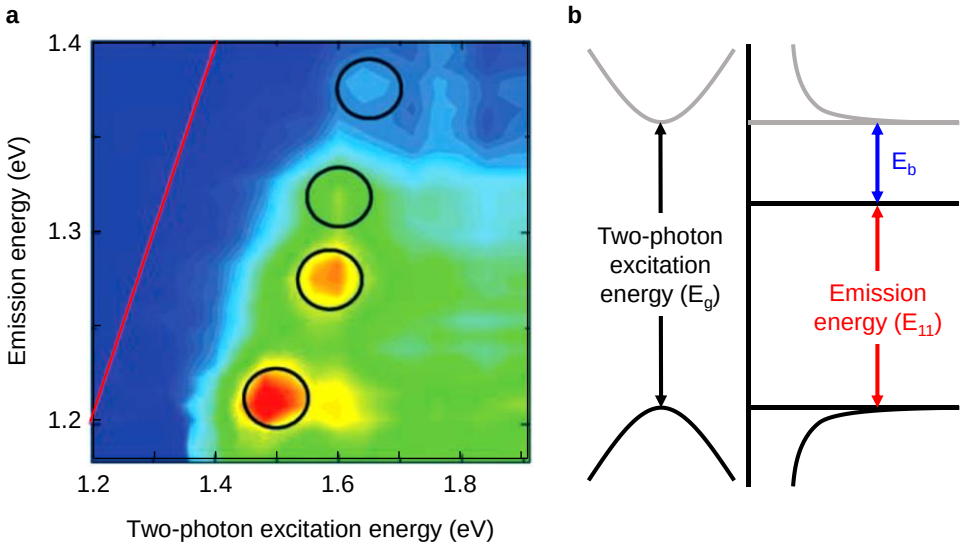

Figure 2-6 Optical resonances in SWCNTs arising from excitons. **a,** 2D contour plot of the two-photon excitation spectrum of SWCNTs. The PL intensity is shown in a false-color representation as a function of the two-photon excitation energy and the one-photon PL emission energy. The two-photon excitation peaks are in general 200–300 meV blue-shifted from the energy of the corresponding emission feature. The red line is to guide where the excitation and emission energies are identical. The circles indicate (7,5), (6,5), (8,3), and (9,1) SWCNTs from bottom to top. The figure is adapted from ref 9. **b,** Schematic of the first sub-band of a semiconducting SWCNT (left) and the corresponding density of states (right). The lowest exciton energy level is shown by the solid horizontal line. The exciton energy (E_{11}) is smaller than the bandgap energy (E_g) due to the exciton binding energy (E_b).

In the excitonic picture, due to the spin multiplicity[18] and intervalley short-range Coulomb interactions of excitons (the presence of K and K' points),[19] SWCNTs impose selection rules on electronic transitions. Combinations of the spin of an electron and a hole of an exciton generate one singlet and three triplet states by spin multiplicity. Each spin state further divides into four states: KK, K'K', K'K and KK', each indicating the location of an electron in the conduction band and a hole in the valence band (Figure 2-7a). As a result, a total of 16 excitonic states exist, with 12 triplet and 4 singlet states for each 1D sub-band of a SWCNT.

Theoretical studies revealed that among these 16 states, only one singlet state is optically allowed.[20-21] Figure 2-7b displays the exciton dispersion relation of the first and second lowest singlets (K'K' and KK, direct excitons). The energy states split by an exchange energy of $\Delta \approx 6$ meV, and the higher energy exciton carries all of the oscillator strength and therefore is optically allowed (bright), whereas the lower energy exciton is dark. The remaining two singlet excitons are doubly degenerate K-momentum excitons (KK' and K'K, indirect excitons). These states have center-of-mass momenta connecting the K and K' points. Even though their large momenta prevent the excitons from directly coupling to photons (optically forbidden), exciton-phonon coupling[22] enables the observation of the K-momentum dark excitonic sideband in optical spectra.[23-24] The energies of the K-momentum excitons are 30–40 meV higher than the bright exciton states (Figure 2-7c). Triplet states are lower in energy than singlet states because no exchange interactions exist in triplet excitons due to the Pauli exclusion principle.

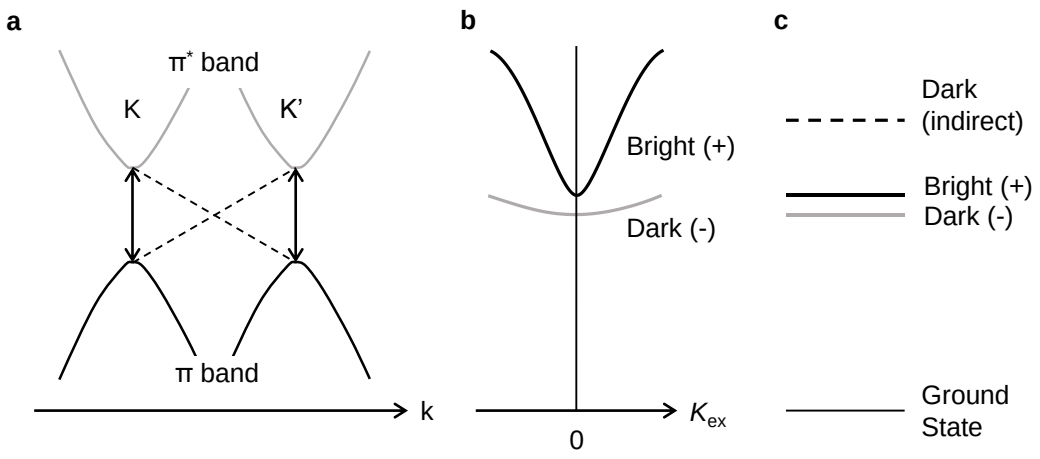

Figure 2-7 Optical selection rules of SWCNTs. **a,** The four possible electron-hole configurations in the K and K' valleys. The solid and dashed arrows indicate the direct and indirect excitons, respectively. **b,** Exciton dispersion relation for the direct (KK and K'K') bright and dark excitons near the center-of-mass wavenumber (K_{ex}) = 0. **c,** Schematic of the exciton energy levels including indirect dark excitons (KK' and K'K, dashed line).

2.1.4 Spectroscopic Characterization of Carbon Nanotubes

Spectroscopic characterization permits sensitive analysis of the 1D properties of SWCNTs. This is attributed to the fact that the unique optical properties of SWCNTs are associated with the 1D confinement of their electronic states, resulting in van Hove singularities in the density of states (Figure 2-5). The singularities in the electronic structure enable optical spectra to display sharp spectral features. However, I would like to note that for the spectroscopic characterization, SWCNTs should be individually isolated because bundled SWCNTs have energy interruption to the electronic states, making the spectrum broad or featureless. Bundled SWCNTs can be individually dispersed by tip sonication,[10] spontaneous exfoliation,[25-26] or surfactant-superacid

exchange[27] methods, and stabilized in an aqueous solution with a surfactant or a polymer.

2.1.4.1 Absorption spectroscopy

The structure-dependent excitonic transitions of SWCNTs can be directly scanned through absorption spectroscopy. The series of optically allowed electronic transitions, E_{ii} (i = 1,2,3,…), carries strong oscillator strength and thus can be observed in an absorption spectrum. For a SWCNT having a relatively small diameter (0.6–1.5 nm), E_{11}, E_{22}, and E_{33} transitions appear in the NIR, visible, and UV regions, respectively (Figure 2-8a). The D-phonon sideband of each E_{ii} transition appears 200–300 meV lower than the primary E_{ii} absorption band and originates from phonon-assisted indirect transitions into dark excitonic states (K-momentum dark excitons in Figure 2-7).

Because each SWCNT has characteristic values of electronic transition energies and molar extinction coefficients, it is possible to identify the composition and fraction of a SWCNT mixture by applying the Beer-Lambert law. Although absorption spectroscopy is useful for identifying the SWCNT chirality, quantitative analysis using absorption spectroscopy is difficult for a mixture of two or more SWCNTs with similar transition energies. In this regard, chirality sorting is important to resolve the well-defined properties of SWCNTs. Gel chromatography[28] or polymer aqueous two-phase separation[29-30] can be adapted to obtain chirality-enriched SWCNT solutions (Figure 2-8b).

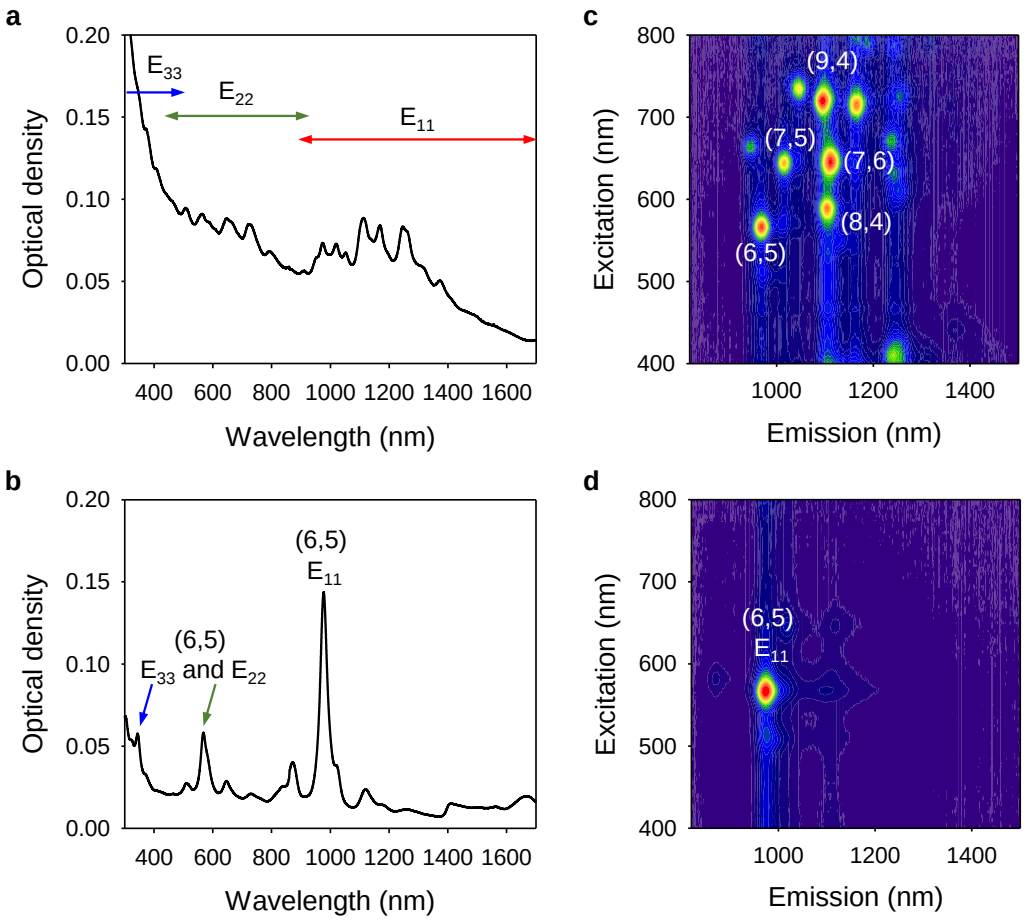

Figure 2-8 Absorption and PL spectra of an unpurified SWCNT mixture (**a,c**) and a gel-purified, (6,5)-enriched SWCNT solution in 1% SDS-D_2O (**b,d**). The ranges of each sub-band transition for semiconducting SWCNTs are marked in **a**. E_{11} (980 nm), E_{22} (568 nm), and E_{33} (350 nm) transitions of (6,5)-SWCNTs are marked in **b**.

2.1.4.2 Photoluminescence spectroscopy

The quantum yield of SWCNTs is influenced by the chirality, length, defect density, and environment, making PL spectroscopy a sensitive tool for studying the excitonic properties of SWCNTs. The excitation-emission PL maps shown in Figure 2-8 provide a basis for identifying SWCNT PL as a function of excitation energy. A vertical slice of the PL map at E_{11} of (*n*,*m*)-SWCNTs is called the PL excitation (PLE) spectrum of the (*n*,*m*)-SWCNT. The PLE profile traces the absorption profile because the nonradiative relaxation from higher sub-bands (E_{22} or higher) to E_{11} is efficient.[17] The PLE spectrum is useful for investigating the electronic coupling between SWCNTs or identifying the origin of the PL emission. Conversely, a horizontal slice of the PL map is the PL emission spectrum at a specific excitation energy. In the PL spectrum of an (*n*,*m*)-SWCNT, the strong PL emission is associated with the radiative recombination of E_{11} excitons (the first sub-band of excitonic transition, E_{11}). At ~140 meV lower in energy than the E_{11} PL, there is a low intensity D-phonon sideband. The D-phonon band results from phonon-assisted excitonic recombination.[22-24] As such, PL spectra provide rich information on the optical properties of SWCNTs.

2.1.4.3 Raman spectroscopy

Raman spectroscopy is also a useful tool for nanotube structural analysis from several characteristic Raman peaks (Figure 2-9). First, the radial breathing mode (RBM) is unique to SWCNTs due to the curvature, and is not observed in other sp^2 carbon materials. It is a totally symmetric vibrational mode related to the vibration of carbon atoms in the directions radial to the nanotube axis. The energy of the RBM peak is inversely proportional to the diameter of the SWCNT and ranges from 50 to 500 cm^{-1} for a diameter range of 5–0.5 nm.[31] Due to its narrow full width at half maximum (FWHM) and diameter dependence, the RBM peak provides complementary information in SWCNT chirality analysis. Second, a Raman band around 1580 cm^{-1} is related to the G band in graphite. This peak represents an in-plane tangential optical phonon involving the stretching of the bond between the two atoms in the graphene unit cell.[32] The curvature effects in SWCNTs split the G band into G+ (1590 cm^{-1}) and G- (1572 cm^{-1}). The G+ and G- bands are related to the circumferential and axial atomic vibrations. Even though the lineshape and Raman shifts of the G- and G+ bands are largely dependent on SWCNT type, *i.e.*, metallic vs. semiconducting, the G band does not provide clear quantitative or qualitative analysis on nanotube electronic structure because the band depends on too many variables.[33] The last key feature of SWCNT Raman spectra is the disorder-induced D band at 1350 cm^{-1}. This is induced by symmetry breaking on the hexagonal sp^2 carbon lattice of SWCNTs. The Raman D-band-to-G-band ratio is used for characterizing the relative density of defects in SWCNTs. SWCNTs with a high density of structural defects have a relatively high Raman D-to-G ratio.[32]

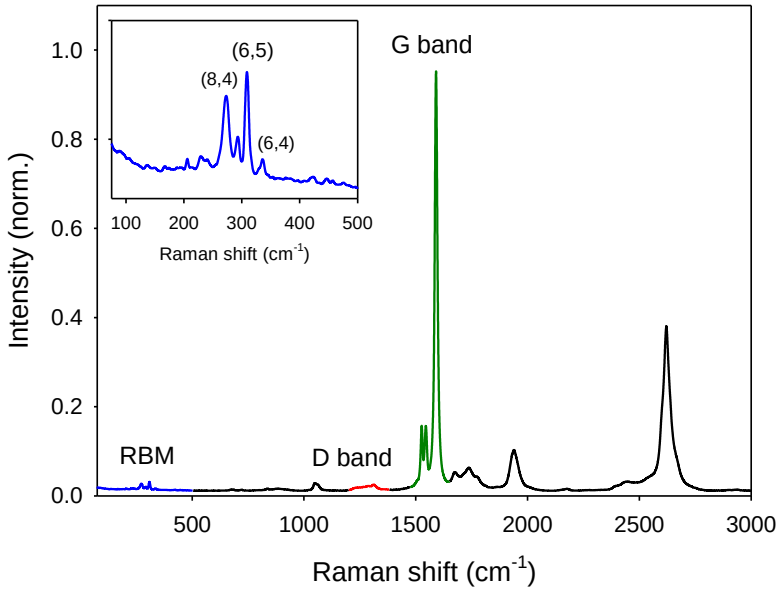

Figure 2-9 Raman spectrum of chirality-enriched (6,5)-SWCNTs at an excitation wavelength of 532 nm. The RBM, D band, and G band are shown in blue, red, and green, respectively. A large peak at 2700 cm^{-1} is an overtone of the D band. The inset shows the enlarged RBM bands at 75–500 cm^{-1}. Because the RBM frequency is inversely proportional to the nanotube diameter, it is possible to identify SWCNT chiralities in the sample.

2.2 Fluorescent Quantum Defects

As discussed in the previous section, dark states exist in the vicinity of the bright state. The low-lying dark states are mainly responsible for the low quantum yields of SWCNTs. The incorporation of fluorescent quantum defects creates new, optically allowed states in SWCNTs. The defect-induced states reside below the lowest dark excitonic state, leading to substantial brightening of SWCNT PL. In this section, I will discuss the definition, characteristics, synthetic protocols, spectroscopic characterization, and applications of fluorescent quantum defects.

2.2.1 Definition of Fluorescent Quantum Defects

Fluorescent quantum defects are chemically created in the sp^2 carbon lattice of semiconducting SWCNTs through covalent attachment of a low density of non-emitting functional groups.[14-15] Experimental results from our lab have shown that a covalently incorporated aryl or alkyl defect can produce a new, defect-induced peak (E_{11}^-). The symmetry breaking of the sp^2 lattice by an sp^3 defect center creates new energy states that are spatially isolated. A deep potential well at a fluorescent quantum defect traps a mobile exciton and makes the exciton fluoresce *via* E_{11}^- (Figure 2-10). As the quantum defects are strongly coupled to the SWCNT host, interesting effects may occur. The available functional groups range from aryl to alkyl, and differ by the synthetic methods.[13-15,34-35] This new class of emitters opens opportunities to probe defects experimentally and to understand the fundamental effects of chemical functionalization in low-dimensional materials.

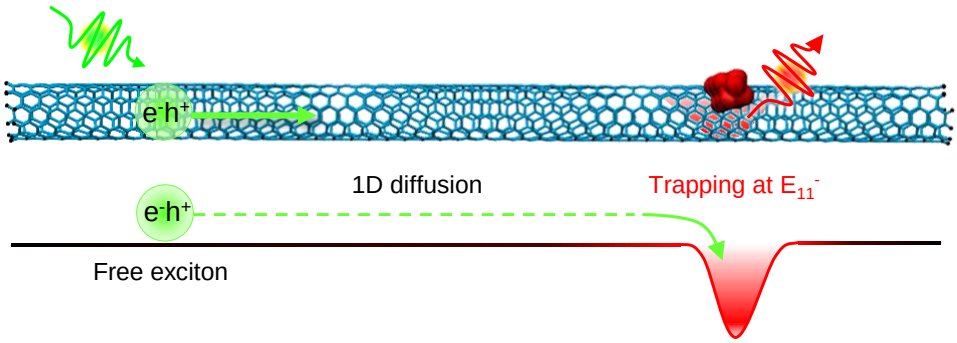

Figure 2-10 Schematic of defect-modulated exciton diffusion and recombination. A free exciton diffuses along the SWCNT, is trapped at a fluorescent quantum defect, and radiatively recombines, emitting an E_{11}^- photon.

2.2.2 Exciton Dynamics in Defect Tailored Carbon Nanotubes

Exciton transport properties in defect-tailored SWCNTs are significantly different from those in unfunctionalized SWCNTs. In reduced dimensions, a single defect becomes important, so much so that its electronic and optical nature can dominate the properties of the SWCNT. In the case of fluorescence, exciton diffusion and trapping dynamics are characteristic parameters that largely determine the role of defects. In this section, I discuss how an exciton behaves in a defect-tailored SWCNT.

2.2.2.1 Diffusion Limited Model

Because an exciton diffuses along the SWCNT axis, the exciton dynamics and PL-related properties can be modeled by the diffusion-limited 1D kinetic model.[36] Hertel *et al.* hypothesized that diffusion-limited contact quenching of excitons determines the PL quantum yield in unfunctionalized SWCNTs. This exciton kinetics is analogous to the generic bimolecular reaction mechanism,

$$A^* + Q \rightarrow A + Q, \qquad \text{Eqn. 2-3}$$

where A^* is a mobile exciton, Q is a stationary quenching site (which includes the SWCNT ends), and A is the quenched exciton state. The change of mobile exciton population can be expressed as

$$\frac{d[A^*]}{dt} = -k_{rad}[A^*] - k_{nr}[A^*][Q], \qquad \text{Eqn. 2-4}$$

in which $[A^*]$ is the density of mobile excitons per unit length, $[Q]$ is the density of quenchers per unit length, and k_{rad} and k_{nr} are the rate constants of radiative and non-radiative decays, respectively. The rate constant of diffusion-limited contact

quenching, k_{nr} is time-dependent and scales with the exciton diffusion coefficient (D) and time (t).

$$k_{nr}(t) = \sqrt{\frac{D}{\pi t}} \qquad \text{Eqn. 2-5}$$

Solving Eqn. 2-4 with Eqn. 2-5 gives the concentration of mobile excitons at time t:

$$[A^*](t) = [A^*]_0 \exp\left[-exp(t/\tau_0)^{1/2}\right] \qquad \text{Eqn. 2-6}$$

in which $[A^*]_0$ is the concentration of mobile excitons at time 0 and τ_0 is a characteristic time scale, $\pi/(4D[Q]^2)$. The integration of Eqn. 2-6 over time gives the number of photons (N_0) emitted from the E_{11} state:

$$N_0 = \frac{L[A^*]_0\pi}{2D[Q]^2\tau_{rad}}. \qquad \text{Eqn. 2-7}$$

The quantum yield of unfunctionalized SWCNT (η_0) is

$$\eta_0 = \frac{N_0}{N_{abs}} = \frac{\pi}{2D[Q]^2\tau_{rad}}, \qquad \text{Eqn. 2-8}$$

in which N_{abs} is the number of E_{11} excitons generated after photoabsorption. Because the number of photons emitted at the E_{11} energy is proportional to the PL intensity of E_{11} (I_{11}) by $N_{11} = aI_{11}$, where a is a constant, we can estimate the relative density of effective quenching sites from the PL intensity of E_{11}.

Incorporation of fluorescent quantum defects adds effective quenching sites for E_{11} excitons in a SWCNT. Thereby, for the defect-tailored SWCNT, we can obtain the following correlation

$$N_{11} \propto \frac{1}{D\tau_{rad}} \frac{1}{\left(n_q + n_{11}^-\right)^2}, \qquad \text{Eqn. 2-9}$$

in which n_q and n_{11}^- are the number of defects on the SWCNT induced by intrinsic quenching sites and fluorescent quantum defects, respectively.

2.2.2.1 Exciton Trapping at a Fluorescent Quantum Defect

The exciton diffusion and trapping model has been applied to study the brightening mechanism and quantum yield of defect trapped excitons[37] and the rate of covalent functionalization.[35]

Considering the diffusion of photogenerated 1D excitons and successive trapping by the local defect state (E_{11}^-), the number of photons emitted from the E_{11}^- state (N_{11}^-) can be expressed as:

$$N_{11}^- = N_{abs}\eta_{11}^- \frac{k_{\mathrm{dif}}}{k_i + k_{\mathrm{dif}}} \frac{n_{11}^-}{n_q + n_{11}^-} \qquad \text{Eqn. 2-10}$$

in which η_{11}^- is the PL quantum yield of a single fluorescent defect site and k_{dif} is the effective decay rate of the E_{11} excitons due to exciton diffusion and successive trapping at the local quenching sites (including intrinsic quenching sites and aryl defects). The factor k_i is the effective decay rate for all possible mechanisms of exciton recombination other than the diffusion-limited mechanism. I note that the contribution of k_i is negligible ($k_i << k_{\mathrm{dif}}$) and therefore $k_{dif}/(k_i + k_{dif}) \sim 1$.[37-38]

The exciton diffusion-trapping model suggests the necessity of controlling the density and spatial tunability of defects in SWCNT. On the one hand, it is important to retain enough conjugated sp^2 crystal structure to produce the number of E_{11} excitons and to maintain the excitonic transport properties in the SWCNT. On the other hand, the higher number of fluorescent defects present, the brighter the defect PL would be. Therefore, either fluorescent quantum defects must be spatially isolated within the exciton diffusion length, or they must be clustered together in a functional band to promote efficient E_{11}^- emission. The experimental observations reflect these correlations. As the degree of functionalization increases (controlled by the initial

reactant ratio[14-15] or the reaction time[34-35]), brighter E_{11}^- PL can be observed. However, if the defect pitch approaches ~5 nm along the SWCNT length ($\ll E_{11}$ exciton diffusion length, 100–500 nm), the excess number of defects irreversibly quenches both E_{11} and E_{11}^- PL.

2.2.3 Chemical Synthesis of Fluorescent Defects

The use of a chemical reaction to implant fluorescent quantum defects provides the opportunity to control the defect density on the nanotube, and also implies that the molecular structure and inductive nature of the defects have been carefully selected. An enormous number of organic synthetic methods can be explored to generate covalent bonds to nanotubes and other carbon nanomaterials.[39] As organic synthesis is used to generate these quantum defects, their molecular nature can be readily controlled, which impacts the localized electronic structure. Here, I will introduce several chemical reactions that produce fluorescent quantum defects in SWCNTs.

2.2.3.1 Billups Birch Reductive Alkylation

The Billups-Birch reduction is one of the first covalent functionalization chemistries to lead to the observation of fluorescent quantum defects.[13] The reaction, involving the solvation of electrons using sodium or lithium in liquid ammonia (–30 ^{o}C), is highly effective at disrupting the van der Waals attractions between nanotubes to generate individually dispersed materials, which is necessary to react scalably with the SWCNT sidewalls. Alkyl halide reactants can then be added to this solution to form radical intermediates upon electron transfer from the reduced SWCNTs, which then

react with the nanotube sidewalls to form covalently attached alkyl groups.[40] A new PL feature appears in the emission spectrum of the functionalized SWCNTs.[13] DFT results reveals that the SWCNT bandgap in the density of states decreases by 70 meV by adding the propagative alkyl groups to a modeled SWCNT.

Deng *et al.* revealed that the Billups Birch alkylation is propagative. The functional bands were clearly resolved in scanning electron microscopy images for highly functionalized SWCNTs over repeated alkylation cycles. DFT calculation suggested that Mulliken charges localize around existing or added defects, driving subsequent functionalization to occur near these sites for a propagating reaction that results in the formation of bands of alkyl functional groups along the nanotube length.[41]

Using this chemistry, one can introduce alkyl defects and achieve 10 meV tunability in the E_{11}^- energy for (6,5)-SWCNTs. The narrow range of tunability is due to the limitations of the chemistry that only worked for a few alkyl defects including perhydrogenated, carboxylic group terminated, and amine terminated hexyl defects (–C_6H_{13}, –$C_6H_{12}COOH$, and –$C_6H_{12}NH_2$).

2.2.3.2 Diazonium chemistry

Diazonium salts, such as 4-chlorobenzenediazonium tetrafluoroborate, have been used as a means to react selectively with metallic SWCNTs[42] to diminish conductivity and improve on/off ratios of SWCNT transistors. The mechanism behind this metallic selectivity is thought to be a result of the relatively rapid non-covalent adsorption of the diazonium molecule to metallic nanotubes due to the higher density of states at the Fermi level compared to their semiconducting counterparts, followed by a slower covalent reaction initiated by electron transfer from the nanotube to the

reactant to form a radical that readily initiates a C–C bond with the graphitic surface. The physisorption of diazonium salts on semiconducting SWCNTs induces stepwise quenching of E_{11} PL because the adsorbed diazonium molecules act as effective quenching sites for excitons.[36,43] However, following the physisorption of diazonium salts to the SWCNT, electron transfer from the SWCNT to the diazonium creates an aryl radical that can initiate covalent functionalization of aryl groups to the SWCNT.[44] Even though diazonium chemistry has been extensively studied for SWCNT functionalization, the synthesis of fluorescent quantum defects *via* the diazonium reaction has only been recently discovered. Piao *et al.* explored the regime of low defect density (0.33 mol% diazonium reagent relative to carbon), where the average defect spacing is comparable or slightly shorter than the exciton diffusion length surface (approximately < 1 defect/20 nm length) Reacting SWCNTs dispersed in 1% wt/v sodium dodecyl sulfate in D_2O or water with aryl diazonium salts at room temperature leads to the evolution of defect-induced PL (E_{11}^-), redshifted by up to 254 meV from the native nanotube fluorescence.[14]

Diazonium chemistry is the most widely used method for creating fluorescent quantum defects because of its simplicity and its potential for wide tunability with a variety of functional groups. Varying the terminating groups of aryl defects from electron-donating (–4-N(C_2H_5)$_2$) to electron-withdrawing groups (–3,5-(NO_2)$_2$) can shift the E_{11}^- PL emission from 1120 nm to 1158 nm (36 meV tunability) for (6,5)-SWCNTs. Furthermore, the overall quantum yield of (6,5)-SWCNTs is in fact enhanced from ~1% to 16% due to the addition of the E_{11}^- emission through aryl defects.[14]

2.2.3.3 Diazoether chemistry

Diazoether chemistry uses the diazoether molecule (3-*O*-4-nitrobenzenediazoascorbic acid; NO_2Ar-DZE) for covalent functionalization with 4-nitroaryl defects on SWCNTs in 1% wt/v SDS-D_2O.[34] DZE molecules comprise ascorbic and aryl groups that are coupled by an azo bond and can exist as *E* or *Z* isomers. The two stereoisomers have different stability due to the difference in structure and bond length. In contrast to the reactive *Z* isomer, the *E* isomer is inert to SWCNTs at room temperature. Without exposure to light, (6,5)-SWCNTs remain intact, evidenced by no E_{11}^- PL evolution. However, under light excitation at a narrow pH window (centered around 3.8), the *E* isomer can react with SWCNTs and create a covalently bonded aryl defect on the SWCNT sidewall. Interestingly, the reactivity of the *E* isomer is switchable either by illumination or by pH change (Figure 2-11). The selectivity comes from a high barrier to isomerize the inert *E* form into the reactive *Z* form. This degree of reaction control using light suggests the potential for lithographic patterning of fluorescent quantum defects.[35] DZE chemistry also offers a level of chirality selectivity that cannot be achieved by diazonium chemistry.

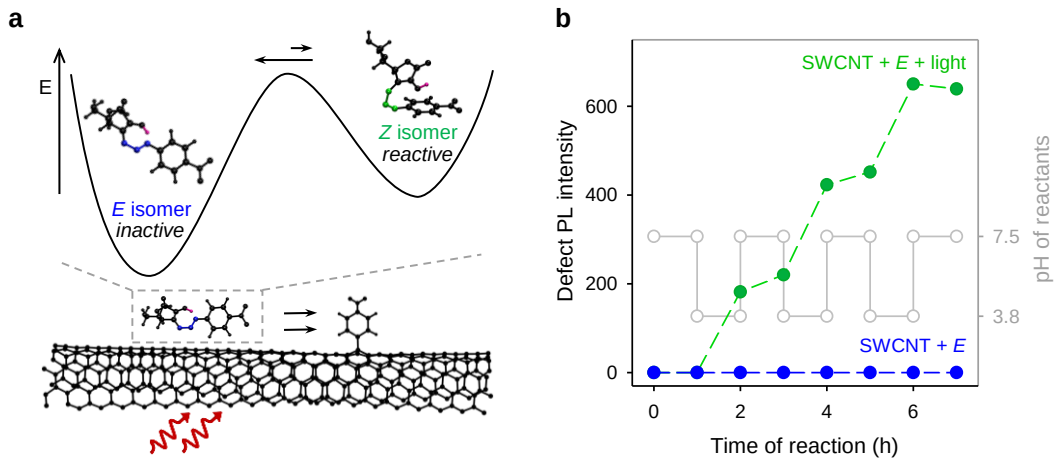

Figure 2-11 Switching of NO_2Ar-DZE reactivity toward a SWCNT. **a,** A schematic showing the localized isomerization of the inert *E*-isomer to the reactive *Z*-isomer by tuning of the barrier to isomerization with pH and resonant optical excitation of the SWCNT. **b,** Reversible activation of reactivity of *E*-diazoether *via* illumination and pH to covalently attach aryl defects to SWCNTs. Step-wise reactivity of the *E*-isomer with (6,5)-SWCNTs was realized through 565 nm excitation (green) and pH switching (gray) compared to the dark control.

2.2.3.4 X-bond chemistry

Kwon *et al.* demonstrated the extent of molecular tunability possible for fluorescent quantum defects with the development of relatively simple alkyl halide chemistry.[15] This reaction, involving SDS-dispersed SWCNTs in aqueous solution, an alkyl iodide reactant, acetonitrile, and the mild reducing agent sodium dithionite, has demonstrated the ability for covalent attachment of over 30 functional groups to SWCNTs at room temperature (remaining stable in aqueous solution for several months), including both mono- and divalent moieties, enabling the defect-induced E_{11}^- peak of (6,5)-SWCNT to be redshifted by as much as 190 meV from the native E_{11} emission and increasing the quantum yield compared to the parent nanotube by an order of magnitude (Figure 2-12). The molecular tunability of this reaction is made possible

by the chemistry's flexible use of almost any iodide-containing (and a few bromide-/chloride-containing) hydrocarbon-based compounds. DFT calculations also suggest that, like the Billups-Birch reaction, functionalization is favored near existing defects (specifically the para-position). Charges tend to accumulate in these regions according to Mulliken analysis, suggesting the likelihood of propagative functionalization for banding or clustered defect structures.

Furthermore, Wu *et al.* have found that photoinduced functionalization of aryl halides can be achieved by exciting the host SWCNTs resonantly.[35] The reaction is temperature independent, but is strongly dependent on photon energy. (6,5)-SWCNTs were excited with various wavelengths of light in the presence of 4-iodoaniline, which absorbs in the UV region. When the solutions were excited at the third and second sub-band transitions of (6,5)-SWCNTs (E_{33} and E_{22}), the rapid evolution of E_{11}^- PL was observed. Meanwhile, the lack of functionalization under E_{11} excitation was posited to be a result of insufficient photon energy to overcome the reaction barrier. These experiments suggest a reaction mechanism in which the excitation of an electron from the SWCNT's ground state to the conduction band of the E_{22} van Hove state results in subsequent electron transfer to the lowest unoccupied molecular orbital of the physisorbed aryl halide. As the reduced 4-iodoaniline readily dissociates into an aniline radical and iodine anion, the radical can then covalently bond with the nanotube. Similar to diazoether chemistry, a photo-switching experiment demonstrated the sensitivity of the reaction to light.

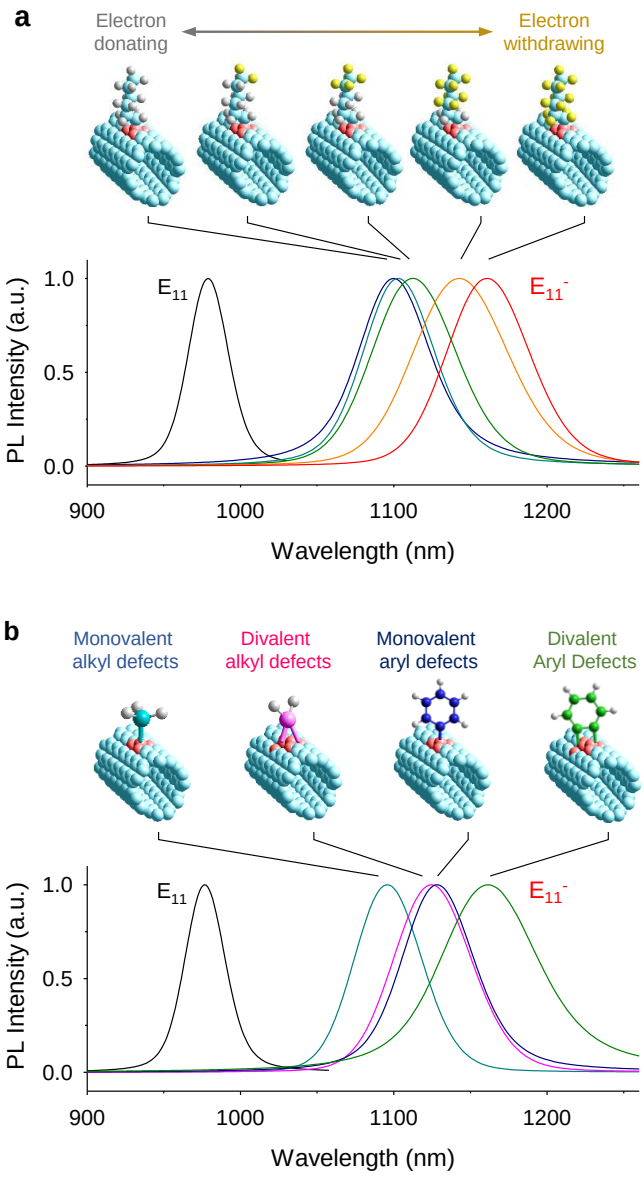

Figure 2-12 Tunable near-infrared PL from defect-tailored (6,5)-SWCNTs. **a,** PL spectra of (6,5)-SWCNTs functionalized with six-carbon alkyl chains with increasing numbers of fluorine substituents. **b,** Comparison of monovalent and divalent fluorescent quantum defects. The SWCNT solutions were excited at 565 nm. The E_{11} PL appears at 980 nm, whereas the E_{11}^- PL is systematically tunable by changing the functional group. The spectra were fitted with Voigt functions. The figures are adapted from ref 15.

2.2.4 Spectroscopic Characterization of Fluorescent Defects

Covalent functionalization of fluorescent quantum defects on SWCNTs changes the hybridization of a defect center from sp^2 to sp^3. Various spectroscopic and imaging techniques can distinguish these types of carbon on the ensemble level, and can be used to detect the presence of quantum defects in SWCNTs.

As discussed above, Raman spectroscopy is one of the most commonly used tools for characterizing the density of defects in SWCNTs (Figure 2-13). Similarly, X-ray photoelectron spectroscopy can be used to determine the presence of defects through the sp^3 peak of C as a function of the applied chemistry. The disruption of the sp^2 crystal with sp^3 defects will also decrease the electrical conductivity of the nanotube. Using substrate-enhanced scanning electron microscopy, the location of clustered defects on SWCNTs can be resolved, as evidenced by the alternating regions of the nanotube that are insulating due to the prevalence of sp^3 carbon thus creating a localized charging effect that appears brighter in contrast with the more conductive regions of the carbon structure.[41]

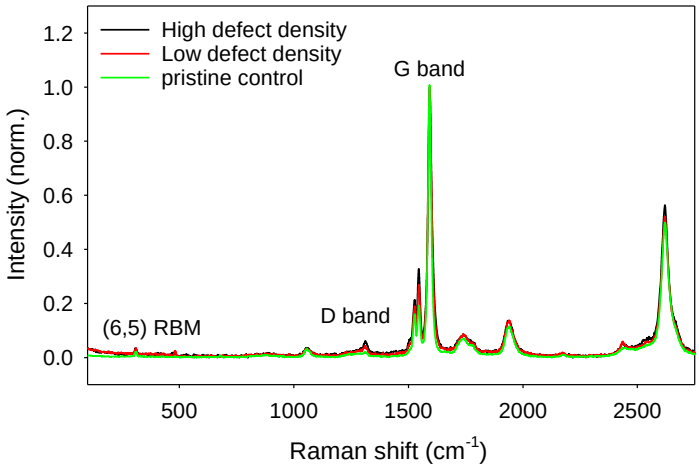

Figure 2-13 Raman spectra of unfunctionalized (green) and 4-aminoaryl defect tailored (6,5)-SWCNTs (red and black). The intensity is normalized to the G band. The excitation wavelength was 532 nm. The integrated intensity ratio of the D band to G band increased from 0.016 to 0.040 by the aryl defects. The figure is adapted from ref 35.

However, the most salient optical feature of fluorescent quantum defects – the generation of a new optical transition redshifted from the native E_{11} emission – is the most direct way of monitoring the presence of these chemical changes. Increasing covalent functionalization is known to disturb the intrinsic electronic structure of SWCNTs and decrease the effective absorption cross section of SWCNTs due to the disruption of the sp^2 symmetry. As such, the reaction progress and the degree of functionalization can be monitored through the decrease of E_{11} and E_{22} absorption bands. At low degrees of functionalization, at which a sufficient fraction of the graphitic crystal remains intact, both the optical absorptions and PL emissions originating from the van Hove transitions in individual SWCNTs can be retained.[14] At a higher density of defects, for which the van Hove transitions almost disappear, the defect-induced states can be observed in the absorption spectrum. The energy of the

new absorption band is consistent with the emission energy of E_{11}^- PL, suggesting that sp^3 defects create new electronic states in the SWCNT (Figure 2-14). PL spectroscopy is the most sensitive method to monitor the fluorescent quantum defects. The covalent functionalization of SWCNTs evolves a new PL peak at 100–300 meV redshifted from E_{11} PL, whereas E_{11} PL continues to decrease.

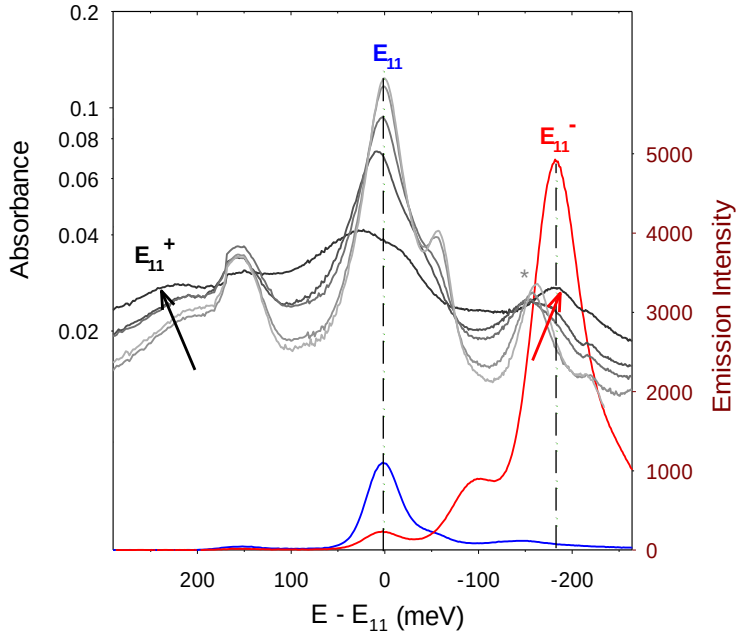

Figure 2-14 Emergence of a defect-induced, low-lying state in the absorption and PL spectra by the covalent functionalization of (6,5)-SWCNTs with 4-nitroaryl defects. As the degree of functionalization increases (light gray to dark gray), the E_{11} absorption band continues to decrease and new absorption bands (E_{11}^+ and E_{11}^-) evolve. The PL spectra of the unfunctionalized (blue) and functionalized SWCNTs (red) unambiguously show that the evolution of redshifted absorption band (E_{11}^-) is associated with the defect-induced state. The excitation wavelength was 565 nm. The figure is adapted from the work by Piao *et al.*[14]

2.2.5 Applications

Enabled by the flexibility of functional groups and tunability of emission energy, fluorescent quantum defects hold a strong potential to be widely used as a quantum light source and in sensing and imaging applications. Here I introduce a few important applications.

2.2.5.1 Sensing

The intensity and emission wavelength of SWCNT PL are sensitive to environmental factors. Even though the optical properties have made SWCNTs obvious choices for sensing applications, unfunctionalized SWCNTs generally have poor selectivity and limited variation on the chemical response. These limitations may be addressed with fluorescent quantum defects that can be chemically tailored to create bioimaging probes and chemical sensors with high sensitivity and selectivity. As defect PL is extremely sensitive to the local environment, as demonstrated by the shifting emission wavelength as a function of the electron-withdrawing nature of the functional group.[14-15] This sensitivity can be capitalized on for sensing small molecules or even ions by taking advantage of changes to the defect's inductive effect upon molecular specific binding.

Kwon *et al*. demonstrated the sensing potential of fluorescent quantum defects.[45] SWCNTs with *N*,*N*-diethyl-4-aminoaryl defects were tested for optical pH and temperature sensing (Figure 2-15a). The covalent addition of *N*,*N*-diethyl-4-aminoaryl defects to the nanotube surface induced the E_{11}^- emission at 1120 nm at a pH of 7.40. Lower pH solutions resulted in protonation of the amino group and a significant redshift of the E_{11}^- wavelength, whereas the wavelength of E_{11} remained

constant. In this manner, the position of E_{11}^- shifts as the pH is changed from 4.5 to 8.5, which covers the physiological pH range (5.5–8.0), across which PL shifts can be resolved down to changes as small as 0.2 pH units.

Furthermore, aminoaryl-functionalized SWCNTs can be used to monitor the temperature of the solution from PL intensity changes. At higher solution temperature, the increased thermal energy enables defect-trapped excitons to escape the potential well, diminishing the integrated intensity ratio I_{11}^-/I_{11}. The detailed description of the temperature dependence will be addressed in Chapter 4. These results demonstrate how the defect PL can be utilized to develop a nano-thermometer and pH-meter, which should have direct application for high-resolution sensing in complex, or *in vivo*.

2.2.5.2 Bioimaging

Compared to visible light, NIR light (750–1400 nm) exhibits low scattering and deep penetration depth in biological tissue.[12] SWCNTs have always been considered promising candidates for bioimaging because of their remarkably narrow emission lines (FWHM ~23 meV at room temperature), but most importantly due to their ability to fluoresce in a range of the NIR (800–1600 nm) that effectively covers the NIR tissue transparency window. Additionally, unlike molecular fluorophores,[46] SWCNTs are exceptionally photostable; they do not blink or photobleach under prolonged excitation.[47]

SWCNTs with fluorescent quantum defects have brighter PL emission than unfunctionalized SWCNTs, and can exhibit new defect-induced emission in the NIR-II region (1000–1500 nm),[12] where light can penetrate biological tissue extremely well with minimal scattering and lower background fluorescence. The presence of defect-

induced state may enable total NIR excitation and emission, which enables nondestructive and high-resolution bioimaging (Figure 2-15b).

2.2.5.3 Single photon source

Physical systems with 0D quantum confinement of carriers, such as nitrogen vacancy centers in diamond, exhibit photon antibunching. The optical anharmonicity in such quasi 0D systems arises from phase-space filling—a consequence of the Pauli exclusion principle that prevents carriers from occupying identical quantum states. The applications of single photon emission are numerous, including quantum information processing, cryptography, and telecommunications.

Högele *et al.* found that a local trap of unfunctionalized SWCNT can emit photons one by one at cryogenic temperatures.[11] However, at a higher temperature, the trapped exciton can readily escape from a shallow trap by thermal energy. These limitations make SWCNTs less efficient systems in single-photon emission.

Fluorescent quantum defects create deep potential wells (several hundred meV $\gg$ kT) that strongly localize excitons. The potential well is deep enough to suppress the thermal detrapping of a defect-trapped exciton and make the exciton radiatively decay from E_{11}^- state. As a demonstration of this concept, He *et al.* have reported photon antibunching at room temperature from aryl defect tailored SWCNTs (Figure 2-15c).[48-49] The combination of the diverse functional groups and the structure-dependent optical tunability of SWCNTs enabled to generate room-temperature single-photon emission spanning the broad telecom band (up to 1550 nm).[48]

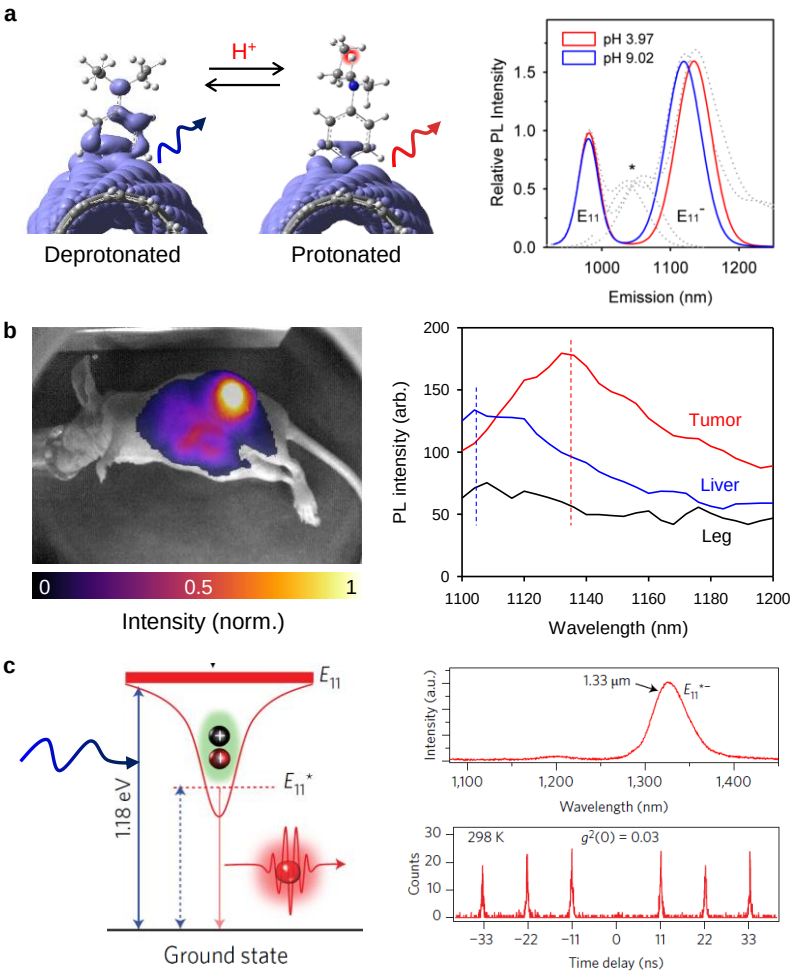

Figure 2-15 Applications of fluorescent quantum defects. **a,** Optical pH sensing in complex solutions. The left schematic shows protonation and deprotonation at a 4-*N*,*N*-diethylaminoaryl defect at (6,5)-SWCNT. The right plot shows the defect PL shifts observed by changing pH of (6,5)-SWCNT-$C_6H_4N(C_2H_5)_2$ solution, reported by Kwon *et al.*[45] **b,** *In vivo* imaging of polymer-suspended (6,5)-SWCNT-$C_6H_4N(C_2H_5)_2$. The left figure displays the intensity distribution of SWCNT PL in a mouse 3 hr after the SWCNT injection. The right plot shows the defect PL spectra of the functionalized (6,5)-SWCNTs. pH difference between tumor and liver can be probed by the wavelength of defect PL (unpublished results from our group) **c,** Single photon source. The left figure is a schematic of a fluorescent aryl defect as a single photon source. The right graphs show the PL spectrum and second-order time correlation of defect PL in (7,5)-SWCNT-$C_6H_4OCH_3$. These figures are adapted from ref 48.

2.3 Challenges to be addressed in this dissertation

In my Ph.D., I explore how optically forbidden dark excitons can be brightened to improve the quantum yield of SWCNT PL. For instance, how does an exciton behave at a defect site? How can the defect trapped exciton be controlled? What is the limit of PL brightening through fluorescent quantum defects?

There are two big challenges in answering these questions. First, the complexity of the system makes it difficult to synthesize fluorescent quantum defects with the desired photophysical response. To be specific, the chemical nature of defects, the density of defects, and the structure of SWCNTs strongly influence the energy of defect PL, electronic coupling with the SWCNT host, the interaction between excitons and electrons, and the trapping of excitons at fluorescent quantum defects. To resolve each factor and clarify the system, I studied the dependence of SWCNT structure on the defect PL and the binding energy of defect-trapped excitons (Chapter 3). The density of defects and the chemical nature of defects are systematically varied to control the exciton trapping depth at a defect site (Chapter 4). Also, I studied the brightening of trions by colocalization of an electron and an exciton at a defect site (Chapter 4).

Another challenge is the lack of adequate analytical tools to probe the fluorescent quantum defects in a molecular-level precision. Although single tube PL spectroscopy is a sensitive tool to optically explore the functionalized SWCNTs, its precision is diffraction-limited. Because the defect PL typically occurs in the NIR, the spatial resolution of the defect PL is low (several hundred nm). Although superlocalzation techniques can be used to define the number of defects and their location below the diffraction limit, the spatial information does not provide the

complete picture of the emissive defect state. Correlating the spectral information into spatial information for a single functionalized SWCNT would be adequate to study the emissive defect state, but the scarcity of the ultra-sensitive NIR camera makes obtaining the PL spectrum of a single defect difficult. My colleagues and I address this challenge by building up a novel super-resolved hyperspectral PL imager, enabling us to probe a spatially and spectrally resolved fluorescent quantum defects in SWCNT at the single defect level (Chapter 6).

3 Mapping Structure-Property Relationships of Fluorescent Quantum Defects

Adapted from a manuscript by Kim, M.; Wu, X.; Ao, G.; He, X.; Kwon, H.; Zheng, M.; Doorn, S.K.; Wang, Y.

Y.W. and M.K. conceived and designed the experiments. M.K., H.K., and Wu, X. performed experiments. Ao, G., He, X. performed carbon nanotube sorting. M.K. and Y.W. wrote the manuscript with inputs from all co-authors.

3.1 Introduction

Fluorescent quantum defects are an emerging class of synthetic defect emitters that can be chemically incorporated into the sidewall of a single-walled carbon nanotube (SWCNT) through covalently bonding functional groups to the semiconductor host.[14-15,35] An introduced chemical defect locally modulates the electronic structure of the SWCNT host to enable trapping of excitons, which can exhibit strong single photon emission. The defect-induced emission (E_{11}^-), which is in the near IR, can be significantly brighter than the native photoluminescence (E_{11}) of the nanotube, suggesting vast potential for applications in imaging,[50] sensing,[45] and creating single-photon sources in the telecom bands.[48-49]

The electronic and optical properties of fluorescent quantum defects vary substantially with the structure of the SWCNT host, each of which is assigned a specific (*n*,*m*) chirality that describes its construction as a rolled-up graphene sheet. There are an increasingly larger numbers of functional groups that are being identified capable of creating fluorescent quantum defects, suggesting virtually unlimited opportunities in broadly applying organic chemistry in this emergent field.[13-15,35,51-54] The

unfunctionalized SWCNT hosts are quasi-1D nanostructure with electronic structure and optical properties of highly predictable.[55] Particularly, the excitonic transition energies of semiconducting SWCNTs show strong dependence on both diameter and chiral angle, as summarized in correlation plots known as the Kataura plots.[21,56] In contrast, systematic analysis of the structure-dependence of fluorescent quantum defects has yet to be performed. It is important to understand how the defect state is related to the nanotube family pattern and chirality, and how the 1D SWCNT couples to the 0D quantum state of the organic colour centres, in order to provide a predicative understanding that will enable the design and synthesis of this family of quantum emitters for bioimaging, biosensing, quantum computing, and nanophotonics, as well as probing the rapidly unraveled fundamentally new phenomena of defect chemistry and physics. Even simply knowing the energies of these defect states for specific (*n*,*m*) structures and fluorescent quantum defects would be important not only for fundamental photophysics of defect-trapped excitons, but also for applications in infrared imaging, chemical sensing, and tailored design and synthesis of quantum materials.

Herein, we stablish structure-property relationships for fluorescent quantum defects through controlled synthesis and comparative spectral studies of 30 chemically distinct fluorescent quantum defects and 14 purified nanotube hosts. We observed distinct defect-induced photoluminescence (PL) features for 14 semiconducting SWCNT species (ranging from 0.62 to 0.94 nm in diameter and from 0 to 27.5° in chiral angle) using 30 different functional groups. Based on the spectrofluorometric measurements of perfluorohexyl-defect-tailored (*n*,*m*)-SWCNTs, we analyzed the E_{11}^-

as empirically fitted functions of nanotube diameter. Our results show that the measured E_{11}^- PL energy is tunable by 400 meV in the near-infrared *via* SWCNT diameter. However, the emission energy of defect-trapped excitons is nearly free from chiral angle and family patterns, suggesting that an exciton at a fluorescent quantum defect to some degree behaves independently from the nanotube host but this quantum defect -host coupling is chemically tunable depending on the chemical nature of the defect in terms of the group's electron withdrawing ability and bonding configuration. These findings provide a comprehensive picture of the structure-property relationships of fluorescent quantum defects that is required to guide controlled and tailored synthesis of this new family of quantum emitters.

3.2 Experimental Section

3.2.1 High Purity SWCNT Sorting.

SWCNT powders (CoMoCAT SWCNTs from Southwest Nanotechnologies and HiPco SWCNTs from Rice University) were dispersed in an aqueous solution of surfactant or DNA by tip-sonication at 8 W for 1 h. Supernatants were collected after 1.5 h centrifugation at 17,000 g for SWCNT purification. (6,4)+(7,3) and (5,4)-SWCNTs were purified using polymer aqueous two-phase separation (ATP), as previously reported by Hartmann *et al.*[57] After ATP, the purified SWCNT solutions were pressure-filtrated (Amicon, no. 5123, using 100 kDa ultracel regenerated cellulose filter membranes) using 1 wt/v% sodium deoxycholate (DOC) to dilute the polymer concentration by a factor of 10^3 and concentrate the solution volume. (11,1),

(10,3), (11,0), (7,5), (6,5), (9,1), and (6,4)-SWCNTs were sorted by DNA mediated ATP methods.[29] The DNA sequences used for the DNA-ATP separation are listed in Table 3-1. In this work, we sorted 14 types of semiconducting SWCNT species into samples highly enriched in single chiralities in total (Figure 3-3).

After ATP, purified SWCNTs were precipitated from the polymer solution using sodium thiocyanate (Sigma Aldrich, 98%), and the wrapping molecules for aqueous suspension of SWCNTs were substituted from DNA to 1 wt/v% DOC. Alternatively, HiPco SWCNTs (Rice University, batch #194.3) were sorted using Sephacryl S-200 high-resolution chromatography resin (GE Healthcare), as described previously by Liu *et al.*[28] to produce (7,6)+(8,4), (8,3)+(8,4), (8,3)+(7,3), and (6,5)-SWCNT enriched samples. For subsequent functionalization, the purified SWCNTs were stabilized as individual nanotubes in D_2O (Cambridge Isotope Laboratories, Inc., 99.8%) by 1 wt/v% sodium dodecyl sulfate (SDS, Sigma Aldrich, ≥ 99%). To prevent inner filter effects in spectroscopic characterization, the SWCNT concentration was kept low, with an optical density of 0.03–0.12 at E_{11}.

Table 3-1 DNA recognition sequences for the ATP-sorted SWCNTs

SWCNT chirality	DNA sequence
(11,1)	$T_4C_4T_4$
(10,3)	C_5TC_6
(6,4)	$A_3T_6A_3$
(11,0)	GC_{11}, C_{12}, TC_6T, $AC_{10}A$, AC_{11}
(9,1)	$(GTC)_2GT$, $(TG)_2T_4(GT)_2$
(6,5)	$TTA(TAT)_2ATT$
(7,5)	$(ATT)_4$, $TGG(GTG)_2GGT$

3.2.2 Covalent Functionalization of Fluorescent Quantum Defects

Diazonium chemistry was the primary method used for covalent attachment of aryl functional groups to the SWCNTs.[14,48,53] A series of diazobenzene tetrafluoroborate salts was synthesized from aniline derivatives, as reported previously.[14] A small amount of diazonium salt was added to the chirality-enriched SWCNTs with a SWCNT-carbon-to-diazonium-salt molar ratio of 100–3000. To accelerate the reaction for low reactivity SWCNT species, such as (11,0), white light illumination was required.[48,53] On the other hand, for some aryl defects that cannot be incorporated using diazonium reactions, such as divalent aryl or aminoaryl defects (e.g., $>C_6H_3NH_2$), light activated arylation was used.[35] For the reaction, a small aliquot of aryl halide (a molar ratio of 50) in acetonitrile (Acros organics, HPLC grade, 99.9%) and 7.6 mM of sodium bicarbonate (EMD chemicals, HPLC grade) was added to 1 mL of (6,5)-SWCNT (optical density at E_{11} ~0.1). Then the SWCNT solution was exposed to excitation light resonant to the SWCNT chirality to activate the arylation. The PL spectrum was *in situ* monitored. Once the defect PL intensity was sufficient to identify the peak position, the excitation-emission PL map was collected.

We followed the experimental protocols reported in ref 15 to create alkyl defects. Briefly, a small aliquot of alkyl iodide (or bromide) dissolved in acetonitrile was added to the chirality-enriched SWCNTs with a SWCNT carbon to alkyl halide molar ratio of 10–300. The solution pH was adjusted to 8 by adding 7.6 mM sodium bicarbonate. Then, 3.6 mM of $Na_2S_2O_4$ (Sigma Aldrich, 85%) was added to the mixture. After 2 h of reaction, the SWCNT solution was characterized by excitation-emission PL mapping. To increase the density of the defects or drive reactions for low

reactivity SWCNTs, the concentration of the reactants can be increased proportionally to the concentration of the nanotubes.

3.2.3 Spectroscopic Characterization.

The SWCNT PL was characterized with a NanoLog spectrofluorometer (Horiba Jobin Yvon) using a liquid-N_2 cooled InGaAs array. The SWCNTs were excited with monochromator-selected light (10 nm slit width) from a 450 W Xenon arc lamp. The excitation power was lower than 10 mW with an integration time of 1–10 s. The spectral resolution was 10 nm for the emission detection channel. UV-vis-NIR absorption spectra were obtained with a spectrophotometer equipped with a broadband InGaAs detector (Lambda 1050, PerkinElmer). The path length of absorption measurements was 10 mm.

3.2.4 Temperature-Dependent Photoluminescence Spectroscopy

3,5-dinitroaryl-functionalized (6,5)- and (8,4)-SWCNTs in 1% SDS-D_2O with the intensity ratio I_{11}^-/I_{11} of ~2.8 at 25 °C were used. The SWCNT solutions were heated from 25° to 60 °C using a circulating water bath, and the PL spectra were obtained in increments of 5–10 °C. The SWCNT PL was characterized with a NanoLog spectrometer. The temperature dependent PL spectra were obtained at E_{22} excitation of (6,5)- and (8,4)-SWCNTs (565 nm and 590 nm, respectively). The solution temperature was measured with a surface temperature sensor (LabQuest 2, Vernier). The PL peaks of E_{11} and E_{11}^- were fitted with Voigt line shapes using Peakfit v4.12 (SeaSolve). The integrated peak areas were plotted as a function of temperature (Figure 3-1).

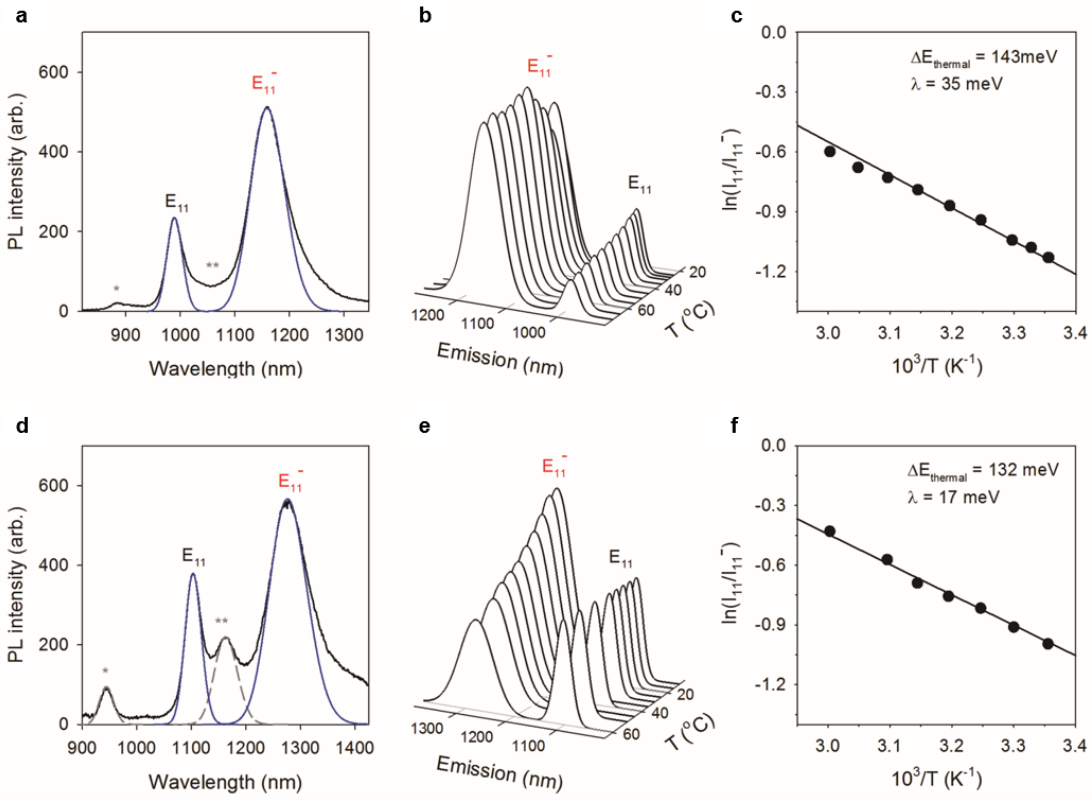

Figure 3-1 Temperature dependence of 3,5-dinitroaryl defect functionalized **a-c,** (6,5)- and **d-f,** (8,4)-SWCNTs. **a,d,** PL spectra of the functionalized (6,5)- and (8,4)-SWCNTs at E_{22} excitation. Asterisks (* and **) denotes the E_{11} and E_{11}^- PL of (6,4)- and (8,3)-SWCNTs. **b,e,** Temperature-dependent PL evolution. **c,f,** PL intensity ratio I_{11}/I_{11}^- as a function of inverse temperature for 3,5-dinitroaryl functionalized The slope of each linear fit corresponds to the thermal detrapping barrier at the fluorescent defect ($\Delta E_{thermal}$). The reorganization energy is derived by subtracting $\Delta E_{thermal}$ from the optical gap ($E_{11} - E_{11}^-$) as is discussed more in the next chapter.

3.3 Results and Discussions

3.3.1 Incorporation of Fluorescent Quantum Defects in SWCNTs

We covalently attached functional groups into a series of (n,m)-SWCNTs to study the correlation of the photon energy emitted from the resulting fluorescent quantum defects with the structure of the SWCNT host (Figure 3-2). The chirality sorted SWCNTs were stabilized in 1 wt/v% SDS-D_2O for subsequent functionalization (see Experimental Section for detailed protocols). The semiconducting SWCNT structures studied in this work ranged from 0.62 to 0.94 nm in diameter and from 0 to 27.5° in chiral angle (Table 3-2). We used diazonium[14] or alkyl[15]/aryl halide[35] chemistry for covalent attachment of 30 different functional groups to the selected SWCNT chiralities. The attached functional groups vary in electron withdrawing capability and bonding configurations, enabling us to modify the energy level of the defect state systematically relative to the native electronic structure of the nanotube. The functionalized SWCNTs were characterized by UV-vis-NIR absorption and PL spectroscopy. The E_{11} and E_{11}^- wavelengths were determined by fitting the PL spectrum resulting from E_{22} excitation using Voigt profiles.

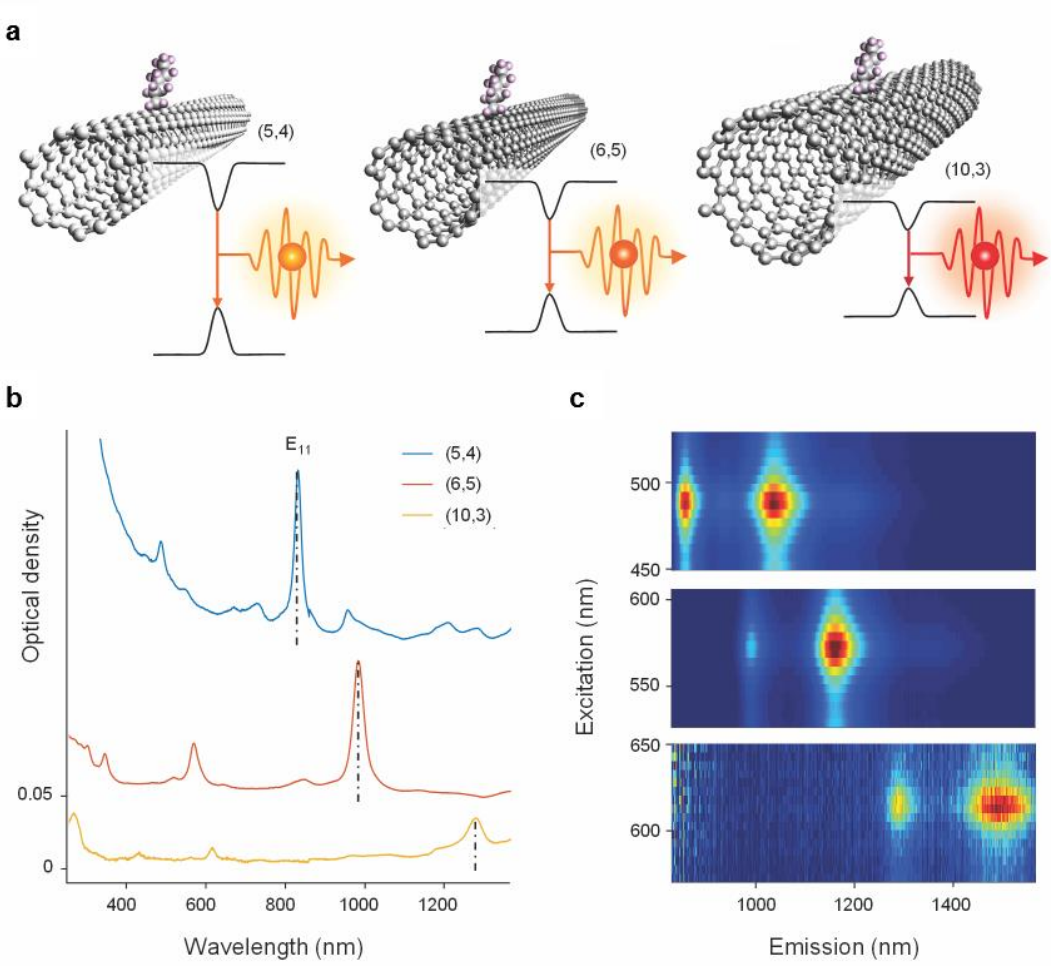

Figure 3-2 Fluorescent quantum defects in semiconducting SWCNT hosts. **a,** Schematic representation of fluorescent quantum defects incorporated as perfluorohexyl defects into a series of (*n*,*m*)-SWCNTs. An individual quantum defect creates a host-structure-dependent potential well where a mobile exciton can be trapped and fluoresce brightly. **b,** UV-vis-NIR absorption spectra of purified (5,4), (6,5), and (10,3) SWCNT solutions dispersed in 1 wt/v% SDS in D_2O. **c,** Excitation-emission PL maps of perfluorohexyl functionalized (5,4), (6,5), and (10,3) SWCNTs, from top to bottom.

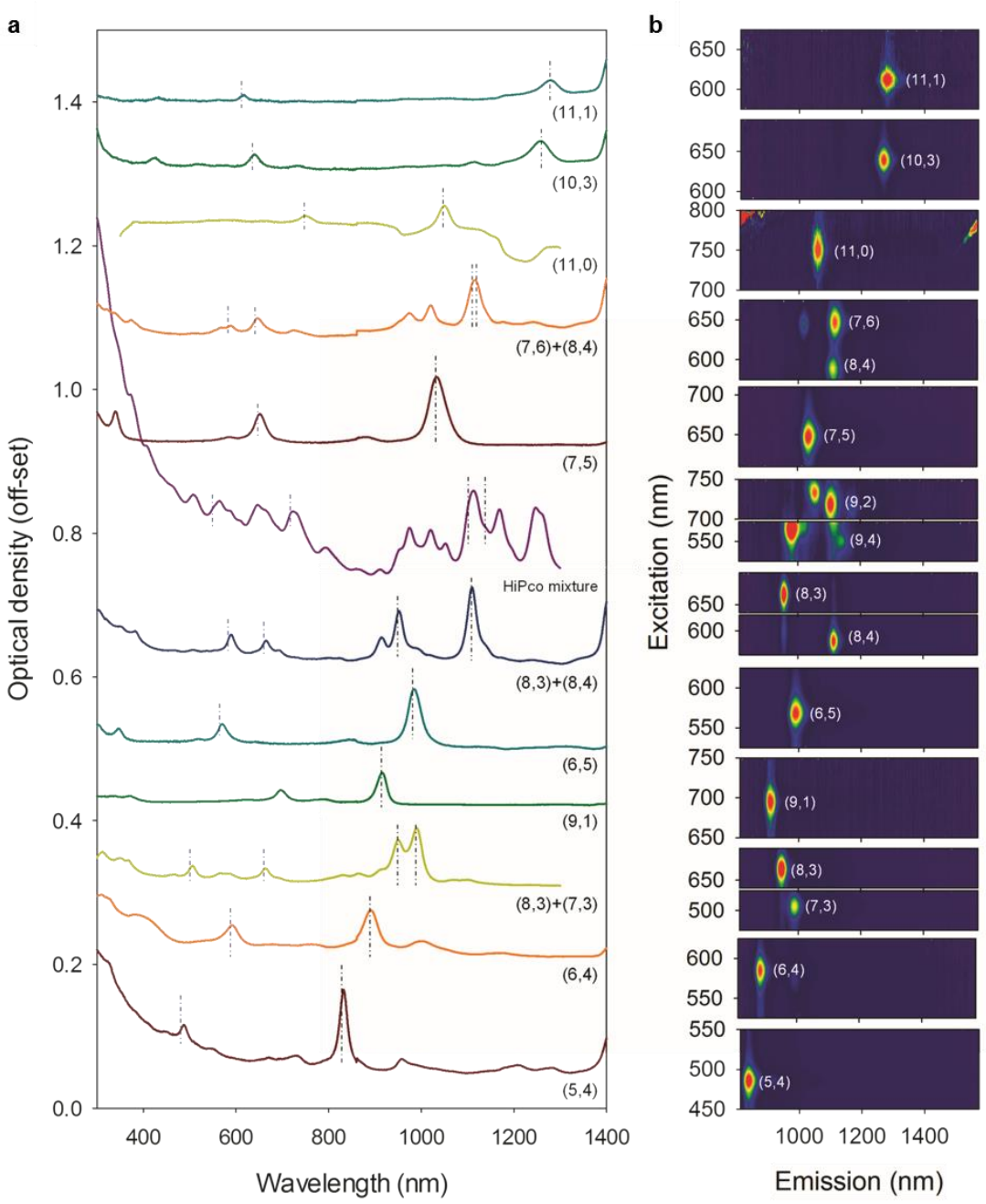

Figure 3-3 Spectral characterization of high purity SWCNT aqueous solution. **a,** UV-vis-NIR absorption spectra and **b,** excitation-emission PL maps of unfunctionalized (*n*,*m*)-SWCNTs in 1 wt/v% SDS in D_2O. The purity and abundance of each chirality can differ depending on purification methods and batch. The black and blue dashed lines in the absorption spectra denote E_{11} and E_{22} transitions, respectively.

Table 3-2 Chirality dependence of defect PL. Note that the PL spectra were obtained from SWCNTs in 1% SDS-D_2O. Note that some E_{trap} values are derived from linear extrapolation of experimentally measured series (asterisked).

(n,m)-SWCNT-$C_6H_4NO_2$

(*n*,*m*)	mod	Angle (deg)	d (nm)	E_{11} (nm)	E_{11}^- (nm)	ΔE (meV)	E_{trap} (meV)
(5,4)	1	26.3	0.620	849	1052	282	211
(6,4)	2	23.4	0.692	879	1066	247	185
(7,3)	1	17	0.706	999	1160	172	129
(9,1)	2	5.2	0.757	917	1115	240	180
(6,5)	1	27	0.757	983	1145	178	133*
(8,3)	2	15.3	0.782	955	1159	229	171
(9,2)	1	9.8	0.806	1144	1310	137	123
(7,5)	2	24.5	0.829	1025	1189	167	152
(8,4)	1	19.1	0.840	1114	1276	141	127
(7,6)	1	27.5	0.895	1124	1281	135	121
(11,1)	1	4.31	0.916	1277	1486	137	123
(10,3)	1	12.73	0.936	1266	1455	127	114

(n,m)-SWCNT-C_6F_{13}

(*n*,*m*)	mod	Angle (deg)	d (nm)	E_{11} (nm)	E_{11}^- (nm)	ΔE (meV)	E_{trap} (meV)
(5,4)	1	26.3	0.620	842	1027	265	199
(6,4)	2	23.4	0.692	879	1082	264	198
(7,3)	1	17	0.706	999	1190	198	148
(9,1)	2	5.2	0.757	925	1128	241	181
(6,5)	1	27	0.757	979	1152	190	142*
(8,3)	2	15.3	0.782	955	1169	238	178
(7,5)	2	24.5	0.829	1032	1206	173	156
(8,4)	1	19.1	0.840	1112	1284	149	134
(7,6)	1	27.5	0.895	1133	1291	134	120
(9,4)	2	17.48	0.916	1114	1270	137	123
(11,1)	1	4.3	0.916	1277	1487	137	123
(10,3)	1	12.73	0.936	1260	1445	126	113

(n,m)-SWCNT>CF_2

(*n*,*m*)	mod	Angle (deg)	d (nm)	E_{11} (nm)	E_{11}^- (nm)	ΔE (meV)	E_{trap} (meV)
(5,4)	1	26.3	0.620	835	1025	275	206
(6,4)	2	23.4	0.692	881	1097	277	208
(7,3)	1	17	0.706	1008	1211	206	154
(6,5)	1	27	0.757	983	1168	200	150

(n,m)-SWCNT-C_6H_{13}

(*n*,*m*)	mod	Angle (deg)	d (nm)	E_{11} (nm)	E_{11}^- (nm)	ΔE (meV)	E_{trap} (meV)
(6,4)	2	23.4	0.692	879	1049	228	171
(7,3)	1	17	0.706	1005	1150	156	117
(9,1)	2	5.2	0.757	923	1086	202	151
(6,5)	1	27	0.757	985	1105	137	103*
(8,3)	2	15.3	0.782	955	1124	195	146
(7,5)	2	24.5	0.829	1032	1174	145	130
(8,4)	1	19.1	0.840	1114	1228	102	92
(7,6)	1	27.5	0.895	1124	1228	92	83

(n,m)-SWCNT-$C_6H_4N(C_2H_5)_2$

(*n*,*m*)	mod	Angle (deg)	d (nm)	E_{11} (nm)	E_{11}^- (nm)	ΔE (meV)	E_{trap} (meV)
(6,4)	2	23.4	0.692	880	1053	232	174
(6,5)	1	27	0.757	987	1132	161	121*
(8,3)	2	15.3	0.782	955	1127	200	150
(7,5)	2	24.5	0.829	1032	1164	136	122
(8,4)	1	19.1	0.840	1114	1242	114	103
(7,6)	1	27.5	0.895	1124	1227	92	83

(n,m)-SWCNT-$C_6H_3(NO_2)_2$

(*n*,*m*)	mod	Angle (deg)	d (nm)	E_{11} (nm)	E_{11}^- (nm)	ΔE (meV)	E_{trap} (meV)
(5,4)	1	26.3	0.620	839	1000	238	178
(6,4)	2	23.4	0.692	876	1029	210	225*
(7,3)	1	17	0.706	880	1084	265	138
(9,1)	2	5.2	0.757	920	1169	287	215
(6,5)	1	27	0.757	985	1160	190	143*
(8,3)	2	15.3	0.782	957	1171	237	160*
(7,5)	2	24.5	0.829	1031	1192	162	146
(8,4)	1	19.1	0.840	1114	1282	146	132*
(11,0)	2	0	0.873	1058	1225	160	144
(7,6)	1	27.5	0.895	1136	1281	124	112

Figure 3-2 displays the absorption spectra and emission-excitation PL maps of three representative nanotube species: (5,4), (6,5), and (10,3). Incorporation of perfluorohexyl fluorescent quantum defects produce a new E_{11}^- PL peak at a redshifted wavelength from the native E_{11} emission of the nanotube host. The E_{11}^- peak originates from the radiative recombination of trapped excitons from fluorescent defect sites,[14] as evidenced by the fact that both the E_{11} and E_{11}^- PL peaks are correlated with the E_{22} excitation of the SWCNT in excitation-emission maps of the functionalized samples (Figure 3-2). Although the attached functional groups ($-C_6F_{13}$) are the same, the emission wavelength of E_{11}^- was found to vary dramatically with the nanotube species, which implies a correlation with the host structures.

We tabulated the emission wavelengths of E_{11} and E_{11}^- PL for the different nanotube chiralities studied and the energy difference between these two PL peaks (optical energy gap, $\Delta E = E_{11} - E_{11}^-$) in Table 3-1. The results provide a basis for an empirically determined energy plot of defect PL versus (*n,m*) chirality for semiconducting SWCNTs (Figure 3-5 and Figure 3-6). Among the species investigated here, the longest wavelength of defect PL appears at 1487 nm for perfluorohexyl functionalized (11,1) nanotubes, (11,1)-SWCNT-C_6F_{13}. The shortest wavelength of defect PL occurs at 1000 nm for (5,4)-SWCNT-3,5-$C_6H_3(NO_2)_2$. The largest ΔE value was 282 meV for (5,4)-SWCNT-$C_6H_4NO_2$, whereas the smallest was 92 meV for (7,6)-SWCNT-C_6H_{13}. This wide emission wavelength range covers the biological transparency window[12] and most of the telecommunication range,[48-49] and can be exploited for applications that require bright, high-quality light sources at near infrared wavelengths.[45,48-49,58]

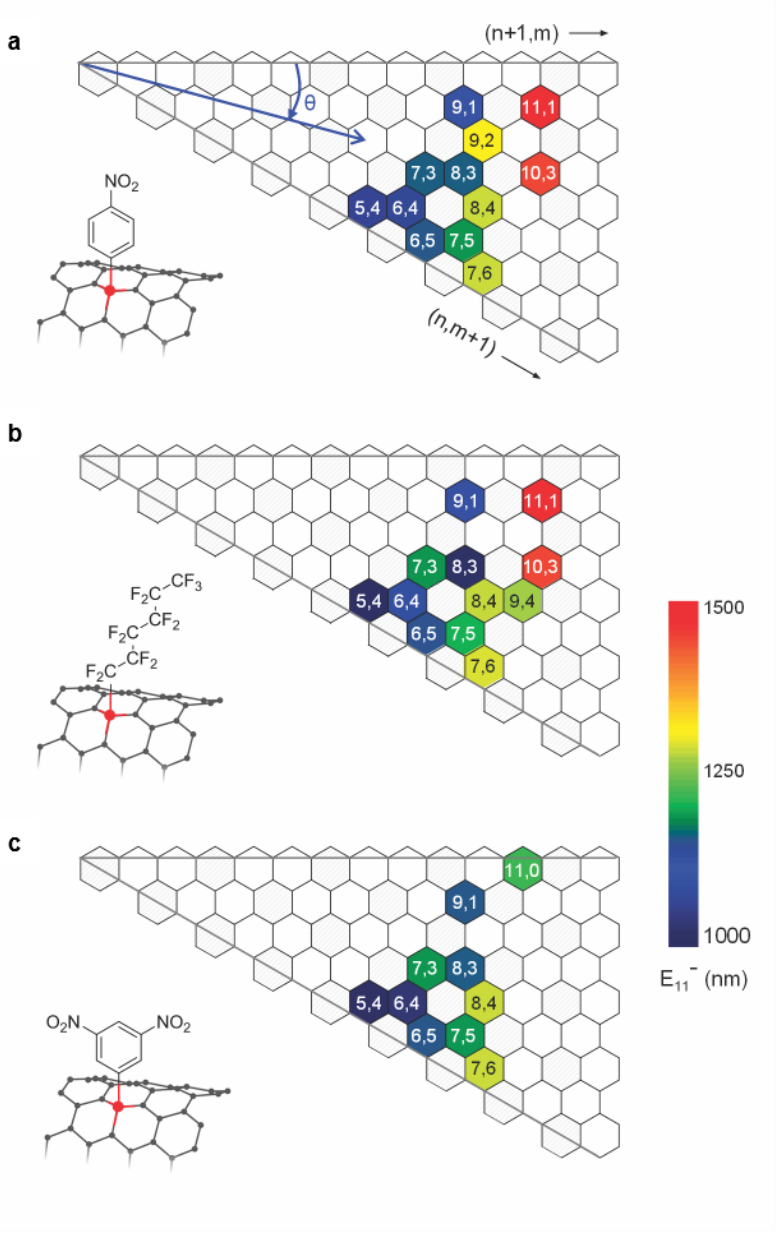

Figure 3-4 Tunable defect PL as a function of host chirality. Experimentally determined E_{11}^- wavelength of **a,** (*n*,*m*)-SWCNT-$C_6H_4NO_2$, **b,** (*n*,*m*)-SWCNT-C_6F_{13}, and **c,** (*n*,*m*)-SWCNT-$C_6H_3(NO_2)_2$ on a graphene sheet showing (*n*,*m*) lattice points. The color bar shows the emission wavelength of the defect PL. A lattice with diagonal stripes is non-emitting metallic SWCNT. A filled lattice is a semiconducting SWCNT studied in this work. The blue arrow and θ in a represent the chiral vector and chiral angle of (6,2)-SWCNTs as a demonstration of SWCNT chirality. The molecular structure of the defects is specified in each part of the figure.

3.3.2 Structure-Property Relationships of the Defect PL Emission

Each SWCNT structure can be uniquely indexed by a pair of (*n*,*m*) integers to indicate the chirality of the nanotube based on the roll-up vector of a graphene sheet (Figure 3-4). The direction of rolling determines not only the physical structure, such as diameter and chiral angle,[59] but also the electronic band structure of the nanotube.[16,55-56] Specifically, becasue a SWCNT imposes boundary conditions on the electron wave function in the direction of rolling, for semiconducting (*n*,*m*)-SWCNTs, dividing (*n* – *m*) by 3 leaves a remainder of 1 or 2, which are classified as mod (*n* – *m*, 3) = 1 and mod (*n* – *m*, 3) = 2, respectively. If (*n* – *m*, 3) is evenly divisible by 3, the SWCNT is metallic and therefore does not emit.

Covalent functionalization may break the intrinsic symmetry of the SWCNT by converting sp^2 carbons to sp^3, which modifies the energy level of the functionalized nanotube locally at the site of the defect.[14-15] At this local defect state, the optical properties, including the emission energy and the size of exciton,[37] are different from those of the intrinsic E_{11} excitons. Hence, we analyzed the structure-dependent properties of defect-trapped excitons in (*n*,*m*)-SWCNTs with perfluorohexyl, 4-nitroaryl, and 3,5-dinitroaryl defects, and mapped out the structure-dependence of the E_{11}^- emission wavelength onto the graphene lattice (Figure 3-4). The results show in general that the E_{11}^- for larger SWCNT diameters emits at longer wavelength, but it also depends on the chiral angle of the nanotube.

We observed a positive correlation between the E_{11} and E_{11}^- emission energies for the studied chiralities with the same perfluorohexyl functional groups (Figure 3-5a), indicating that the defect state is closely related to the E_{11} excitonic state. The energy

difference between E_{11} and E_{11}^{-} (ΔE) were examined for dependence on diameter (d), chiral angle (θ), and mod ($n - m$, 3). We explored the diameter dependence by fitting ΔE with the inverse second order equation of diameter (Eqn. 3-1):

$$\Delta E/\text{meV} = 11.3\ d^{-2} + 253 d^{-1} - 158\ , \qquad \text{Eqn. 3-1}$$

in which d is the SWCNT diameter in nm. Figure 3-5b shows in general an inverse correlation between ΔE and diameter. However, we also observe 28% deviation of ΔE on average from eq. 1 for the range of diameters studied, suggesting diameter alone cannot account for ΔE variation, thus the chirality effect should be considered. Although the ΔE versus chirality plot displays no obvious pattern (Figure 3-5c), we found that the deviation of ΔE is mod dependent with higher ΔE values for structures of mod ($n - m$, 3) = 2 than for mod ($n - m$, 3) = 1. This mod dependent deviation of ΔE is reminiscent of what was reported for the E_{11} energy and diameter correlation.[21,55] The mod dependent deviation represents the degree of electronic decoupling and will be discussed in the next section.

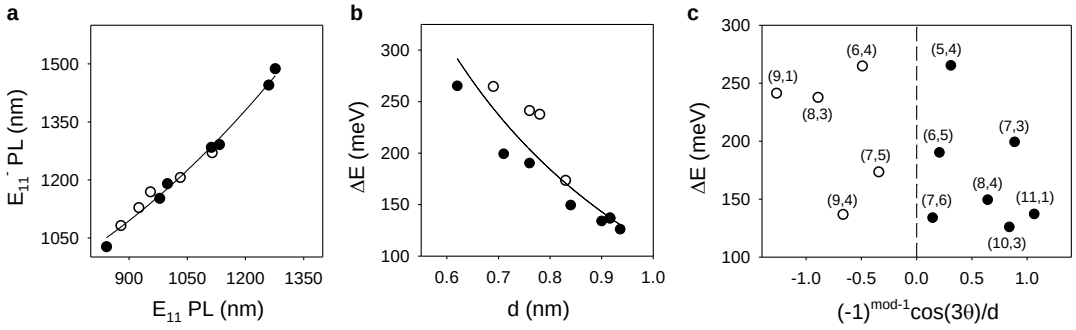

Figure 3-5 SWCNT structure relationship to perfluorohexyl defects. Closed and open circles indicate mod 1 and mod 2. **a,** Positive correlation between E_{11} and E_{11}^{-} wavelengths. The solid line is a quadratic function drawn to guide the eye. **b,** Diameter dependence of ΔE. The solid line is an empirical fitting to Eqn. 3-1. **c,** Chirality effect on ΔE. The dashed line indicates metallic armchair SWCNTs with $\theta = 30^{o}$. Each point represents different (n,m) species that are covalently functionalized with perfluorohexyl defects.

3.3.3 Exciton Trapping Potential at Fluorescent Quantum Defects

The exciton trapping potential (E_{trap}) is the minimum energy required to detrap the E_{11}^- exciton from the defect trap to restore as a free E_{11} exciton. It is an important parameter to understand the structure-related properties of excitons as well as to predict the PL stability. As established in our previous work,[60] the trapping potential of a defect state can be experimentally determined by monitoring the E_{11} and E_{11}^- PL as a function of temperature or calculated from the difference between the optical energy gap (ΔE) and the reorganization energy (λ).

Reorganization occurs due to deformation of the nanotube geometry upon exciton trapping at the defect site[60] and is related to the exciton localization at the defect site,[61-62] with greater localization presumably leading to a larger reorganization energy. When the density of defects increases, the exciton wavefunction may be delocalized across multiple defects, leading to weaker localization of excitons at the defect site and smaller reorganization energy. For the series of perfluorohexyl defect-tailored SWCNTs, we also experimentally derived a larger λ in smaller diameter SWCNTs ($d < 0.84$ nm, Figure 3-1). Such greater spatial localization of the wave function effectively increases the amount of exciton-phonon coupling and thus increases reorganization energy in small diameter SWCNTs. By linear extrapolation from the experimentally determined series (Table 3-2), we derived that the trapping potential of perfluorohexyl defect-trapped excitons ranges from 113–200 meV, as shown in Figure 3-6.

Our results suggest that the trapping potential is related to the size of the trapped exciton (electron-hole separation). For a larger trapping potential, the wavefunction of

the exciton, which can be computed using density functional theory,[60] is more spatially localized at the defect site.[37,60,63] This is congruent with our previous theoretical prediction that an E_{11} exciton of a (6,5)-SWCNT is squeezed by 17% in size when trapped at an aryl defect.[60] The inverse correlation between E_{trap} and diameter (regardless of λ values) implies that in smaller diameter SWCNTs, a defect trap can effectively reduce the exciton size and increase the oscillator strength of the defect state.[63] Strong localization at a deep trap may enhance the binding energy of the E_{11}^- exciton, and improves the stability of the defect trapped excitons. This may be related to the diameter dependent quantum yield enhancement[14] and PL stability of E_{11}^- excitons in single photon emission.[11,48] Although the photon conversion efficiency is an important parameter for many potential applications of fluorescent quantum defects, it remains a challenging and labor-intensive task,[14] which warrants the development of more efficient techniques to quantify this value. Extrapolating beyond d > 0.94 nm (the largest diameter studied here), our empirical fitting of E_{trap} (solid line in Figure 3-6a) predicts that sp^3 defects created by covalent functionalization create shallow traps in large diameter SWCNTs (e.g., few meV for d > 1.3 nm), making trapping and radiative recombination of E_{11}^- excitons less efficient.

Another interesting finding is that only a weak chirality dependence was observed for the E_{11}^- fitting. Figure 3-6b shows the empirically fitted emission energy of the E_{11} and E_{11}^- exciton as a function of diameter for 12 SWCNT chiralities that are tailored with perfluorohexyl fluorescent quantum defects. There is a clear inverse correlation between nanotube diameter and exciton emission energy. The deviation from the diameter fitting is due to the chiral angle dependence. This dependence

becomes more apparent if we group the same nanotube families ($2n + m$) with a solid line, indicating the set of SWCNTs with similar diameters but different chiral angles.[15,16,21] It is also clear that the curvature effects in E_{11}^- are less significant than those in E_{11}. These two trends may be understood by examining the electronic structure of the nanotube host and the molecular nature of the defects. The E_{11} energy levels influence the energy levels of the defect states because the defect state originates from the splitting of the doubly degenerate frontier orbitals of the SWCNT host.[1,22] and thus exhibits some degrees of chiral angle dependence that arises from the trigonal wrapping effect inherent in the host.[16] Meanwhile, once a mobile exciton is trapped at an sp^3 defect, the trapped exciton manifests photophysics that is different from the E_{11} exciton, which is governed by the sp^2 symmetry of the SWCNT lattice. Thus, our data suggest that as the defect trap becomes deeper, the exciton localization is stronger, and the optical and electronic properties of the trapped excitons become closer to an isolated zero-dimensional system with weaker dependence on the chiral angle of the nanotube host.

Finally, Figure 3-7 demonstrates that the trapping potential and emission energies of defect-trapped excitons are highly tunable depending on the chemical nature of the defects. Here we specifically studied (6,5)-SWCNT because it is easier to prepare high purity samples compared to other chiralities. The spectral characterization of all defect-tailored (6,5)-SWCNTs studied in this work is available in Table 3-3 of the Supplemental Information. We note that this correlation between the chemical natures of the defect and ΔE is observed for other chiralities as well (Table 3-2). Due to the wide choice of defects (30 different functional groups), the defect PL of (6,5)-

SWCNTs can be broadly tuned over the emission wavelength of 1094–1164 nm. We found that in general, E_{trap}, as well as the E_{11}^- wavelength and ΔE, increased as the electron withdrawing ability of the defects became stronger. The electron withdrawing ability can be quantified using Hammett constants for aryl defects[64] and Taft constants for alkyl defects.[65] From the study presented here, we show that the chemical nature of defects has a significant impact on the fluorescent quantum defects, as manifested in E_{trap} which follows a linear correlation with both Hammett (σ) (Figure 3-7a) and Taft constants (σ*) (Figure 3-7b). Combining the results of Figure 3-6 and Figure **3-7**, we derived empirical prediction models of ΔE for monovalent aryl- and alkyl-defect tailored SWCNTs. For aryl-defect functionalized SWCNTs,

$$\frac{\Delta E}{meV} = \frac{17.3}{(d/nm)^2} + \frac{235.5}{d/nm} - 146.3 + \Delta\sigma(613.2 - \frac{559}{d/nm}) , \qquad \text{Eqn. 3-2}$$

For alkyl-defect functionalized SWCNTs,

$$\frac{\Delta E}{meV} = \frac{11.3}{(d/nm)^2} + \frac{253}{d/nm} - 158 + \Delta\sigma^*(205.1 - \frac{248.6}{d/nm}) \qquad \text{Eqn. 3-3}$$

in which Δσ is σ – 0.788 and Δσ* is σ*– 4.87. Due to the chiral angle dependence of the E_{11} and E_{11}^- PL, the chiral angle dependence generates on average 9% deviation from the experimentally determined values from the diameter fitting.

Lastly, we note that bonding configuration also influences E_{trap} and E_{11}^- PL (Figure 3-7c). Divalent defects, including $>CF_2$, $>CH_2$, $>C_6H_4$, and $>C_6H_3NH_2$, tend to create deeper defect potentials and increase the exciton trapping potentials compared to their monovalent counterparts ($-CF_3$, $-CH_3$, $-C_6H_5$, and $-C_6H_4NH_2$).

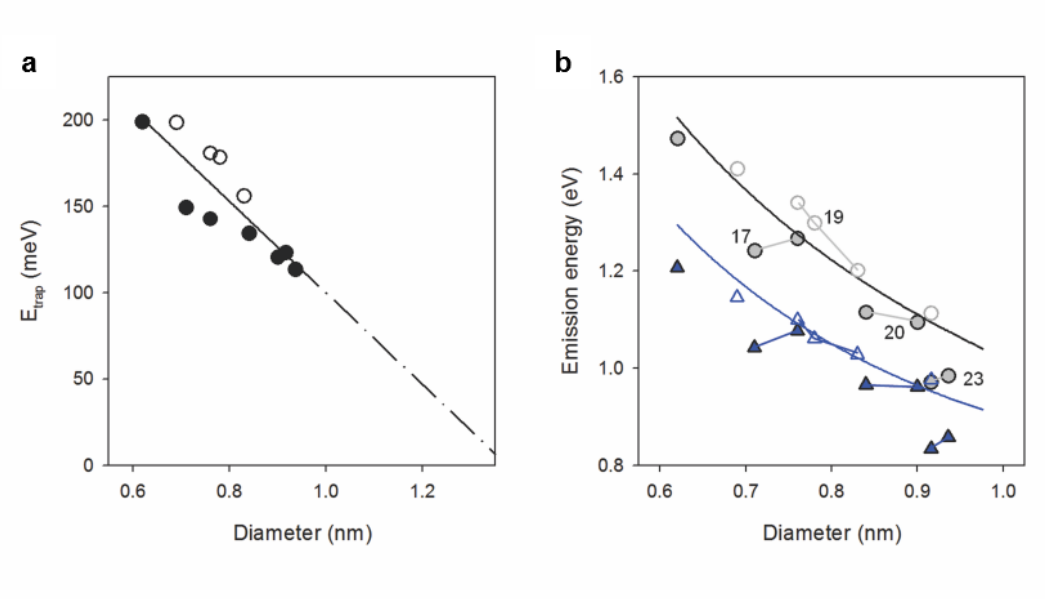

Figure 3-6 Trapping potential of E_{11}^- exciton at organic colour centres. **a,** Diameter dependence of the trapping potential of E_{11}^- excitons in (n,m)-SWCNT-C_6F_{13}. **b,** Diameter dependence of E_{11} (gray) and E_{11}^- (blue) emission energies. The labels categorize the ($2n + m$) families. Filled and open circles mark mod 1 and 2 SWCNT structures, respectively.

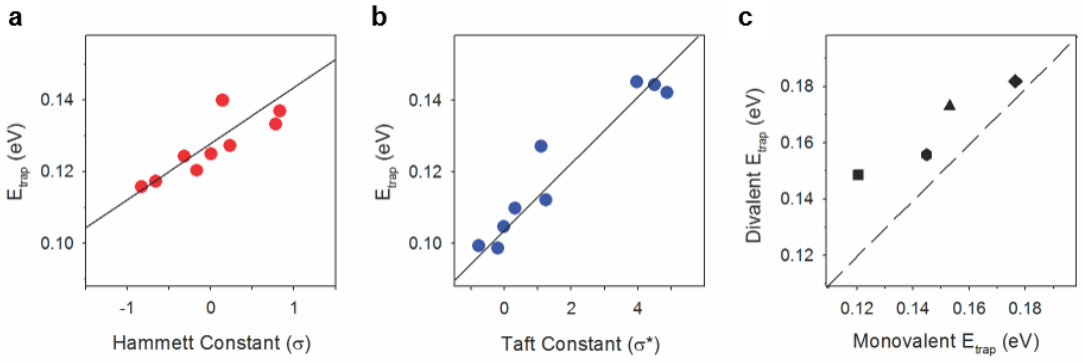

Figure 3-7 Trapping potential of E_{11}^- excitons at fluorescent quantum defects in (6,5)-SWCNT host. **a,** The inductive and resonance effects of terminating aryl moieties on E_{trap}. **b,** Inductive effects of alkyl chains on E_{trap}. The solid lines in a and b are linear fitting of the correlations. **c,** Divalent methyl (square), aminoaryl (circle), aryl (triangle), and perfluoromethyl (diamond) defects have larger E_{trap} compared to their monovalent counterparts. The dashed line is E_{trap}(monovalent) = E_{trap}(divalent) drawn to guide the eye. The correlations are also observed for other chiralities, as shown in Table 3-2.

Table 3-3 Chemical tunability of defect PL in (6,5)-SWCNTs. The position of the substituent in aryl defects is para if not specified.

(6,5)-SWCNT-aryl				(6,5)-SWCNT-alkyl			
R	E_{11} (nm)	E_{11}^- (nm)	ΔE (meV)	R	E_{11} (nm)	E_{11}^- (nm)	ΔE (meV)
$-C_6H_4-N(CH_3)_2$	990	1130	155	$-CH_3$	980	1094	132
$-C_6H_4-N(C_2H_5)_2$	987	1132	161	$-CH_2(CH_2)_2CH_3$	984	1099	132
$-C_6H_4-NH_2$	990	1132	157	$-CH_2(CH_2)_3CH_3$	981	1096	133
$-C_6H_3$-3,5-$(NH_2)_2$	990	1141	166	$-CH_2(CH_2)_4CH_3$	980	1097	135
$-C_6H_4-OCH_3$	983	1125	159	$-CH_2(CH_2)_4CF_3$	980	1099	137
$-C_6H_4-C(CH_3)_3$	983	1131	165	$-CH_2(CH_2)_4COOH$	980	1102	140
$-C_6H_4-CH_3$	983	1127	161	$-CH_2(CH_2)_2CF_3$	981	1101	140
$-C_6H_4-NHC_2H_4CONH_2$	985	1128	160	$-CH_2(CH_2)_3CF_3$	979	1104	143
$-C_6H_5$	984	1134	167	$-CH_2CH_2CF_3$	981	1110	147
$-C_6H_4-CO_2$	985	1134	165	$-CH_2(CH_2)_3CF_2CF_3$	980	1107	146
$-C_6H_4-I$	980	1131	169	$-CH_2(CF_2)_2CF_3$	980	1114	152
$-C_6H_4-Cl$	980	1130	169	$>CH_2$ (^{12}C)	979	1125	164
$-C_6H_4-Br$	982	1135	170	$>CH_2$ (^{13}C)	980	1125	163
$-C_6H_4-NO_2$	985	1147	178	$-CH_2CH_2(CF_2)_3CF_3$	983	1137	170
$-C_6F_5$	983	1150	183	$-CH_2CH_2(CF_2)_5CF_3$	983	1139	173
$-C_6H_3$-3,5-$(NO_2)_2$	985	1160	190	$-CF_2(CF_2)_6CF_3$	979	1152	190
$-C_6H_3$-2,4-$(NO_2)_2$	985	1157	187	$-CF_2(CF_2)_4CF_3$	981	1155	190
$>C_6H_3$-*o*-NH_2	986	1141	171	$-CF_2(CF_2)_2CF_3$	979	1155	193
$>C_5H_3N$	980	1145	182	$-CF_3$	980	1158	194
$>C_6H_4$	986	1162	190	$>CF_2$	980	1164	200

3.4 Conclusion

In conclusion, we have synthesized a series of fluorescent quantum defects in semiconducting SWCNTs and determined the diameter and chirality dependence of PL emission wavelengths and the thermal trapping potential for defect-trapped excitons. Similar to the native exciton (E_{11}) in unfunctionalized SWCNTs, the E_{11}^- PL is strongly correlated with nanotube diameter. The emission energy of defect-trapped excitons, however, is largely free from chiral angle and family patterns of the semiconductor host, suggesting that an exciton at an fluorescent quantum defect to some degrees decouples from the one-dimensional nanotube host. Our work establishes the structure-property relationships for fluorescent quantum defects that may help guide the controlled and tailored synthesis of this new family of quantum emitters for applications in bioimaging, quantum information, and optoelectronics in general.

4 Exciton Trapping and Detrapping at a Fluorescent Quantum Defect

Adapted from Kim, M.; Adamska, L.; Hartmann, N.; Kwon, H.; Liu, J.; Velizhanin, K.; Piao, Y.; Powell, L.; Meany, B.; Doorn, S.; Tretiak, S.; Wang, Y. J. Phys. Chem. C 2016, 120, 11268–11276

Y.W. and M.K. conceived and designed the experiments. M.K., N.H., H.K., Y.P., and L.P. performed experiments. B.M. purified carbon nanotube solution. L.A., J.L., and S.T. performed DFT calculations. K.V. constructed theoretical models. Y.W., S.K.D., and M.K. wrote the manuscript with inputs from all authors.

4.1 Introduction

A fluorescent quantum defects can trap a mobile exciton (Figure 2-10), allowing the exciton to decay radiatively *via* E_{11}^- PL. The defect PL occurs at red-shifted energies from the native PL (E_{11}).[14-15] The unique optical properties of these fluorescent defects have spurred intensive investigations on exciton trapping and brightening at defect sites.[37,62,66-70] Beyond a desire to understand the origins and behavior of this novel emission, studies are motivated by the promise defect emission holds for photonic, optoelectronic, sensing, and imaging applications, afforded by potential for enhanced quantum yields,[14,37,69,71] new functionality,[45] and as photon upconversion[72] and quantum light sources.[48-49]

An important aspect of defect-induced photophysics that remains to be understood is determining the factors underlying exciton trapping. In particular, we seek to understand the depth of the trapping potential and how it impacts the observed emission behavior. Trap depth is a determining factor in such fundamental behavior as

the degree of exciton localization and for relaxation processes or impact on band positions (of relevance to dopant-site redox behavior and potential impact on energy harvesting ability).[68] Trap depth can also impact the quality and stability of defect PL emission.[48,62] Furthermore, thermal detrapping is an important step in recently observed photon upconversion from similarly defect-engineered SWCNTs.[72] Studies of thermally-induced exciton detrapping in oxygen-doped and alkylated nanotubes indicate the trap depth is significantly lower, with detrapping energies ($\Delta E_{thermal}$) being less than 50% of $\Delta E_{optical}$ (energy difference between E_{11} and E_{11}^-, marked in Figure 4-1b).[69,71] Combined experimental and theoretical studies of the defect-site redox behaviors also indicate a reduction in bandgap that is significantly smaller than the associated optical energy shift.[68] While a simplistic picture of ground-state perturbation of exciton energies at the oxygen dopant site provides an initial understanding of the difference in observed energies,[71] the origin of the large discrepancy between $\Delta E_{optical}$ and $\Delta E_{thermal}$ is not yet established.

Herein, we quantitatively probe the thermal activation of defect-trapped excitons as a function of the chemical nature and density of defects and generalize the behavior to a new class of defects. A series of fluorescent aryl defects were chemically created in (6,5)-SWCNTs through controlled diazonium chemistry.[14] Detrapping energies for each defect type are derived from van ‘t Hoff plots constructed based on the intensity ratio of E_{11} and E_{11}^- PL as a function of temperature. The measured detrapping energies are directly correlated with the optical gaps $\Delta E_{optical}$ determined from defect PL. We found that both $\Delta E_{optical}$ and $\Delta E_{thermal}$ are linearly dependent on the electron-withdrawing nature of specific functional groups, as measured by the

Hammett substituent constant. At relatively high defect densities, $\Delta E_{thermal}$ is more than half of $\Delta E_{optical}$. However, we found a strong dependence of the energy mismatch on defect density, with differences between $\Delta E_{thermal}$ and $\Delta E_{optical}$ on the order of 100 meV found in the low-density limit. Based on these observations, we propose a theory that highlights as the origin of the $\Delta E_{thermal}$ and $\Delta E_{optical}$ energy difference a substantial vibrational reorganization energy between the excited and ground state of SWCNTs in the presence of a fluorescent defect. This proposed origin is supported by density functional theory (DFT) calculations of reorganization energies that agree with the experimental trends and magnitude of measured trapping energies.

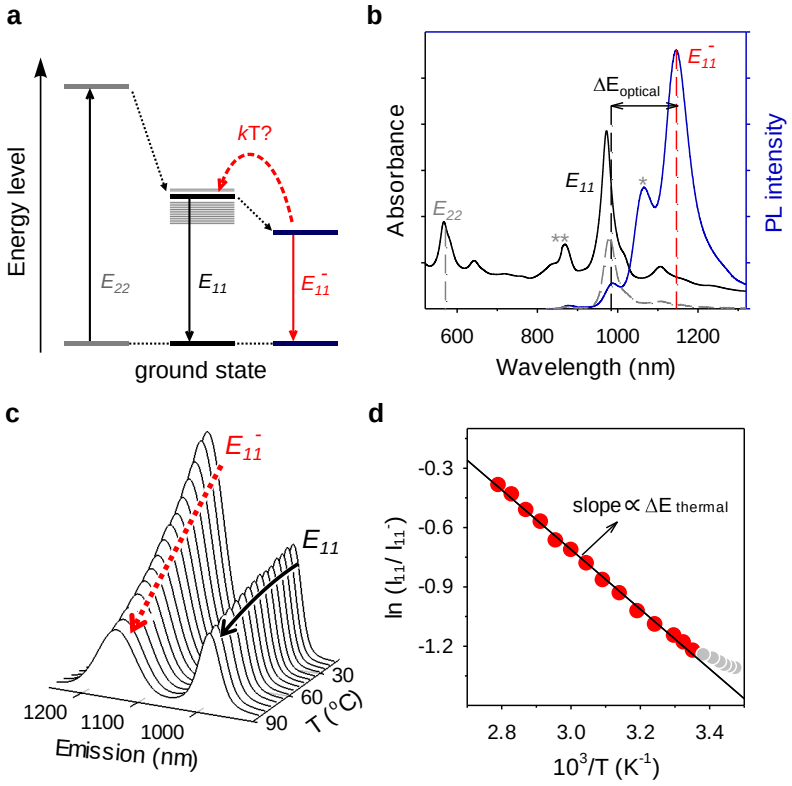

Figure 4-1 Temperature dependence of defect PL in functionalized SWCNTs. **a,** Energy diagram of a SWCNT with a fluorescent quantum defect: An exciton trapped at the defect level (E_{11}^-) can thermally escape the quantum defect well and recombine via the bright singlet exciton channel (E_{11}). **b,** UV-vis-NIR absorption (black) and vis-NIR photoluminescence spectra of (6,5)-SWCNT-$C_6H_4NO_2$. **c,** Peak fitted PL spectra of (6,5)-SWCNT-$C_6H_4NO_2$ (synthesized from [Dz]:[C] = 1:500) at increasing temperatures with 5°C increments. **d,** The van 't Hoff plot as derived from the PL spectra in Figure **c**. Open circles where surfactant reorganization effects are dominant are excluded for calculating the potential well depth.

4.2 Experimental Section

4.2.1 Chirality-Enriched Carbon Nanotubes

HiPco SWCNTs (Rice University, batch #194.3) were sorted using Sephacryl^{TM} S-200 high-resolution chromatography resin (GE Healthcare), as described previously,[28] to produce (6,5)-SWCNTs enriched samples. The purified SWCNTs were stabilized as individual nanotubes in D_2O (Cambridge Isotope Laboratories, Inc., 99.8%) by 1 wt.% sodium dodecyl sulfate (SDS) for subsequent studies. Alternatively, a polymer aqueous two-phase (ATP) separation process[25,30] was used also to generate (6,5)-SWCNTs enriched material used for doping with ozone and covalent functionalization with 3,5-dichlorobenzenediazonium tetrafluoroborate. After chirality isolation the SWCNTs were exchanged into 1 wt.% SDS in Millipore H_2O or 1 wt.% sodium dodecylbenzenesulfonate (SDBS) in Millipore H_2O surfactant environment *via* pressure filtration (100 kDa regenerated cellulose membrane).

4.2.2 Chemical Creation of Fluorescent Aryl Defects in SWCNTs

Aryl defects were created through controlled functionalization of SWCNTs with aryl diazonium salts as we previously described.[14] We note that a modified functionalization protocol[62] was used for (6,5)-SWCNT-$C_6H_3Cl_2$, which was suspended by 1 wt/v% sodium deoxycholate (DOC) while in all other cases the functionalized nanotubes were stabilized by 1 wt.% SDS. Briefly, the concentration of (6,5)-SWCNTs was adjusted to give an optical density of 0.1 at the E_{11} absorption. A 4-nitrobenzenediazonium tetrafluoroborate (4-$C_6H_4NO_2N_2^+ \cdot BF_4^-$) solution was then added to this nanotube solution for a starting molar ratios of reactants, [Dz,

diazonium]/[C, nanotube carbon], at 1:4,000, 1:2,500, 1:1,500, 1:1,000, 1:750, 1:500 and 1:250. These reactant ratios were slightly adjusted for the other diazonium salts to accommodate the difference in reactivity. The reaction occurs at room temperature with a pH of 5.5 and was monitored by following the defect photoluminescence with a NanoLog spectrofluorometer (Horiba Jobin Yvon) and UV-vis-NIR absorption with a Lambda 1050 UV-vis-NIR spectrophotometer (PerkinElmer). The corresponding Raman D/G ratio was calculated from Raman spectra collected under both 532 nm and 633 nm excitation (LabRAM ARAMIS Raman microscope, Horiba Jobin Yvon).

4.2.3 Introduction of Oxygen Defects in SWCNTs

Oxygen dopants were introduced by following a doping protocol described previously.[71] (6,5)-SWCNTs in 1 wt.% SDBS (OD of 0.04 at E_{11}) were diluted with nanopure H_2O to a concentration of 0.2 wt.% SDBS. Ozonated nanopure H_2O was then added with a volume ratio of 1:1. The reaction mixture was illuminated for 4 h by a quartz-tungsten halogen lamp and subsequently quenched by pressure filtration through a 100 kDa cellulose membrane using 1.04 wt.% DOC solution as eluate.

4.2.4 Temperature-Dependent Photoluminescence Spectroscopy

To probe the energy levels of fluorescent aryl defects, both the defect (E_{11}^-) and original (E_{11}) PL were collected as a function of solution temperature. The temperature of the nanotube solution was controlled using a circulating water bath stage (FL-1027, Horiba Jobin Yvon). The temperature was measured with an immersion Surface Temperature Sensor and LabQuest 2 (Vernier). At each 5 ^oC increment from 15 ^oC to 85 ^oC, a photoluminescence spectrum was collected. The E_{11} and E_{11}^- were fitted with

Voigt profiles using Peakfit v4.12 (SeaSolve), and the integrated intensity ratios were plotted against temperature.

4.2.5 Quantum Chemical Modeling

The computations were performed using Gaussian 09 software suite.[73] A 10 nm long (6,5)-SWCNT segment, with open ends terminated by hydrogen atoms, was used. The system contained about 1000 carbon atoms. Density functional theory (DFT) calculations were done using Coulomb-attenuated B3LYP functional[74] and STO-3G basis set. The optical transitions were computed using time-dependent DFT (TD-DFT). If not mentioned otherwise, the calculations were done in vacuum. Some test cases have utilized solvents effects in the framework of conductor-like polarizable continuum medium model[75] using experimentally relevant water solvent. The functional group was added in the middle of the nanotube. In the case of oxygen doping, only the lowest energy structure (named ether-d in ref.[71]) was studied. In the case of aryl defects, we show the results for a special defect configuration consisting of 4-bromoaryl ring and hydrogen atom added to the nearest neighbor carbon along the tube axis.

4.2.6 Characterization of Defect Density through Raman Spectroscopy

Raman spectra were collected from solid SWCNT samples using a Raman microscope (Horiba Jobin Yvon, LabRAM, ARAMIS) in duo scan mode, which averages spectra from a 30×30 μm^2 area. Each data was sampled from at least 5 different regions and averaged to ensure data is statistically meaningful. The excitation wavelengths were 531 nm and 632.8 nm.

4.3 Results and Discussions

4.3.1 Defect Detrapping Energy Derived from Temperature Dependence of PL evolution

To determine the defect detrapping energy, we measured the PL spectra at 5 °C increments (over a temperature range from 15 to 85 °C) and constructed van 't Hoff plots based on the intensity ratio of the E_{11} and E_{11}^- PL as a function of temperature (Figure 4-1). We note that the PL intensities discussed here are integrated PL intensities. The van 't Hoff analysis is routinely applicable to an effective two-level system at thermal equilibrium where at finite temperature the ratio of populations of two states is given by a Boltzmann exponent, exp(−ΔE/kT), where ΔE is the energy between the two states. For the case of SWCNTs that involve trapped (E_{11}^-) and free (E_{11}) excitons the situation is more complicated since the "upper state", *i.e.*, the free exciton, is not a single state, or a discrete number of states, but a continuum of freely moving excitons with a thermal distribution of kinetic energies. The partition function for such a system is given by[76]

$$Z = Z_t + Z_f = Ln_d + \frac{L}{\pi\hbar} e^{-\Delta E/kT} \left[\int_0^\infty dp\, e^{-p^2/2MkT}\right]^N \qquad \text{Eqn. 4-1}$$

where the first right-hand side term is the number of defect sites (n_d is the concentration of defect sites and L is the SWCNT length). The dimensionality of the system is denoted by N (1 in the case of SWCNT). The second right-hand-side term represents the summation over the thermally excited free exciton states, where M is the exciton total mass, k is the Boltzmann constant, and T is temperature. The integral here can be evaluated exactly, leading to the ratio of trapped and free exciton populations as

$$\frac{p_f}{p_t} = \frac{Z_f}{Z_t} \propto T^{N/2} e^{-\Delta E/kT} \qquad \text{Eqn. 4-2}$$

with the result being similar to the classical result for a thermally excited population of electrons in an extrinsic n-type semiconductor.[76] The ratio of populations in Eqn. 4-2 is not exactly of the van 't Hoff type. However, the population of excitons is not what is directly accessed experimentally. Instead, what is analyzed is the ratio of photoluminescence intensities, which is essentially different from the ratio of populations if the oscillator strengths are temperature-dependent. The oscillator strength of the zero-dimensional trapped exciton is constant. However, thermally excited free excitons are decoupled from photons, so the average oscillator strength of free excitons in a 1D system (*e.g.*, SWCNT) is proportional to $1/\sqrt{T}$.[77-79] The result is that the square roots of temperature, originating from the ratio of populations, and from the oscillator strength considerations, cancel each other, resulting in the ratio of PL intensities being the Boltzmann factor:

$$I_{11}/I_{11}^{-} \propto \exp(-\Delta E/kT) \qquad \text{Eqn. 4-3}$$

in which I_{11} and I_{11}^{-} are the integrated PL intensities of E_{11} and E_{11}^{-}. Therefore, the energy between the trapped and free excitonic states can be effectively derived by the van 't Hoff method. This energy difference is denoted as $\Delta E_{thermal}$ to differentiate it from the optical gap $\Delta E_{optical}$, which is determined from the emission energies. We note that this analysis neglects the possibility of dark exciton and trap states, which will introduce additional temperature dependences to observed PL intensities at low temperatures.[37,80-81] In the temperature range of our experiments, however, such an approximation is suitable. We further note that this van 't Hoff analysis can be skewed toward smaller $\Delta E_{thermal}$ if there exists an inhomogeneous distribution of trap depths.

This effect is minimized here by integrating over the entire line width of the emission to better account for the contribution from the entire population of both native excitons and defect-trapped excitons. Quantification of this effect may be possible by applying similar techniques as developed by Graham *et al.* and Schilling *et al.* to determine the inhomogeneous broadening of the native exciton (E_{11}) band due to a distribution of energy barriers.[82-83] Experimentally, we found that the PL of aryl-tailored nanotubes systematically responds to changes in the solution temperature. Above 25 °C, the PL intensity of both E_{11} and E_{11}^- gradually decrease with temperature (Figure 4-1c), but the relative decrease is more rapid for E_{11}^-. The behavior of E_{11} is due to the $1/\sqrt{T}$ intensity dependence, as discussed above, while the intensity loss in E_{11}^- arises from thermally induced exciton detrapping from the defect site. As shown in Figure 4-1d, the integrated intensities of E_{11} and E_{11}^- PL are correlated with temperature by the following van 't Hoff relation:

$$ln\frac{I_{11}}{I_{11}^-} = -\frac{\Delta E_{thermal}}{kT} + A' \qquad \text{Eqn. 4-4}$$

in which A' is a correction factor. The slope of the van 't Hoff plot thus provides the thermal detrapping energy equal to 131 meV for (6,5)-SWCNT-$C_6H_4NO_2$.

4.3.2 Defect Detrapping Energy as a Function of the Chemical Nature of Defects

The ability to synthetically tune the aryl dopants to alter optical properties provides a route to probe the generality and structural dependences of the $\Delta E_{thermal}$ behavior. We constructed van 't Hoff plots for a series of seven fluorescent aryl defects with different substitutional moieties (Figure 4-2). In all cases, a good linear fit to Eqn.

4-3 is found, allowing $\Delta E_{thermal}$ to be extracted for each dopant (see Table 4-1). We found that $\Delta E_{thermal}$ is linearly correlated with the electron-withdrawing capabilities of the terminating groups, as measured by the Hammett constant (σ).[84] As σ_p increases from −0.83 for 4-N,N-diethylamine to 1.42 for 3,5-dinitro, $\Delta E_{thermal}$ increases by 41 meV (Figure 4-3, red data, and also Table 4-1). This trend in $\Delta E_{thermal}$ closely traces what was observed with $\Delta E_{optical}$ (Figure 4-3, black data). As σ_p increases, the magnitude of $\Delta E_{optical}$ also increases (see also Table 4-1) and directly parallels the change observed in $\Delta E_{thermal}$. In our previous experiments it was concluded that a larger σ_p could effectively lower the E_{11}^- state, creating a deeper trap for excitons.[14] The linear correlation between $\Delta E_{thermal}$ and $\Delta E_{optical}$ thus consistently suggests that greater energy will be required for an exciton to thermally escape a deeper trap, as expected. Of significant interest, However, is the observation of a large energy offset of ~45 meV between $\Delta E_{thermal}$ and $\Delta E_{optical}$ that remains nearly constant for each type of aryl defect. Notably, in all cases, the magnitude of the observed $\Delta E_{thermal}$ values are significantly lower (on the order of 70%) than the corresponding $\Delta E_{optical}$ values (Figure 4-3). This energy mismatch across the aryl defect series is also larger than that reported by the Weisman group for oxygen-doped nanotubes.[71] We note that in Figure 4-1d and Figure 4-2, for temperatures below 25 °C, the intensity ratio of E_{11} to E_{11}^- begins to rise again as the temperature is lowered further. This behavior is likely due to surfactant reorganization at low temperatures.[85-88]

Here, we conclude that the energy mismatch between $\Delta E_{thermal}$ and $\Delta E_{optical}$ is now seen as a general phenomenon over a wide range of defect tailored SWCNTs.

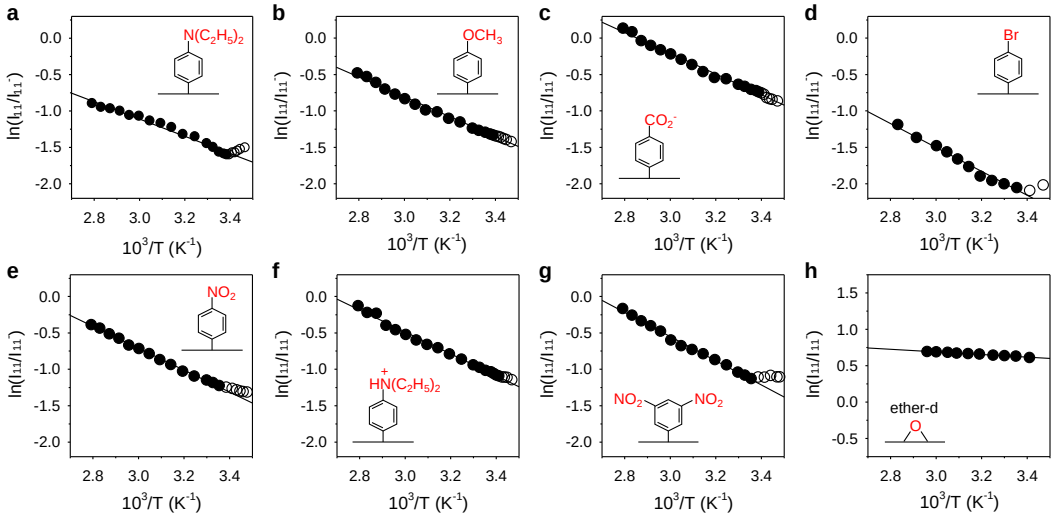

Figure 4-2 van 't Hoff plots for fluorescent quantum defect-labeled (6,5)-SWCNTs. The chemical nature of the defect is given in each plot. The defect density is maintained at a similar level for the aryl functional groups (**a-g**). The defect density for the O-doped sample (**h**) is at a lower level

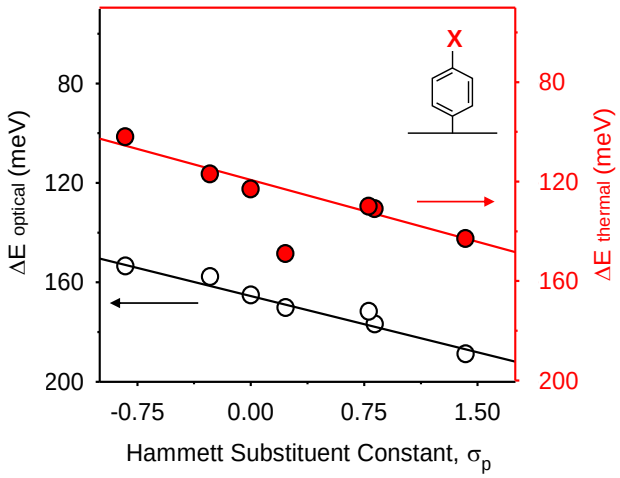

Figure 4-3 Correlations of optical gaps ($\Delta E_{optical}$, black open circles) and thermal detrapping energies ($\Delta E_{thermal}$, red closed circles) as functions of the chemical nature (as measured by σ_p) of fluorescent aryl defects. The defect density of each (6,5)-SWCNT sample was adjusted to produce $I_{11}^-/I_{11} > 2$.

Table 4-1 Tabulation of trap site optical emission energies (E_{11}^-), optical band gaps ($\Delta E_{optical}$), thermally-determined trapping energies ($\Delta E_{thermal}$), and experimentally determined reorganization energies (λ) for various fluorescent defects (X).

X**	E_{11} (nm)	E_{11}^- (nm)	$\Delta E_{optical}$ (meV)	$\Delta E_{thermal}$ (meV)	λ (meV)
O-doped (low)*	994	1125	146	24	122
-NEt_2	989	1127	154	102	52
3,5-Cl_2 (low)*	992	1133	155	35	120
3,5-Cl_2 (high)*	992	1133	155	134	21
-OCH_3	988	1130	158	117	41
-CO_2-	992	1143	165	123	42
-Br	988	1143	170	149	21
-NO_2 (low)*	982	1139	174	76	98
-NO_2 (high)*	981	1141	177	131	46
-$HNEt_2^+$	989	1146	172	130	42
3,5-$(NO_2)_2$	988	1163	189	143	46

*Values for $\Delta E_{thermal}$ and λ for these fluorescent defects are given for high and/or low defect density cases. The low density limit is most directly comparable to the DFT results of Table 2. All other values were obtained at relatively high defect densities, where $I_{11}^-/I_{11} > 2$ at 25°C

**X represents the terminating moieties of an aryl defect except for an oxygen dopant (ether-d).

4.3.3 Potential Energy Surface Model for Excitons

Figure 4-4 depicts the energy diagram of defect tailored SWCNTs in terms of overlapping molecular-like potential surfaces for free and trapped excitons. Such a molecular view has been demonstrated as useful for understanding certain aspects of free exciton behavior in carbon nanotubes[89] and is particularly appropriate for an exciton localized at a trap site. Within this view, the energy mismatch may be interpreted to arise from major contributions from reorganization energy at the defect site. Consider the electronic terms of our system. These may include the potential energy surfaces for the ground state (G), defect-trapped (X^-) exciton, and free exciton (X), as schematically presented in Figure 4-4. The "configuration coordinate" (r) has been arbitrarily chosen as zero at the optimal ground state geometry, so that the energy minimum of the ground state parabola is located at r = 0. Thus, coordinate r represents the distortion of the SWCNT geometry relative to the ground state geometry.

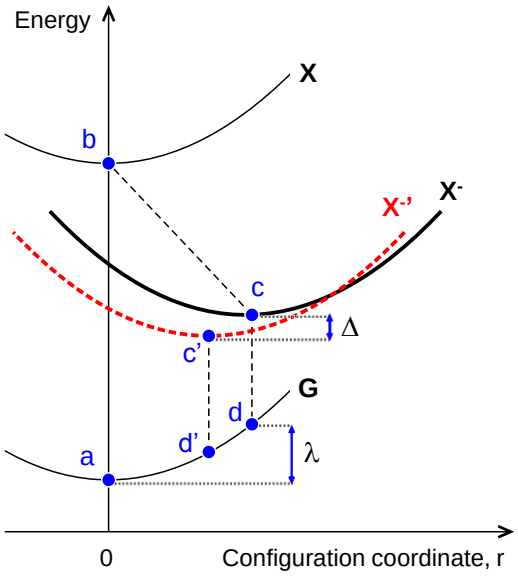

Figure 4-4 Potential energy surfaces for ground (G), trapped exciton (X^-), and free exciton (X). "Configuration coordinate" r (horizontal axis) denotes the deformation (reorganization) of the SWCNT geometry. Here the reorganization energy is dominated by displacement of nuclear coordinates since changes in vibration frequency, or curvature of potentials, are negligible in rigid systems such as SWCNTs. Note that the energy separations between the states are not to scale.

Following initial optical excitation to X, diffusional transport to a defect site results in exciton trapping and relaxation to state X^-.[37,62,70] We focus on energies associated with thermal activation out of X^- to X or relaxation from X^- to G via emission of a photon. Because of exciton−phonon coupling, the minima of the excited state parabolas are in general located at finite r. Trap state PL originates from the optimal geometry of the X^- state (point c in Figure 4-4). Because of the Franck−Condon principle, the optical transitions are "vertical." The defect state emission process, therefore, occurs between point "c" of the X^- curve and point "d" of the ground state surface, with energy $E_{cd} = E_c - E_d$. Point "d" represents an excited state geometric configuration of the ground state surface. Its energy difference with the ground state

equilibrium configuration at point "a" (E_{da}) represents the reorganization energy λ for the transition between X^- and G electronic terms. Our defined $\Delta E_{optical}$ is therefore equivalent to $E_{ba} - E_{cd}$. Thermal activation out of the trap state, on the other hand, is a slow process relative to optical excitation, and the Franck−Condon principle is thus invalid for thermal detrapping. The required thermal activation energy is therefore equivalent to the energy difference between the minima of the X and X^- curves: $E_{bc} = \Delta E_{thermal}$. Referring to Figure 4-4, the difference between the optical and thermal activation energies is

$$\Delta E_{optical} - \Delta E_{thermal} = (E_{ba} - E_{cd}) - E_{bc} = E_{da} = \lambda > 0 \qquad \text{Eqn. 4-5}$$

We note that in arriving at Eqn. 4-5, we have neglected for simplicity any independent reorganization energy associated with optical excitation of the initial E_{11} excited state at point "b" of the X curve. This is a reasonable approximation, as the relatively delocalized nature of the E_{11} exciton (in contrast to that of the trap state) naturally leads to a reduced reorganization energy. Such a simplification is supported by experimental observations of small Stokes shifts (~8 meV) in E_{11} emission[90] and by Raman studies showing weak exciton− phonon coupling.[91]

Inspection of Figure 4-4 thus suggests that the origin of the mismatch in $\Delta E_{optical}$ vs $\Delta E_{thermal}$ is due to a reorganization energy component associated with the optical transition. Such an energy cost is expected from the associated large coordinate changes that should arise from significant localization of the exciton wave function imposed by trapping.[62,70] We note that while we have discussed changes in the reaction coordinate r (Figure 4-4) as arising from a distortion of the SWCNT geometry, other contributions can exist, including solvent polarization and surfactant reorganization as examples.

Any such contribution can only increase the total observable reorganization energy, so the final expression for the difference between the optical gap and the detrapping energy would be

$$\Delta E_{optical} - \Delta E_{thermal} = \sum_i \lambda_i > 0 \qquad \text{Eqn. 4-6}$$

where each contribution λ_i is positive.

4.3.4 Quantum Chemical Modeling of the Functionalized SWCNTs

From the measured $\Delta E_{thermal}$ and $\Delta E_{optical}$, we can further derive that the reorganization energy can be on the order of 50 meV (Table 4-1) and, in the limit of low defect density, can be as large as 100 meV. While $\Delta E_{optical}$ and $\Delta E_{thermal}$ have similar origins in the trap state, they are nevertheless physically distinct, as they describe vertical and nonvertical transitions, respectively. In particular, Eqn 4-5 and 4-6 imply that $\Delta E_{optical}$ is always larger than $\Delta E_{thermal}$, which is consistent with our experimental observations and those of Ghosh *et al.*[71] Furthermore, it is important to recognize that our proposed model based on Figure 4-4 indicates that the experimentally determined thermal barrier most closely equates to the actual depth of the trapping potential. As described below, our DFT results further support this interpretation. Our previous computational studies of oxygen-doped or defect-tailored carbon nanotubes have provided a detailed view on the structure and properties of SWCNT excited states and electronic levels at defect sites.[13-14,62,70,92-93] Here we focus on the vibrational relaxation of ground and excited electronic states in representative examples. The reorganization energy (λ) is computed as the difference of total energies of the system in the ground state, at the ground state optimal geometry (r = 0 in Figure 4-4) and in the ground state,

but at the configuration coordinate (r) corresponding to the optimal geometry of the excited state X^- (point d in Figure 4-4), which directly corresponds to the definition given by Eqn 4-5. Ground and excited state optimal geometries were obtained using DFT and time-dependent DFT (TD-DFT) formalisms, respectively. The relevant computational details are provided in Experimental Section. In addition to the pristine 10 nm long (6,5) tube, we have considered oxygen-doped (ether-d) and 4-bromoaryl ($-C_6H_4Br$) defect-tailored species. In the pristine SWCNT, we consider the lowest electronic states. Here the calculated λ of the E_{11} exciton is 13 meV. This supports our earlier approximation where this quantity was neglected. When defects are introduced, we observe lower energy electronic states in our calculations. Specifically, the lowest state (E_{11}^-) in the aryl defect tailored tube has substantial oscillator strength and thus is emissive. In stark contrast to the E_{11} exciton of a pristine tube, λ for E_{11}^- is substantially larger, being 101 meV (see Table 4-2).

Miyauchi et al. suggests the occurrence of bright and optically forbidden (dark) defect states for oxygen-doped tubes.[37] Our DFT results also indicate this. Interestingly, for oxygen-doped nanotubes the dark defect state is energetically below the emissive state while for aryl defects, the bright defect state is the lowest. At the optimal geometry of the dark state, we find the lowest electronic transition in oxygen-doped tubes in the ether-d geometry is this dark state, whereas the optically allowed E_{11}^- transition is state number 2. The calculated splitting between these bright and dark states at this geometry is 13 meV. These results are in agreement with ref [37], which suggested the existence of a dark state at 16 meV below the E_{11}^- transition for oxygen-doped tubes. We calculate a small λ of 18 meV in the ether-d geometry for the dark state. In contrast, at the optimal

geometry for the bright state, the ordering of the states is reversed, with the bright state found to cross the dark state and become the lowest energy dopant state. The bright state optimized geometry is found to occur at a larger configuration coordinate (r, Figure 4-4). Consequently, the reorganization energy of the bright E_{11}^- transition (70 meV) is larger than that of the lowest energy dopant state for oxygen-doped SWCNTs.

To rationalize the observed trends in λ and to link them to the underlying wavefunction properties, we further analyze calculated transition density matrices corresponding to the excitonic wavefunctions of the excited states. These quantities for native E_{11}, ether-d E_{11}^- and 4-bromoaryl ($-C_6H_4Br$) defect E_{11}^- excitons are depicted in Figure 4-5a thru c, respectively. In these plots, the horizontal and vertical axes correspond to electron and hole coordinates, respectively. The diagonal size of the matrix corresponds to the delocalization of exciton wave function along the SWCNT axis, and the width of the matrix reflects electron-hole separation, which is about 1-2 nm in all cases. We observe that the native E_{11} exciton is delocalized over about 6 nm (Figure 4-5a). For the dark E_{11}^- excitons in the oxygen-doped tube (state 1) we find a localization to about 3 nm in size (Figure 4-5b). Moreover, both the bright E_{11}^- excitons in the oxygen-doped tube (state 2) and for the aryl defect tailored tube are localized even more, on about a 1 nm length scale (see Figure 4-5c). Such spatial localization of the wavefunction effectively increases the amount of exciton-phonon coupling and thus increases reorganization energy across these cases.

Table 4-2 Calculated reorganization energies for pristine and functionalized (6,5)-SWCNTs.

Dopant System	λ (meV)
Pristine	13
Ether-d (state 1, dark)	18
Ether-d (state 2, bright)	70
2×(C_6H_4Br+H) (1 nm spacing)	28
2×(C_6H_4Br+H) (2 nm spacing)	78
2×(C_6H_4Br+H) (3 nm spacing)	92
Single isolated -C_6H_4Br+H	101
Isolated -C_6H_4Br+H with solvent	125

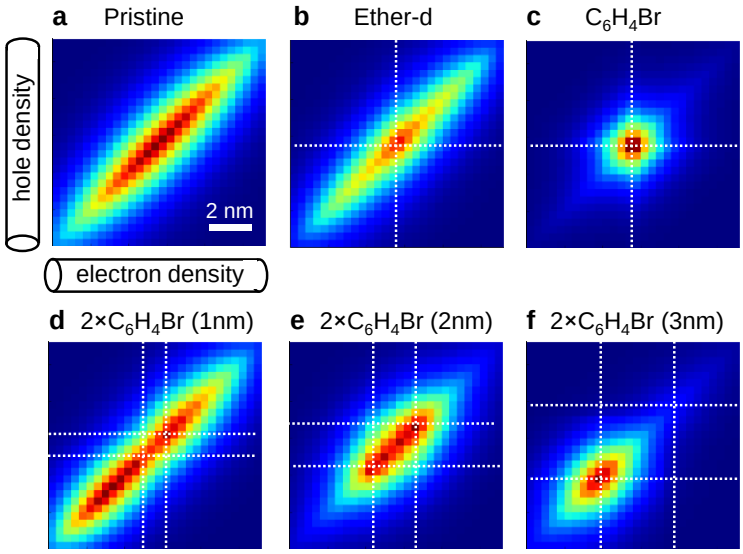

Figure 4-5 Exciton plots of optically active states in a pristine (6,5)-SWCNT (**a**), and the lowest electronic transitions for oxygen-doped (**b**) and 4-bromoaryl defect (denoted as –C_6H_4Br) tailored (**c-f**) 10 nm long (6,5)-SWCNTs. Horizontal (vertical) axis corresponds to the distribution of electron (hole) density along nanotube axis. White dashed lines mark the positions of dopants. The size of one pixel is 0.4 nm.

Finally, we investigated computationally the effect of defect density in aryl defect tailored SWCNTs on the value of λ. We have used two C_6H_4Br+H defects on a single (6,5)-SWCNT separated by 1, 2, and 3 nm distance. The computational results are summarized in Table 4-2. Our analysis shows that if the two defect sites are situated closely to each other, at distances comparable to the exciton size at the defect site, their electronic states overlap and strongly interact. Subsequently, the lowest optical transition with E_{11}^- character becomes delocalized between the two sp^3 defects as shown in Figure 4-5d, suggesting a reduced exciton-phonon coupling. As a result, the reorganization energy is strongly reduced from 101 meV to 28 meV. When the distance between defects increases, λ gradually increases and approaches the value found for isolated sp^3 defects (~100 meV). For example, λ is equal to 78 meV for defects separated by 2 nm distance. Here, the exciton wave function is contained to about 2 nm length (Figure 4-5e). For larger separation distances, the defect sites become uncorrelated and the vibrational dynamics is contained to a single site. For example, Figure 4-5f shows that the exciton is localized on one of the sp^3 defects, and its wave function resembles the isolated defect site case (Figure 4-5c). The reorganization energy for a system with two sp^3 defects, separated by 3 nm, is 92 meV, approaching that of an isolated defect of 101 meV. The computed trend for λ suggests that observed reorganization energy (the difference between $\Delta E_{optical}$ and $\Delta E_{thermal}$) should depend on the defect density. This predicted trend, in fact, agrees with our experimental results.

4.3.5 Defect Detrapping Energy as a Function of the Density of Defects

As a route to a more in-depth understanding on the origins of this energy mismatch, we employ density functional theory to model the energies of the relevant states and transformations between them within a molecular picture of the defect site. We confirmed this theoretical prediction experimentally by measuring $\Delta E_{thermal}$ in (6,5)-SWCNT-$C_6H_4NO_2$ as a function of the defect density (Figure 4-6). The defect density is chemically controlled simply by changing the [Dz]:[C] reactant ratio and quantified by Raman spectroscopy (Figure 4-7). The Raman D/G ratio is directly correlated with the defect density because the D phonon mode (at ~1350 cm^{-1}) is due to symmetry breaking by the covalently attached aryl groups while the G band (~1580 cm^{-1}) is an in-plane stretching mode of the sp^2 bonded carbon lattice.[32] As SWCNTs react with increasing amounts of 4-nitrobenzenediazonium salts, the D/G ratio proportionally increases, consistent with previously reported trends in the reaction of (6,5)-SWCNTs with 4-bromobenzenediazonium salts.[14] From the constructed van 't Hoff plots, we found that the slopes ($\Delta E_{thermal}$) are linearly correlated with the defect density (Figure 4-8). The $\Delta E_{optical}$ is only weakly dependent on the defect density, with a change of only 5 meV across the range of densities explored. In contrast, $\Delta E_{thermal}$ is strongly affected by the density of defects, varying from 76 meV at the lowest density (synthesized at [Dz]:[C]=1:2500) to 134 meV at the highest (synthesized at [Dz]:[C]=1:250). At the lowest defect density that can be experimentally measured in (6,5)-SWCNT-$C_6H_4NO_2$, the mismatch (λ) between $\Delta E_{thermal}$ and $\Delta E_{optical}$ is as large as 98 meV, in close agreement with the DFT results for the isolated defect case (see Table 4-2). Similar results were obtained with a defect density series based on the 3,5-

dichloroaryl defects as well, for which a λ value of 120 meV was determined in the low defect density limit, again in agreement with the DFT results. We also note that the oxygen dopant result of Figure 4-2h was obtained in this low defect density limit, thus providing an explanation for the difference in our result for $\Delta E_{thermal}$ (24 meV) compared to that initially reported in the work of Ghosh *et al* (61 meV).[71]

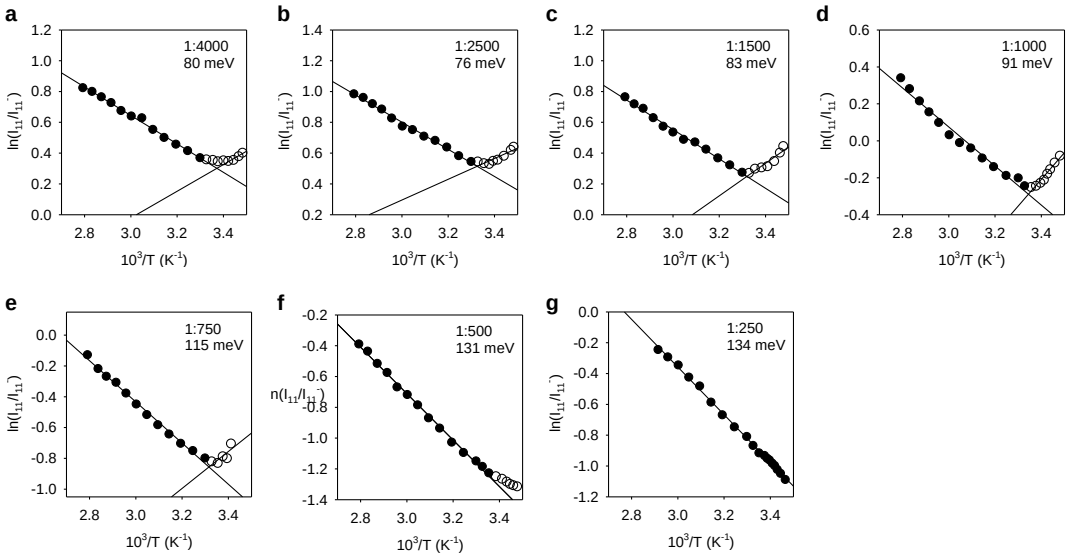

Figure 4-6 van 't Hoff plots of (6,5)-SWCNT-$C_6H_4NO_2$ at increasing defect density due to the increased [Dz]/[C] reactant ratios as labeled on each plot. The noted energy is derived from the slope of the fitted line through the black dots.

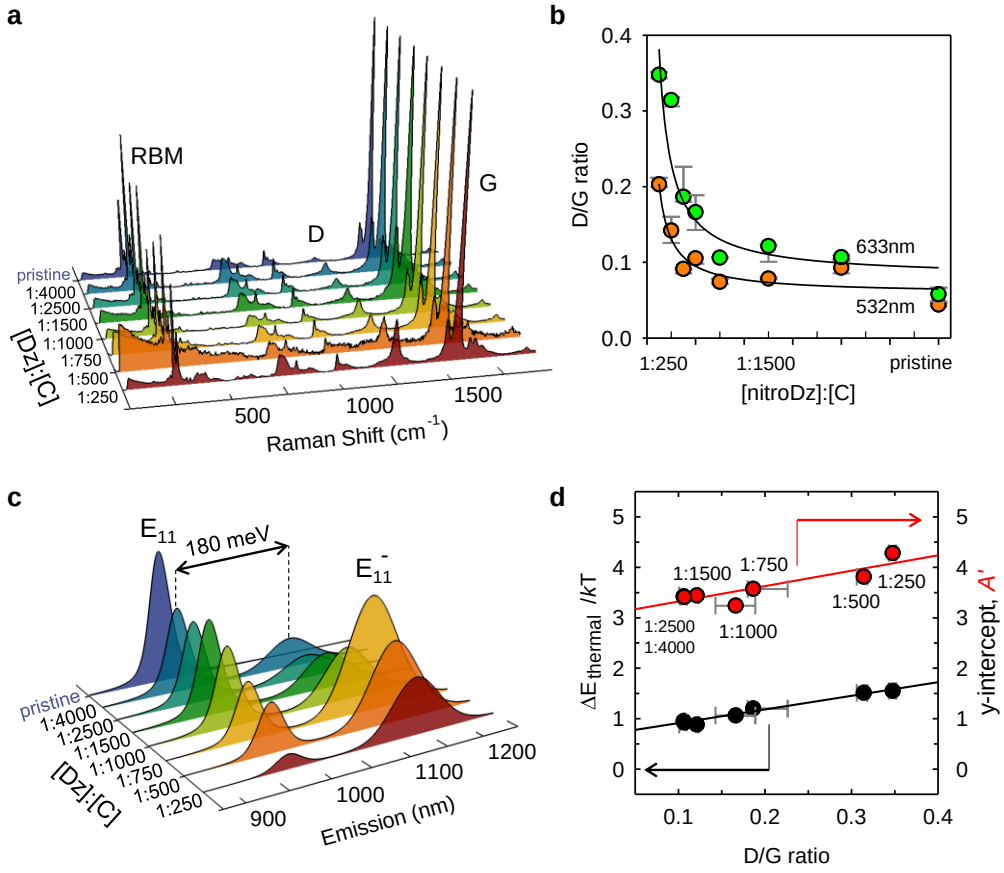

Figure 4-7 Correlated PL and Raman scattering of (6,5)-SWCNT-$C_6H_4NO_2$ with increasing density of fluorescent quantum defects. **a**, Raman spectra of non-functionalized (blue) and covalently modified SWCNTs by reacting at increasing [Dz]/[C] reactant ratios. The spectra were collected under 633 nm excitation and the intensities are normalized by the G-band. **b,** The Raman D peak intensity increases as a function of the [Dz]/[C] reactant ratio. Both 633 nm excitation (green dots) and 532 nm excitation (orange dots) show a similar trend. **c**, PL spectra of non-functionalized (blue) and (6,5)-SWCNT-C6H4NO2 at increasing [Dz]/[C] reactant ratios. (d) The van ‘t Hoff plot characteristics (slope and intercept) as a function of Raman D/G ratio at 633 nm excitation.

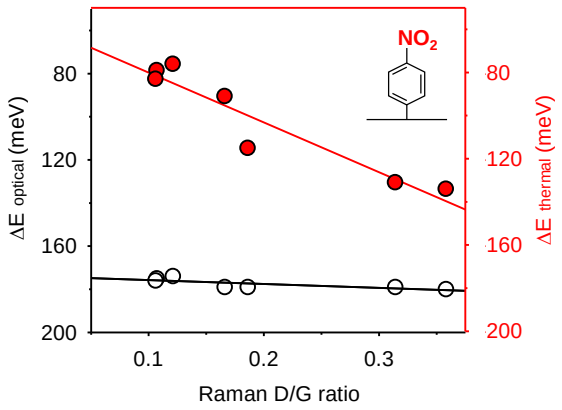

Figure 4-8 Correlations of optical gaps ($\Delta E_{optical}$, black open circles) and thermal detrapping energies ($\Delta E_{thermal}$, red closed circles) as functions of the density of 4-nitroaryl defects in (6,5)-SWCNTs. Both the emission energy difference ($\Delta E_{optical}$, from PL at room temperature) and the potential well depth ($\Delta E_{thermal}$, from thermodynamic probing experiments) are linearly correlated with the Raman D/G ratio.

At high defect densities, there is a finite probability that a single trapped exciton can be delocalized over two (or more) defect sites. This probability is small if the position of defects is completely random along the SWCNT. However, the probability can increase if the functional groups do effectively interact with each other; for instance, during a propagative reaction, a second functional group has a high probability to attach to a SWCNT near the first defect.[41] Evidence of defect coupling is suggested by the gradual, nevertheless persistent redshift (by 5 meV in Figure 4-8) and peak broadening (from 44.7 meV to 73.2 ± 7.9 meV at 30°C) of the E_{11}^{-} PL at increasing defect densities.

As indicated by our DFT results, there are two consequences of a trapped exciton being delocalized over two defect sites. First, at fixed ground state geometry its electronic energy decreases due to the delocalization of the trapped exciton. As a

result, the corresponding X^- parabola in Figure 4-4 would shift downward in energy by an amount Δ. Second, due to the decrease of the electron-phonon interaction upon the delocalization, the minimum of the resulting parabola shifts towards r = 0. The resulting potential energy surface is shown by a red dashed parabola in Figure 4-4. The corresponding reorganization energy, $\lambda' = E_{d'a}$ is smaller than the original λ. These two results have consequences for the observed behavior of both E_{11}^- and $\Delta E_{thermal}$.

For a trapped exciton that is delocalized over two (or more) defect sites, E_{11}^- and $\Delta E_{thermal}$ energies become

$$E_{11}^{-\prime} = E_{c\prime d\prime} = E_{11}^- - \Delta + (\lambda - \lambda') \qquad \text{Eqn. 4-7}$$

$$\Delta E'_{thermal} = E_{bc\prime} = \Delta E_{thermal} + \Delta \qquad \text{Eqn. 4-8}$$

and E_{11} remains the same if the concentration of defects is not large enough to significantly alter the ground and excited states of the entire SWCNT (this is observed experimentally). Eqn. 4-7 shows that the trap state emission energy, while red-shifted by the coupling between interacting sites, may be offset in the opposite direction by the reorganizational change accompanying the expected exciton delocalization at higher dopant densities. Our experimental observation of only minor changes in E_{11}^- as defect density is increased indicates these two effects nearly balance each other. As seen in Eqn. 4-8 on the other hand, $\Delta E_{thermal}$ is affected only by changes in Δ. Thus, the detrapping energy extracted from the van 't Hoff plots is expected to steadily increase with the defect density.

4.4 Conclusions

We observed a substantial mismatch between optical energy gap and detrapping energy in a series of fluorescent aryl defects in SWCNTs. Both the optical gap and the detrapping energy reveal a linear correlation with the electron withdrawing/donating capability of the aryl substituents. However, depending on the chemical nature and density of the defect, the detrapping energy is 14–77% smaller than the optical gap.

The observed energy mismatches can be understood in terms of vibrational reorganization due to significant deformation of the nanotube geometry upon exciton trapping at the defect site. The reorganization energy is experimentally determined to be as large as 100 meV for (6,5)-SWCNT-$C_6H_4NO_2$ and 120 meV for (6,5)-SWCNT-$C_6H_3(NO_2)_2$, and is strongly dependent on the defect density. These experimental findings are analyzed with our electronic structure simulations, which map the observed trends into defect-dependent vibrational reorganization energy in the molecular picture. Our findings are consistent with spectroelectrochemical measurements from oxygen-doped SWCNTs that show smaller redox potential than the optical energy gap[68] and provide new insights on the origin of the large discrepancy between the optical gap and the detrapping energy in fluorescent quantum defects. These insights establish a comprehensive picture of the energetics of fluorescent defects in SWCNTs, of direct relevance for the mechanistics of recently reported photon upconversion processes in defect-tailored SWCNTs,[72] and may help guide their design and synthesis of molecularly tunable quantum defects[15] for applications in near-infrared bioimaging, sensing,[45] energy harvesting,[72] and single photon sources.[48-49,94-95]

5 Generation of ultra-bright trions at fluorescent quantum defects

Adapted from a manuscript by Kwon, H.[†]; Kim, M. [†]; Hartmann, N. F.; Meany, B.; Clark, C.; Doorn, S. K.; Höegele, A.; Wang, Y.

[†] These authors equally contributed to this work.
Y.W., H.K., and M.K. conceived and designed the experiments. M.K. and H.K., performed the synthesis and spectroscopic experiments. N.F.H. performed lifetime measurements. B.M. performed nanotube sorting. Y.W., M.K. and H.K. wrote the manuscript with inputs from all co-authors.

5.1 Introduction

A negative trion is an electron-hole-electron (e-h-e) tri-carrier quasiparticle similar to the anions of hydrogen and positronium.[96] In contrast to electron-hole pairs that are known as excitons, a trion features a net charge and half-integer spin, which allow for the manipulation of electron spin[97] and optically probing local electrostatic fluctuations.[98] Governed by optical selection rules different from those of excitons,[99] trions can also significantly impact the dynamics of optically forbidden dark excitons.[100] Because of their unique properties, trions have been intensively explored for a broad range of potential applications, including quantum information,[97] sensing,[98] energy harvesting,[99] lasing,[101] and light-emitting devices.[102]

However, trions have been observed only as a minority species at room temperature. In fact, although this quasiparticle was theoretically predicted by Lampert[103] as early as 1958, trions escaped experimental observation for decades until their recent identification by photoluminescence (PL) spectroscopy in low dimensional semiconductors at cryogenic temperatures.[98,100-101,104] One of the key factors that

fundamentally limits trions to rise as a dominant species is their low binding energy (2 – 45 meV).[100,104] In low-dimensional semiconductors, such as single-walled carbon nanotubes (SWCNTs) and atomically thin 2D transition metal dichalcogenides, the binding energy of trions increases due to the stronger Coulomb interactions at reduced dimensionality, allowing trions to be detected at room temperature.[102,105] In SWCNTs, trions have been generated by high power laser excitation[106-107] and doping[108-111] of the host material, or by chemically charging covalently functionalized SWCNTs.[69] However, in all previous reports, including the one from us,[69] trion PL was typically rather weak and in the case of SWCNTs, weaker than the PL of native excitonsature. As it will become clear through this study, the challenges there are due, in part, to (1) the chemistry used[69] that does not allow for trions to be probed and tuned *in situ*, (2) lack of high purity nanotube semiconductor hosts, and (3) lack of tools that allow for directly imaging and probing of trions at the single molecule level.

Here we report the first direct experimental evidence of ultra-bright trions, enabled by trapping at chemical defects that are synthetically created in semiconducting SWCNT hosts through the incorporation of sp^3 alkyl defects into the sp^2 carbon lattice using a highly tunable trion chemistry. These chemical defects are quantum organic color centers,[14-15,48-49] allowing excitons to be channeled and radiatively recombined emitting nearly 100% pure single photons. By co-localizing a charge with the exciton at these organic color centers we now show that it is even possible to produce bright trions at these chemically tailored light emitting centers. Through single molecule fluorescence imaging, we experimentally resolved strong localization of trions around defects along the nanotube host. The trap-localized trions fluoresce brightly at room

temperature, even with weak excitation (< 1 kW/cm^2), which is otherwise impossible in the absence of strong localization due to trapping. We experimentally determined the binding energy of the defect-localized trions to be as large as 119 meV in (6,5)-SWCNT, which are significantly larger than that of mobile trions in the same host (54 meV),[109,111] 0D quantum dots (2–25 meV),[100,104] and also 2D materials (15–45 meV),[112] and can even be compared to the 327 meV binding energy of positronium anions.[96] The trapped trions have an emitting probability that is significantly larger than that of the native exciton, by a surprising 8-times, as well as a photoluminescence lifetime that is more than two-order of magnitude larger than "free" trions in the same host material. Our defect dependence studies and magnetoluminescence spectroscopy provide the first experimental evidence that unlike native excitons and free trions, these trapped trions are intrinsically bright (their lowest energy state is optically allowed).

5.2 Experimental Section

5.2.1 High Purity SWCNT Hosts.

CoMoCAT SG65i (Southwest Nanotechnologies, lot no. SG65i-L39) were stabilized in water as individual particles wrapped with DNA ($TTA(TAT)_2ATT$, Integrated DNA Technologies) using tip-sonication (Misonix, model S-4000) at 8 W and 10 ^oC for 2 h. Chirality pure (6,5)-SWCNTs were then isolated by polymer aqueous two-phase separation.[29] Long (6,5)-SWCNTs were isolated from raw SG65i using the superacid-surfactant exchange.[27] Other chirality-enriched SWCNT solutions were isolated from HiPco materials (Rice University, batch no. 194.3) by gel chromatography[28] using Sephacryl^{TM} S-200 high-resolution chromatography resin (GE Healthcare). The sorted SWCNTs were stabilized in D_2O (Cambridge Isotope Laboratories, Inc., 99.8%) with 1% wt/v sodium dodecyl sulfate (Sigma Aldrich, > 98.5%) for subsequent functionalization. The concentration of the chirality-enriched solutions was determined from absorption spectra based on the extinction coefficient of (6,5)-SWCNTs.[113]

5.2.2 Chemical Creation of Quantum Defects in SWCNT Hosts.

7.6 mM of $NaHCO_3$ (EMD chemicals, HPLC grade), 0.16% v/v CH_3CN (Acros organics, HPLC grade, 99.9%) and various alkyl halides (see Table 5-1) were added sequentially to each SWCNT solution, which was kept in a capped glass vial covered by aluminum foil to block out light. 3.6 mM of $Na_2S_2O_4$ (Sigma Aldrich, 85%) was then added to the mixture and stirred with a magnetic stir bar at room temperature. After 2 h of reaction, the SWCNT solution was characterized in situ by PL spectroscopy

at 565 nm excitation or excitation-emission mapping. To increase the density of defects, the concentration of the alkyl halide was increased proportionally to the concentration of the SWCNTs.

Table 5-1 Alkyl halide precursors used for the synthetic creation of quantum defects in SWCNT hosts.

Chemical	Manufacturer	Purity	Batch No.
$I(CF_2)_5CF_3$	Sigma Aldrich	99 %	MKBJ8925V
$I(CH_2)_2(CF_2)_3CF_3$	Fluka Analytical	95 %	BCBH7887V
$I(CH_2)_2CF_2CF_3$	TCI	98 %	-
$I(CH_2)_4CF_2CF_3$	Matrix Scientific	97 %	V05H
$I(CH_2)_2CF_3$	Sigma Aldrich	97 %	MKBF3292V
$I(CH_2)_3CF_3$	Santa Cruz Biotechnology	99 %	C3114
$I(CH_2)_5CF_3$	Oakwood Chemical	97 %	F17N
$I(CH_2)_5CH_3$	Sigma Aldrich	98 %	MKBW2847V

5.2.3 Spectroscopic Characterization of Trion PL

The reactions were monitored in situ using a NanoLog spectrofluorometer (HORIBA Jobin Yvon). The samples were excited with a 450 W Xenon source dispersed by a double-grating monochromator. The slit width of the excitation and emission beams was 10 nm. Excitation-emission maps and single excitation PL spectra were collected using a liquid-N_2 cooled linear InGaAs array detector. Absorption spectra were also measured, using a Lambda 1050 UV-vis-NIR spectrophotometer (Perkin Elmer) equipped with both a photomultiplier tube and an extended InGaAs detector. For single tube PL imaging, a small aliquot of (6,5)-SWCNT-C_6H_{13} solution in 1 % wt/v sodium deoxycholate (Sigma Aldrich, >99%) was deposited on poly D-lysine coated glass slides (Part No. P35GC-0-10-C, MatTek Corporation). The imaging

was performed using a custom-built system that integrates an inverted microscope (Eclipse Ti-U, Nikon), a volume Bragg grating system (Photon etc), and an oil immersion objective (UAPON 150XOTIRF, NA = 1.45, Olympus). The nanotubes were excited by a 730 nm diode laser at a power density of 0.5 kW/cm^2, and the PL emission was collected using a liquid-N_2 cooled 2D InGaAs detector (Cougar 640, Xenics) with an integration time of 16 s.

5.2.4 Brightness of Trion PL on the Ensemble Level

The relative PL brightness of E_T and E_{11}^- was calculated using the following equations:

$$\Phi_T = \frac{I_T}{I_0}\frac{OD_{565nm}}{OD^*_{565nm}} \qquad \text{Eqn. 5-1}$$

$$\Phi_{11}^- = \frac{I_{11}^-}{I_0}\frac{OD_{565nm}}{OD^*_{565nm}} \qquad \text{Eqn. 5-2}$$

in which Φ is the relative PL brightness, I_T and I_{11}^- are the integrated PL intensities of E_T and E_{11}^- of the functionalized SWCNTs, respectively, I_0 is the integrated PL intensity of the unfunctionalized SWCNTs, OD^*_{565nm} is the optical density of the functionalized (6,5)-SWCNTs at the E_{22} excitation, and OD_{565nm} is the optical density of the unfunctionalized (6,5)-SWCNTs at the E_{22} excitation. The PL peaks were fitted with Voigt functions using PeakFit software v4.12. No baseline correction was applied.

5.2.5 The Probability for a Trapped Trion to Radiatively Decay

The number of E_{11} photons (N_{11}) is proportional to the PL quantum yield of E_{11} exciton (η_{11}) and the number of absorbed photons to a SWCNT (N_{abs}):

$$N_{11} = N_{abs}\eta_{11} \qquad \text{Eqn. 5-3}$$

Considering the diffusion and trapping of E_{11} excitons at defect states[36-37], here E_{11}^- (or E_T), the number of photons emitted from the E_{11}^- (or E_T) state, N_{11}^- (or N_T) is:

$$N_{11}^- = N_{abs}\frac{k_{dif}}{k_r+k_i+k_{dif}}\frac{n_{11}^-}{n_q+n_{11}^-+n_T}\eta_{11}^- \qquad \text{Eqn. 5-4}$$

$$N_T = N_{abs}\frac{k_{dif}}{k_r+k_i+k_{dif}}\frac{n_T}{n_q+n_{11}^-+n_T}\eta_T \qquad \text{Eqn. 5-5}$$

in which k_r is the radiative decay rate for E_{11} excitons, k_{dif} is the decay rate of the E_{11} excitons due to exciton diffusion and trapping at defect sites (quenching defects, E_{11}^- and E_T defect sites), and k_i is the effective decay rate for all possible non-radiative recombination other than exciton trapping and the radiative decay before trapping. n_q is the number of the quenching defects, and n_{11}^- and n_T are the numbers of neutral and charged quantum defect sites on a SWCNT, respectively. η_{11}^- and η_T are the probabilities for a trapped exciton and trion, respectively, to radiatively decay and emit a photon.

Note that in this kinetic model we assume once trapped an exciton cannot escape the defect site (indeed, thermal detrapping has a relatively low efficiency as previously demonstrated for E_{11}^- excitons[60]). We also assume that the defect sites are evenly distributed along the nanotube; more rigorous treatment may need to take into account the effect of spatial distribution of defects.[114]

The quantum yields of E_{11} excitons in unfunctionalized (η_0) and quantum defect-tailored SWCNTs (η_{11}) are given by:

$$\eta_0 = \frac{\pi k_r}{2D(n_q)^2 l^{-2}} \qquad \text{Eqn. 5-6}$$

$$\eta_{11} = \frac{\pi k_r}{2D\left(n_q+n_{11}^-+n_T\right)^2 l^{-2}} \qquad \text{Eqn. 5-7}$$

in which l is the average nanotube length and D is the exciton diffusion constant.

From Eqns. 5-1, 5-6, and 5-7, the changes in the number of E_{11} photons by covalent functionalization, ΔN_{11} can be calculated as:

$$\Delta N_{11} = N_{abs}\eta_0\left(1-\frac{\eta_{11}}{\eta_0}\right) = N_{abs}\eta_0\left[1-\frac{{n_q}^2}{\left(n_q+n_{11}^-+n_T\right)^2}\right]$$

$$= N_{abs}\eta_0\left[1+\frac{n_q}{n_q+n_{11}^-+n_T}\right]\left[1-\frac{n_q}{n_q+n_{11}^-+n_T}\right] \qquad \text{Eqn. 5-8}$$

Using Eqns. 5-4 and 5-8, we obtained

$$\frac{N_{11}^-}{\Delta N_{11}} = \frac{\eta_{11}^-}{\eta_0}\frac{k_{dif}}{k_r+k_i+k_{dif}}\frac{n_q+n_{11}^-+n_T}{2n_q+n_{11}^-+n_T}\left(1+\frac{n_T}{n_{11}^-}\right)^{-1} \qquad \text{Eqn. 5-9}$$

At the low defect density limit ($n_q \gg n_{11}^- + n_T$), $\frac{n_q+n_{11}^-+n_T}{2n_q+n_{11}^-+n_T} \sim \frac{1}{2}$. We further assume $k_r + k_i \ll k_{dif}$, as supported by previous studies on E_{11} exciton PL,[36,38] and therefore $\frac{k_{dif}}{k_r+k_i+k_{dif}} \sim 1$. The number of emitted photons (N) is proportional to the integrated PL intensity (I). So Eqn. 5-9 is simplified to

$$\frac{I_{11}^-}{\Delta I_{11}} = \frac{\eta_{11}^-}{2\eta_0}\left(1+\frac{n_T}{n_{11}^-}\right)^{-1} \qquad \text{Eqn. 5-10}$$

Similarly, from Eqns. 5-5 and 5-8, we obtained Eqn. 5-11 (an equivalent form cited as Eqn. 5-17 in Section 5.3.2)

$$\frac{I_T}{\Delta I_{11}} = \frac{\eta_T}{2\eta_0}\left(1+\frac{n_{11}^-}{n_T}\right)^{-1} \qquad \text{Eqn. 5-11}$$

From single nanotube PL imaging experiments, we confirmed that $n_{11}^- > n_T$ and $n_T \geq 0$ for our experimental conditions, and obtained η_{11}^- and η_T for $\frac{\Delta I_{11}}{I_0} = 0.22$ as follows (see also Table 5-2)

$$16.35\eta_0 < \eta_{11}^- < 32.7\eta_0 \qquad \text{Eqn. 5-12}$$

$$7.88\eta_0 \leq \eta_T \qquad \text{Eqn. 5-13}$$

Table 5-2 Lower-bound probability for a trapped trion in (6,5)-SWCNT-C_6H_{13} to radiatively recombine and emit a photon. The probabilities were calculated using Eqns. 5-10 and 5-11 where η_0 is determined from lifetime measurement to be 1%.

$[C_6H_{13}I]/[C]$	$\Delta I_{11}/I_0$	η_{11}^- (%)	Minimum η_T (%)
3	0.22	16 – 33	7.88
4	0.31	15 – 30	7.63
6	0.42	15 – 24	6.29
8	0.45	14 – 28	7.62

5.2.6 Brightening Effects by E_{11} Excitation

$N_{abs,\lambda}$, the number of excitons generated upon excitation at λ, is related to the molar extinction coefficient of SWCNTs at a given wavelength ($\sigma_{\lambda nm}$) and the E_{22} to E_{11} branching ratio (γ). Specifically, the number of E_{11} excitons by E_{11} and E_{22} excitations can be expressed as:

$$N_{abs}(E_{11}) = b\sigma_{980nm} \qquad \text{Eqn. 5-14}$$

$$N_{abs}(E_{22}) = \gamma b\sigma_{565nm} \qquad \text{Eqn. 5-15}$$

respectively. Here *b* is a correction factor to account for the nonradiative recombination of E_{11} excitons. Using Eqns. 5-14 and 5-15, the collective PL intensity $I_{total} \propto N_{11} + N_{11}^- + N_T$ at different excitation wavelengths can be compared. This brightening factor by excitation at E_{11} (versus E_{22}) can then be expressed as:

$$\frac{I_{total}(E_{11})}{I_{total}(E_{22})} = \frac{1}{\gamma}\frac{OD_{980nm}}{OD_{565nm}} \qquad \text{Eqn. 5-16}$$

in which I_{total} is the integrated PL intensity, and OD is the optical density at the excitation wavelength.

Experimentally, we used a 450 W Xenon arc source dispersed by a double monochromator system within the Nanolog spectrometer to excite the (6,5)-SWCNTs at E_{22} and E_{11}, with a slit width of 3 nm. The photon fluence at each wavelength was measured using an optical power meter (Newport 1916-C) equipped with a silicon detector (Newport 918-SL-OD3). The PL intensity was corrected based on the excitation fluence. To simultaneously excite SWCNTs at E_{11} and detect the E_{11} PL, a 980 nm notch filter with a full width at half maximum (FWHM) of 41 nm (Thorlabs, NF980-41) was placed between the sample and detector. The spectral resolution for the emission detection channel was 1 nm. The E_{11} peak was reconstructed based on the lower energy trace of the E_{11} PL. To avoid potential errors in peak fitting, ultrapure (6,5)-SWCNT samples were used for the experiments.

5.2.7 Hole Doping Experiments

The (6,5)-SWCNT-C_6H_{13} solutions were ultrafiltrated using a 100 kDa ultrafiltration centrifugal tube (Amicon, EMD Millipore) to remove the reaction byproducts and unreacted reagents. The quantum defect-tailored SWCNTs were then hole-doped by hydrochloric acid. The solution pH was adjusted from 2.98 to 8.72 by adding small aliquots of 20 mM HCl (Sigma Aldrich) or $NaHCO_3$ solutions. The pH was determined using a pH meter (AccumetTM AB15+ Basic and BioBasic pH meters, Fisher Scientific). Hole doping by 2,3,5,6-tetrafluoro-7,7,8,8,-tetracyanoquinodimethane (F_4TCNQ) was performed by sequentially increasing the concentration of F_4TCNQ (Sigma Aldrich, 97 %, lot no. MKBR1477V) from 0 to 1 mM in the SWCNT solution.

5.2.8 PL Lifetime Measurement through Time-Correlated Single Photon Counting

The surfactant environment of the (6,5)-SWCNT-C_6H_{13} sample was exchanged with 1% wt/v sodium deoxycholate by ultrafiltration (Amicon, no. 5123, using 100 kDa ultracel regenerated cellulose filter membranes). 100 μl of the SWCNT solutions were transferred into NMR tubes for the measurements. The PL lifetimes were measured using 568 nm excitation (4 ps pulsewidth, 40 MHz repetition rate) and a single quantum nanowire detector. Spectral filtering to resolve each PL peak was achieved with appropriate band-pass (BP)/long-pass (LP) filters in front of the detector, including BP 1000/50 for E_{11}, BP 1100/10 for E_{11}^-, and LP1200 for E_T. The collected decay curves were reconvolution fitted with the corresponding instrument response function for each detector in FluoFit (Picoquant).

5.2.9 Magnetoluminescence Measurements

The unfunctionalized (6,5)-SWCNT control and (6,5)-SWCNT-C_6H_{13} in 1 % wt/v DOC were drop-casted onto SiO_2 substrates and subjected to magnetic fields of up to 8 T in a home-built confocal microscope immersed in a helium bath cryostat with a base temperature of 4.2 K. Individual nanotubes were selected for collinear orientation with the magnetic field axis using the well-known antenna effect.

5.3 Results and Discussions

5.3.1 Spatial Localization of Trions at Quantum Defect Sites

We chemically created quantum defects in individual (6,5)-SWCNTs by covalently attaching hexyl groups to the semiconducting SWCNTs,[15] producing a 0D-1D hybrid quantum system hereafter labeled as (6,5)-SWCNT-C_6H_{13} (Figure 5-1a). The defect creates a discrete state (E_{11}^-, emitting at 1095 nm) that lies below the native E_{11} excitonic state of the nanotube (emitting at 980 nm; Figure 5-1b). $Na_2S_2O_4$, which is used as a radical initiator, also acts as a reducing agent that introduces electrons to the nanotube enabling production of negatively charged trions (E_T, emitting at 1226 nm). In stark contrast to free trions in unfunctionalized SWCNTs that are mobile or weakly bound at shallow potential wells,[106,111] in the presence of quantum defects, we found that trions are localized in a deep potential well, with a depth of ΔE_T (the energy difference between E_{11} and E_T in the PL spectra; Figure 5-1a). By controlling the density of defects, we show it is possible to finely tune the defect and trion PL intensities (Figure 5-2). We found that the E_{11} emission decreased over the course of the reaction while the intensity of E_{11}^- and E_T PL peaked after around 30 min of reaction and stabilized within 1 h. This correlated PL evolution pattern of E_{11}^- and E_T indicates that trion formation is directly related to the fluorescent quantum defects.

Single defect-resolved hyperspectral PL imaging provides direct evidence that trions are spatially localized at the quantum defects (Figure 5-1c-f). Note that this observation is made at low excitation power (0.5 kW/cm^2 at off-reasonant wavelength, 730 nm) to avoid possible optical generation of trions.[106] While E_{11} PL is distributed

along the whole length of the imaged nanotube (7 μm), the E_{11}^- and trion PL are spatially confined within the diffraction limit of our PL microscope (430 nm). The PL emission of E_T is also spatially correlated to the intensity profile of E_{11}^-, which similarly shows localization as previously observed for ether and aryl defects,[62] and low PL intensity of E_{11}. This complementary nature of intensity distribution suggests that trion PL originates from the hexyl defects and spatially correlates with E_{11}^- states.

In the absence of the hexyl defects, $Na_2S_2O_4$ does not induce E_T. Hole doping experiments further confirm that the observed E_T PL originates from negative trions in (6,5)-SWCNT-C_6H_{13}. Our results showed that the PL intensity of all three peaks (E_{11}, E_{11}^-, and E_T) decreased upon addition of hydrochloric acid as a hole dopant, due to the known quenching effect of hole-doping for E_{11} excitons,[115] but the E_T peak responded even more sensitively to the doping compared to E_{11}^- (Figure 5-3d, e). When the proton concentration is higher than 1 mM, the trion PL becomes completely quenched. This doping effect is also consistently observed for another hole doping agent, 2,3,5,6-tetrafluoro-7,7,8,8,-tetracyanoquinodimethane (Figure 5-3b,c). This doping effect is attributed to the hole dopants that can readily neutralize the negatively charged trions.

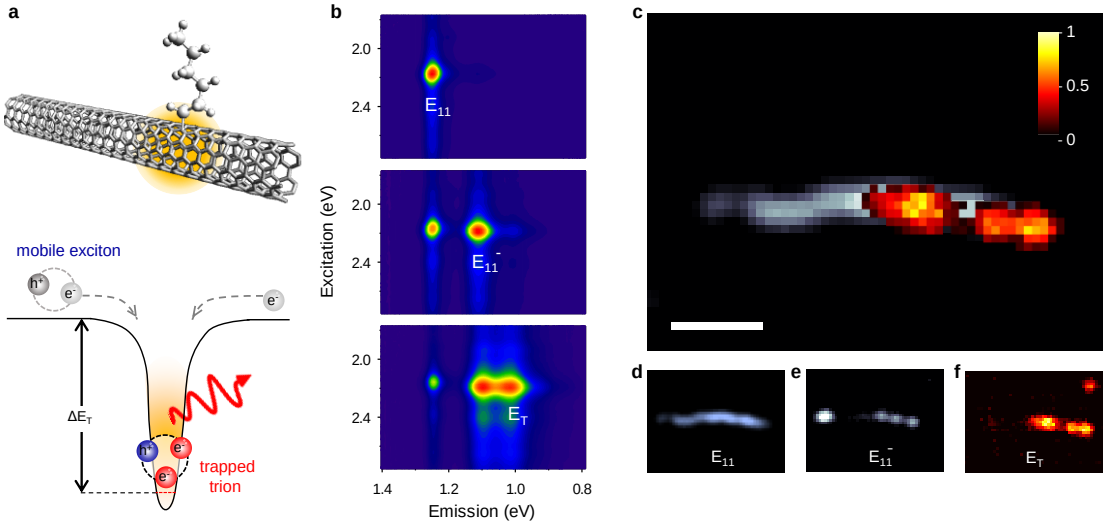

Figure 5-1 Spatial localization of trions at fluorescent quantum defects. **a,** Schematic of a trion trapped in a defect-induced quantum well with a depth of ΔE_T. **b,** Excitation-emission PL maps showing the rise of bright trions as (6,5)-SWCNT (top) is chemically tailored with alkyl quantum defects (middle and bottom). **c,** Localized trion PL in a 4.4 μm long (6,5)-SWCNT-C_6H_{13} resolved by hyperspectral imaging. Scale bar is 2 μm. The trion PL (red) is superimposed on the E_{11} PL (blue) of the nanotube host, with the PL intensity of E_T scaled by a factor of 4 for clarity. Hyperspectral PL images of **d,** E_{11} (992 nm), **e,** E_{11}^- (1108 nm), and **f,** E_T (1224 nm) emission, resolved using a volumetric Bragg grating with a spectral resolution of 4 nm.

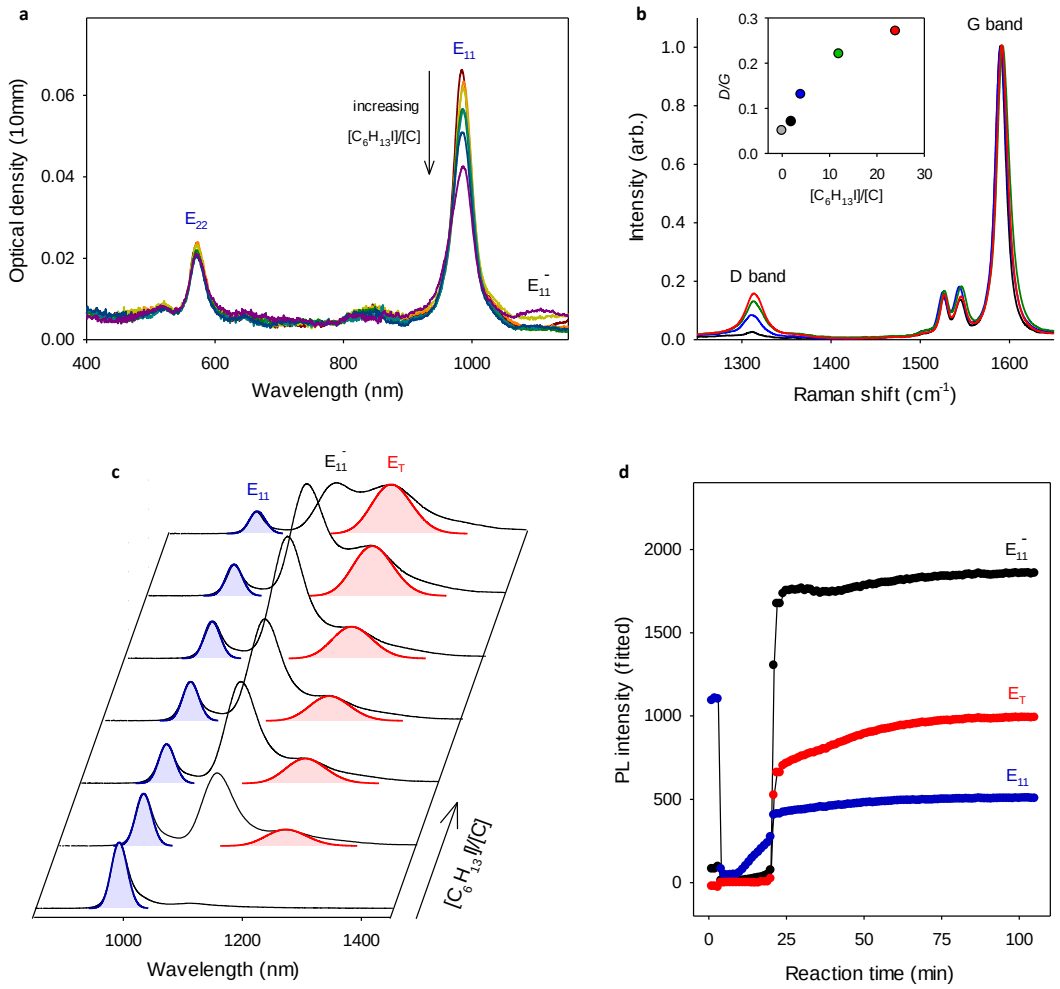

Figure 5-2 Creation of quantum defects by covalently attaching hexyl functional groups to the semiconductor host. **a,** UV-vis-NIR absorption spectra of (6,5)-SWCNT-C_6H_{13} at increasing concentrations of the $C_6H_{13}I$ reactant. At the highest reactant molar ratio of $[C_6H_{13}I]/[C]$ = 16 (purple trace), the defect-induced E_{11}^- state can be identified as an absorption band centered at 1100 nm. **b,** Raman spectra of unfunctionalized (6,5)-SWCNTs (black) and (6,5)-SWCNT-C_6H_{13}. The inset is the integrated intensity ratio of Raman D band (1200–1400 cm^{-1}) to G band (1500–1650 cm^{-1}) as a function of the molar ratio of reactants. The excitation wavelength is 633 nm. **c,** The PL spectra, from bottom to top, are of (6,5)-SWCNT-C_6H_{13} for $[C_6H_{13}I]/[C]$ molar ratios of 0 (unfunctionalized), 3, 4, 6, 8, 12, and 16, respectively. **d,** The PL evolution profiles of E_{11} (blue), E_{11}^- (black), and E_T (red) as a function of reaction time. The PL intensity is the integrated PL intensity of the Gaussian-fitted PL peaks.

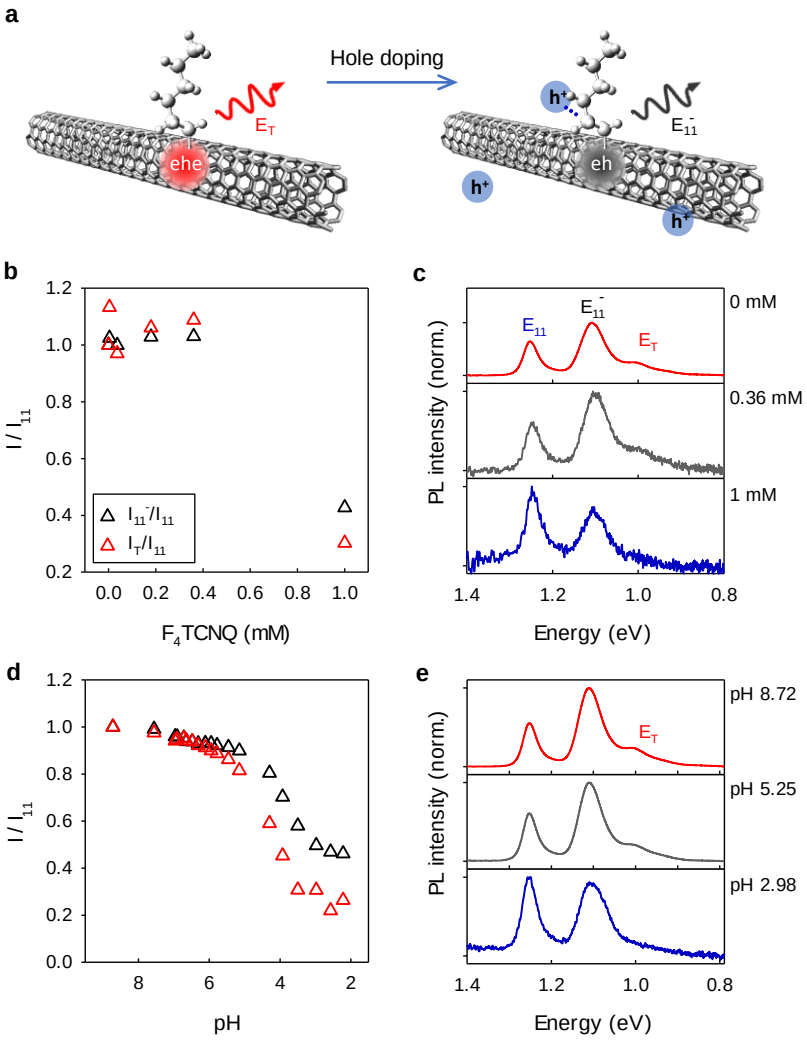

Figure 5-3 Hole doping of (6,5)-SWCNT-C_6H_{13} by F_4TCNQ and HCl. **a,** Schematic of hole doping in SWCNT-C_6H_{13}. The hole dopants neutralize the extra negative charge of the trion, resulting in reduced E_T PL intensity. **b,** The defect PL changes as a function of F_4TCNQ concentration. Note that the integrated intensity of trion PL (I_T/I_{11}) at a specific pH was normalized by the PL intensity (I_T/I_{11}) at the starting pH 8.72. **c,** Normalized PL spectra of (6,5)-SWCNT-C_6H_{13} hole-doped with 0 mM (red), 0.36 mM (gray), and 1 mM (blue) of F_4TCNQ. The trion PL is completely quenched at 1 mM of F_4TCNQ. **d,** The defect PL changes as a function of solution pH. **e,** Normalized PL spectra of pH 8.72 (red), 5.25 (grey), and 2.98 (blue). The trion PL completely quenched at pH 2.98.

5.3.2 Bright PL from Trapped Trions.

In stark contrast to free trions in unfunctionalized SWCNTs,[111] our alkyl-functionalized SWCNTs exhibit surprisingly bright PL. In the absence of intentionally implanted quantum defects, the PL brightness of trions is far below that of E_{11} and can only be resolved at high doping (> 0.7 nm^{-1}, ref [110]) or power densities (> 1 kW/cm^2, ref [106]). In our system, the observed trion PL intensity is 3.1-times the native E_{11} PL intensity of unfunctionalized SWCNTs, even though the quantum defect sites are outnumbered by the lattice atoms of SWCNTs by more than 100 times, and approximately 7.3-times as high as the brightest trion ever reported[69] based on ensemble measurements (Figure 5-4a). By exciting the nanotube at the E_{11} transition instead of the typical E_{22}, we further demonstrate that the trion PL intensity can be further increased, by another factor of 2.7, to a total of more than 8 times (Figure 5-5).

Consistently, PL lifetime measurements (Figure 5-4 and Table 5-3) show that the PL decay of E_{11} in (6,5)-SWCNT-C_6H_{13} is dominated by the bright state (τ ~24 ps) and a small, long-lived component (103 ps; amplitude less than 5%). These time scales are similar to those observed in unfunctionalized control samples (25 ps and 147 ps) where the long component originates from dark E_{11} excitons.[57] In the presence of quantum defects, the PL decays of E_{11}^- and E_T are also biexponential. However, the E_T PL lifetimes (154 ± 12 ps for τ_s and 374 ± 8 ps for τ_l) are considerably longer than the E_{11} PL and "free" trions (less than 2 ps).[110,116] The amplitude of τ_l for E_T was 53.7 ± 1.6%, which is also significantly higher than those of E_{11} and E_{11}^- (4.8 ± 0.3% and 18.6 ± 0.4%, respectively).

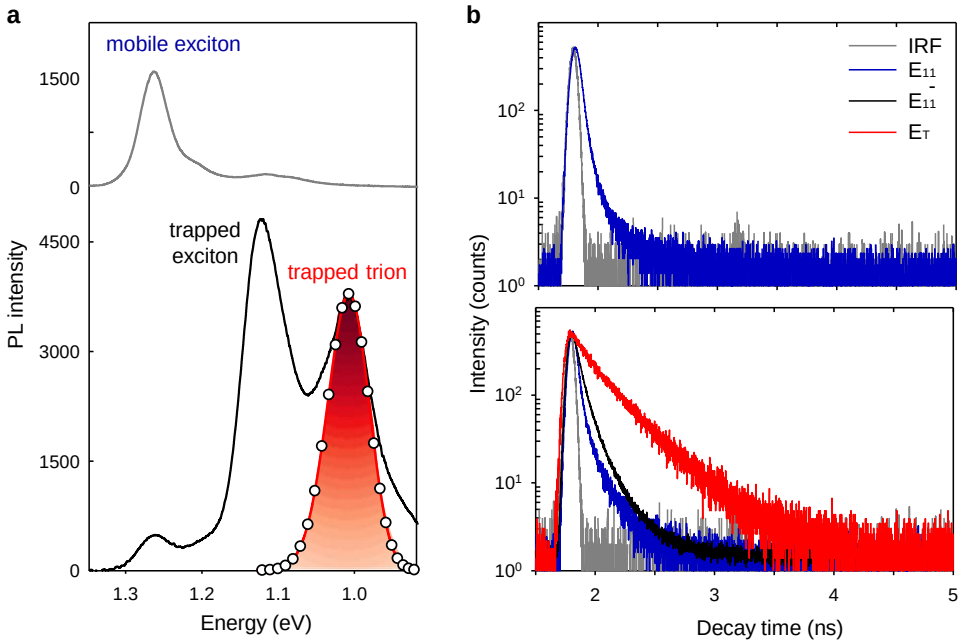

Figure 5-4 Ultra-bright PL from trapped trions. **a,** PL spectra of (top) unfunctionalized (6,5)-SWCNT, the semiconductor host, and (bottom) (6,5)-SWCNT-C_6H_{13}. The excitation wavelength is 565 nm. **b**, The PL decays of E_{11} from (top) (6,5)-SWCNT and (bottom) E_T, E_{11}, and E_{11}^- of (6,5)-SWCNT-C_6H_{13}. Note that the instrument response function (IRF) is also plotted.

Table 5-3 PL lifetime of (6,5)-SWCNT-C_6H_{13} in comparison with the unfunctionalized control.

PL peak	τ_s (ps)	A(τ_s) %	τ_s (ps)	A(τ_l) %
Unfunctionalized (6,5)-SWCNT				
E_{11}	24 ± 1	98.1 ± 1.9	103 ± 6	1.9 ± 0.2
Functionalized (6,5)-SWCNT-C_6H_{13}				
E_{11}	25 ± 1	95.2 ± 2.1	147 ± 5	4.8 ± 0.3
E_{11}^-	68 ± 1	81.4 ± 1.3	206 ± 3	18.6 ± 0.4
E_T	154 ± 12	46.3 ± 3.5	374 ± 8	53.7 ± 1.6

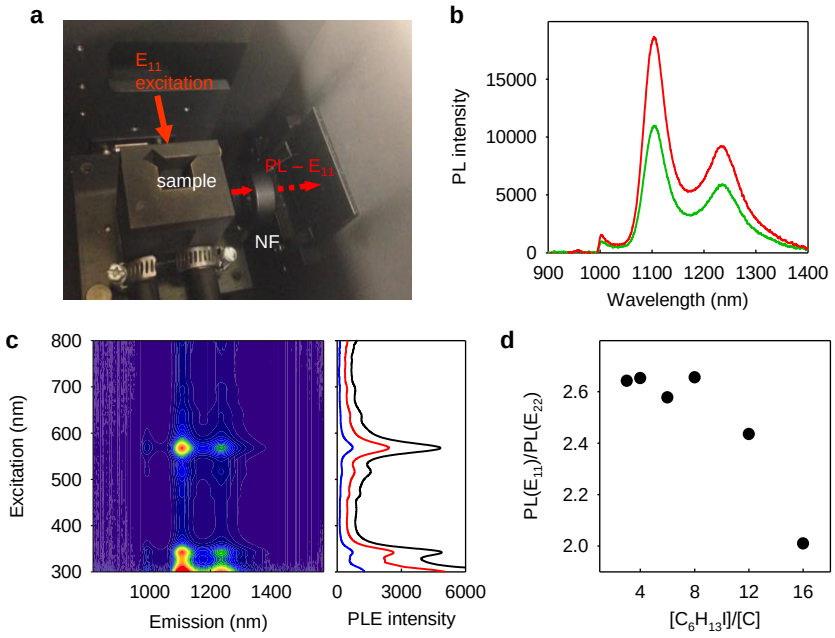

Figure 5-5 Brightening of SWCNT PL by E_{11} excitation. **a,** Experimental setup of E_{11} excitation experiments. A notch filter (NF), centered at 980 nm with 41 nm FWHM, was placed to reject E_{11} excitation light from detection. **b,** PL spectra of (6,5)-SWCNT-C_6H_{13}, measured with this experimental setup at E_{11} (975 nm, red) and E_{22} (565 nm, green) excitations. The 980 nm notch filter blocks the PL emission from 960–1000 nm. **c,** Excitation-emission PL map and PL excitation spectra of (6,5)-SWCNT-C_6H_{13}. All PL peaks, including E_{11} (blue), E_{11}^- (black), and E_T (red), resonate to the electronic transitions of (6,5)-SWCNTs. We note that the shapes for all three excitation spectra are identical. **d,** PL intensity ratio of E_{11} vs. E_{22} excitation as a function of the molar ratio of reactants, $[C_6H_{13}I]/[C]$.

Based on fluorescent lifetime measurements, the QY of the E_{11} exciton is estimated at 1%, consistent with reports for unfunctionalized SWCNTs in aqueous dispersion.[36] To determine the emitting probability of quantum defect-trapped trions, we considered exciton diffusion, trapping at local defects,[36-37,57] and the formation of trions at the defect site in the low defect density limit, and derived that

$$\frac{\eta_T}{\eta_0} = \frac{2I_T}{\Delta I_{11}}\left(1 + \frac{n_T}{n_{11}^-}\right) \qquad \text{Eqn. 5-17}$$

in which η_T and η_0 are the emitting probabilities of E_T and E_{11} excitons, respectively, I_T is the PL intensity of the trions, ΔI_{11} is the change in E_{11} PL intensity due to the incorporation of quantum defects, and n_T and n_{11}^- are the number of E_{11}^- and E_T defects on a SWCNT (see Section 5.2.5 for the derivation). Based on this calculation, we found that the PL QY of a trapped exciton in (6,5)-SWCNT-C_6H_{13} is approximately 16.4 – 32.7%, which is consistent with Piao *et al.*,[14] while a trapped trion has a lower-bound probability of at least 7.9% to emit a photon, nearly 8 times as bright as the E_{11} exciton in unfunctionalized SWCNTs.

Surprisingly, E_{11}^- and E_T are both brighter than the statistical upper-bound limit of bright E_{11} excitons in SWCNTs based on spin and symmetry selection rules alone.[117] These observations suggest that dark excitons must contribute to the observed ultra-bright PL from trapped excitons and trions. Furthermore, ΔE_T shows a strong dependence on both the nanotube chirality and diameter (Figure 5-6 and Table 5-4). The (2n + m) family pattern of ΔE_T matches that of free trions in unfunctionalized SWCNTs[108] while the diameter dependence follows the inverse second order equation, which is another evidence of dark exciton brightening.[14,21] It is important to note that our experiments do not reveal the detailed mechanisms by which the dark excitons may

contribute, but we suspect that dark exciton brightening occurs due to the trion's extra charge, which makes trions follow a different selection rule from that of excitons.

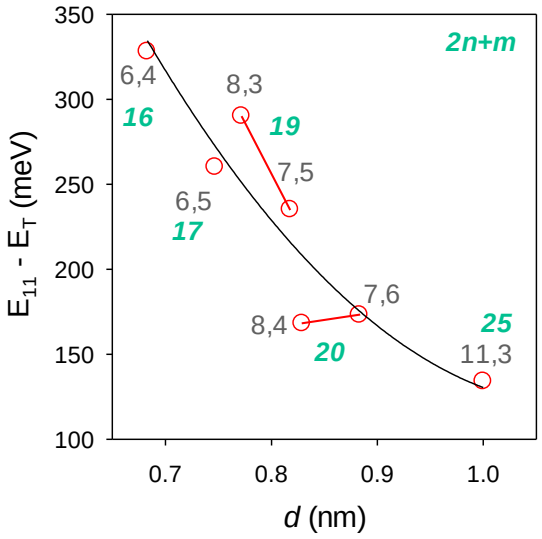

Figure 5-6 Diameter dependence of E_T in (n,m)-SWCNT-C_6H_{13}. Trion emission energy is correlated with SWCNT diameter (d) by $\Delta E_T = E_{11} - E_T = A/d + B/d^2 + C$. Deviations from the fitted line are related to the chiral angle dependence.

Table 5-4 Chirality dependence of trion PL. Each chirality was clearly resolved due to the use of high purity samples.

(n,m)	d (nm)	E_{11} (nm)	E_{11}^- (nm)	E_T (nm)	ΔE_{11}^- (meV)	ΔE_T (meV)
(6,4)	0.683	879	1044	1138	223	321
(6,5)	0.747	982	1102	1229	138	254
(8,3)	0.772	960	1126	1231	190	284
(7,5)	0.818	1027	1174	1270	151	231
(8,4)	0.829	1117	1228	1316	100	168
(7,6)	0.883	1128	1228	1332	90	168
(11,3)	1.000	1207	1326	1386	92	133

5.3.3 Magnetoluminescence Spectroscopy Suggests Absence of Dark States in the Energetic Vicinity of Trapped Trions

In order to probe the presence of potential dark states in the energetic vicinity of E_{11}^- and E_T states, we performed magnetoluminescence spectroscopy on individual SWCNTs. The upper and lower panels of Figure 5-7a show the evolution of the E_{11} peak for an unfunctionalized (6,5)-SWCNT in response to an increasing magnetic field. The nanotube PL exhibits both characteristic features expected for an unfunctionalized SWCNT subjected to a coaxial magnetic field[19]: with increasing magnetic field, the lower-lying singlet dark state brightens progressively by acquiring oscillator strength at the expense of the bright state (as evident from the peak fits of the bright and dark PL emissions in the upper panel as well as in the color-coded PL representation in the lower panel of Figure 5-7a); additionally, the bright-dark splitting of the singlet (Δ_0) evolves from its zero-field value of 4.5 meV according to the hyperbolic relation $\Delta^2 = \Delta_0^2 + \Delta_{AB}^2$ (solid line in the inset of the lower panel of Figure 5-7a).[118] The field-induced energy splitting $\Delta_{AB} = \mu\varphi$ is a consequence of the Aharonov-Bohm flux $\varphi=\pi d^2 B_{||}/4$ due to the fraction of the magnetic field $B_{||} = B \cos\theta$ that is parallel to the SWCNT with diameter (d) and magnetic coupling constant (μ). Based on the fit to the data with $\theta = 45°$ for this specific nanotube, we extracted $\mu = 1.8$ meVT^{-1} nm^{-2}, which is consistent with a (6,5) tube diameter of 0.76 nm and values found in previous experiments.[119]

In stark contrast to the E_{11} PL of the unfunctionalized SWCNT in Figure 5-7a, neither the E_{11}^- nor the E_T peaks of the covalently functionalized nanotube showed sizeable effects in magnetic fields of up to 8 T (upper and lower panels of Figure 5-7b

and c, respectively). Both E_{11}^- and E_T remained solitary peaks throughout the magnetic field sweep, without displaying any significant shifts or splitting within the energy boundaries given by characteristic spectral fluctuations (~2 meV) and the resolution limit of our spectrometer (~0.1 meV), respectively. These observations provide the first experimental evidence suggesting that E_{11}^- and E_T are the lowest energy states for these defect-trapped quasi-particles. This further explains why the trapped excitons and trions are much brighter than their "free" counterparts, whose photophysics is dominated by non-radiative decay mechanisms due to the lower-lying dark states, and thus may present a new quasi-particle state that is intrinsically bright.

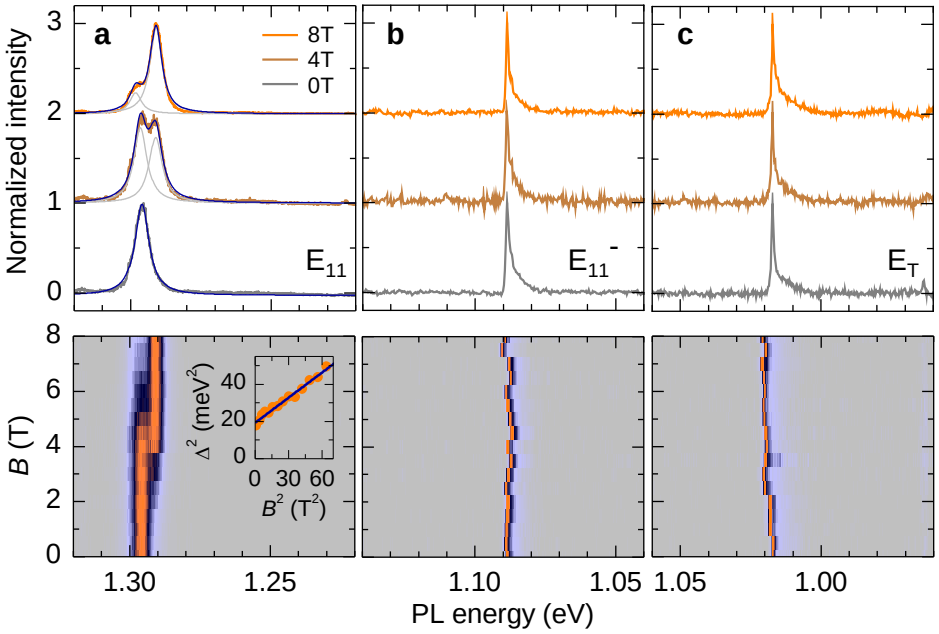

Figure 5-7 Spectroscopy of unfunctionalized and quantum defect-tailored SWCNTs in a magnetic field. **a**, PL spectra (upper panel) of the E_{11} emission for a single, unfunctionalized (6,5)-SWCNT without a magnetic field (grey) and in magnetic fields of 4 T and 8 T (brown and orange, respectively). Grey solid lines show Lorentzian fits to the bright and dark exciton peaks with their total contribution to the PL spectrum, shown as a solid blue line. The lower panel shows the color-coded PL energy dispersion of the same nanotube in magnetic fields ramped up in steps of 1 T, highlighting the transfer of the oscillator strength from the bright to dark exciton. The inset shows the evolution of the bright-dark splitting of the singlet E_{11} excitons with the Aharonov-Bohm effect induced by the magnetic field (plotted as Δ^2 vs. B^2, with the fit to the data according to $\Delta^2 = \Delta_0^2 + \Delta_{AB}^2$ shown as the solid blue line). **b, c**, PL spectra for the E_{11}^- and E_T peaks of an individual (6,5)-SWCNT-C_6H_{13}. No brightening of dark satellites was observed within the energy range of 100 meV around the E_{11}^- and E_T peaks, suggesting that lower-lying dark exciton states are absent in the quantum defect-tailored nanotubes.

5.3.4 Extraordinarily Large Binding Energies of Trions in Deep Trapping Wells

To better understand the origin of the unexpectedly bright trions, we further determined the binding energies, E_b, of these quantum defect-trapped species. Caught in a deep trap, a trion is expected to have a larger binding energy due to enhanced Coulomb interactions between the exciton and electron.[120]

The binding energy of a negative trion is the minimum energy required to bind an exciton and an electron. For mobile trions in unfunctionalized SWCNTs,[106,111] this binding energy can be determined by subtracting from ΔE_T the energy splitting between the triplet dark E_{11} exciton, which is the lowest energy state, and the singlet bright E_{11}. By subtracting from ΔE_T (253 meV) the dark-triplet bright-singlet splitting (69.7 meV),[20] we obtained a binding energy of 183 meV for (6,5)-SWCNT-C_6H_{13}, compared to 54 meV for mobile trions in unfunctionalized (6,5)-SWCNT.[109,111]

Intriguingly, for a trapped trion, as it dissociates, either the exciton or the electron may remain trapped. Since it takes more energy for an exciton than an electron to escape the trap, the binding energy of a trapped trion would be the minimum energy required to dissociate into an exciton, which remains trapped at the quantum defect, and an electron. On the energy ladder, both the trapped trion and trapped exciton are located deeply and well below that of the low-lying dark states of E_{11} excitons (Figure 5-8; Table 5-5). Furthermore, since dark states are not observed in the energy vicinity of the trapped trion or trapped exciton, the lowest energy state is optically allowed for both excitons and trions when they are trapped at a quantum defect. Therefore, the binding energy of a quantum defect-trapped trion is simply the energy difference

between the trapped trion and trapped exciton, which can be experimentally determined directly from E_T and E_{11}^- to be 119 meV. This binding energy is lower than that is derived from the conventional picture (183 meV), but even with this conservative lower-bound value (119 meV) the binding energy of a trapped trion is still significantly larger than that of mobile trions in unfunctionalized (6,5)-SWCNT (54 meV),[109,111] 0D quantum dots (2–25 meV),[100,104] and also 2D materials (15–45 meV).[112]

This extraordinarily large binding energy explains the unexpected brightness observed for trapped trions. By systematically varying the chemical nature of the quantum defects, ranging from nonfluorinated ($-C_6H_{13}$), partially fluorinated, and perfluorinated ($-C_6F_{13}$), we found it is possible to tune the well depth and the binding energy of the trapped trion (Figure 5-8; see also Table 5-5). We also observed that as the potential well became deeper (as indicated by E_{11}^-), E_T PL is weaker (Figure 5-9). This observation was initially unexpected, but can be understood as a result of the electronic inductive effects of fluorine on the alkyl defects and can be quantitatively correlated to the Taft constant, σ^* (ref.). On the one hand, the fluorine pushes down the well allowing the exciton to be trapped more deeply. On the other hand, with its electron withdrawing capability the fluorine may pull electron density away from the trapped trion and as a consequence, E_b of the trapped trion decreased by 38 meV for (6,5)-SWCNT-C_6F_{13} compared to the $-C_6H_{13}$ defects. Extrapolating the E_{11}^- and E_T curves in Figure 5-8, we suspect that the trion may lose its brightness when σ^* becomes significantly more negative, since it would cross the dark states, while on the other side the binding energy may decrease to a level inadequate to bind the electron-hole-electron as a quasiparticle. This inductive effect suggests the possibility of electrically

gating the generation of excitons and trions at chemically incorporated defect sites, which will be verified in future experiments.

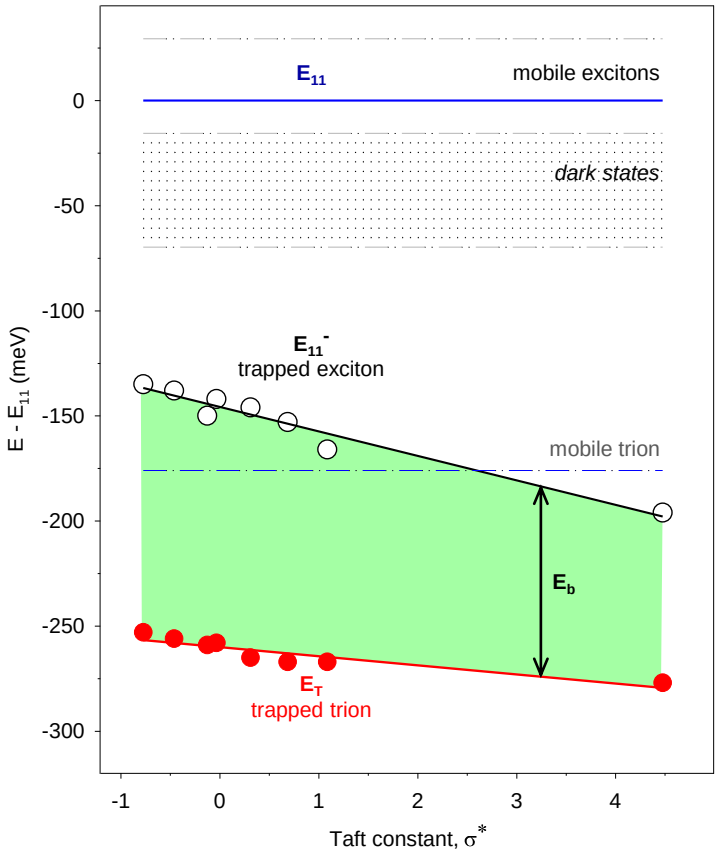

Figure 5-8 Binding energies of quantum defect-trapped trions. The emission energies of E_{11}^- (black dots and line) and E_T (red dots and line) decrease linearly with the Taft constants of the functional groups that create the quantum defects in (6,5)-SWCNTs. The bright-dark splitting of E_{11} excitons is plotted as theoretically predicted[20] energies of dark states (shaded), bound by the low-lying singlet dark state and the lowest, triplet state which is dark. The energy level of the mobile trion[111] is also plotted for comparison.

Table 5-5 The binding energy of trions in (6,5)-SWCNT-R as a function of the chemical nature of the quantum defect. Note that σ_{calc} is the Taft constant for each alkyl functional group calculated based on an empirical formula[121].

R	σ_{calc}	E_{11} (nm)	E_{11}^- (nm)	E_T (nm)	ΔE_T (meV)	E_b (meV)
$-(CF_2)_2(CF_2)_3CF_3$	4.48	986	1168	1265	277	81
$-(CH_2)_2(CF_2)_3CF_3$	1.09	984	1133	1248	267	101
$-(CF_2)_2CF_2CF_3$	0.69	978	1112	1239	267	114
$-(CF_2)_4CF_2CF_3$	-0.13	980	1112	1232	259	109
$-(CH_2)_2CF_3$	0.31	980	1108	1240	265	119
$-(CH_2)_2CH_2CF_3$	-0.03	980	1104	1231	258	116
$-(CH_2)_2(CH_2)_3CF_3$	-0.46	980	1100	1229	256	118
$-(CH_2)_2(CH_2)_3CH_3$	-0.77	981	1098	1227	253	119

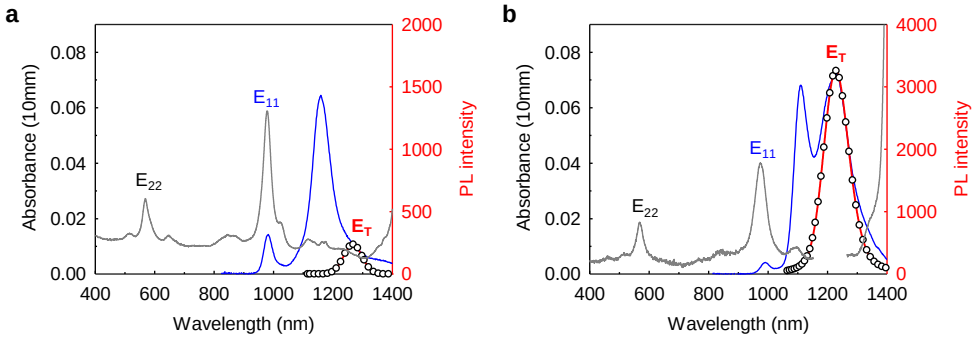

Figure 5-9 Optimized trion brightening in (6,5)-SWCNT-C_6F_{13} and -C_6H_{13} from ensemble measurement. Absorption and PL spectra of **a,** (6,5)-SWCNT-C_6F_{13} and **b,** (6,5)-SWCNT-C_6H_{13}. Based on Eqn. 5-1, the relative PL brightness for trions are calculated to be 0.6 and 5.4 for (6,5)-SWCNT-C_6F_{13} and (6,5)-SWCNT-C_6H_{13}, respectively.

5.4 Conclusions

We observed ultra-bright PL from trions trapped at quantum defects that were synthetically created in semiconducting SWCNT hosts by covalent bonding of alkyl groups to the sp^2 carbon lattice. The trapped trion is nearly 8-times as bright as the native nanotube excitons, with a photoluminescence lifetime that is more than 100 times larger than "free" trions in the same host material. This unexpected brightness arises from strong localization of the trion in the deep potential well of the quantum defect, giving rise to an extraordinarily large binding energy for this tri-carrier quasiparticle (119 meV in (6,5)-SWCNT-C_6H_{13}). Magnetoluminescence spectroscopy suggests that the lowest energy states for these quantum defect-trapped quasi-particles are optically allowed. With ultra-bright trions, it is now possible to manipulate charged excitons with non-zero spin, which provides an ideal platform for studying fundamental photophysics, including dark exciton states in low-dimensional carbon materials and many-body physics. Many promising applications derived from these materials can also be expected, including infrared bioimaging,[12] carrier-doped field effect transistors,[108-109] and quantum information science.[97]

6 Dark Exciton Brightening at a Fluorescent Quantum Defect

Adapted from a manuscript by Kim, M.; Wu. X.; Qu, H.; Huang, Z; Xu,B; Wang, Y.

Y.W. and M.K. conceived and designed the experiments. M.K., X.W., and H.Q. performed the experiments. Z.H. and B.X. prepared substrates for imaging. M.K. wrote the manuscript.

6.1 Introduction

Because of the unique electronic structure and optical properties, semiconducting SWCNTs can be used for single-photon sources,[11] imaging,[12] sensing,[122] and other important optoelectronic applications.[123] However, the quantum yields of SWCNTs are surprisingly low (3% ± 1% in water,[124] and even worse for aggregated nanotubes[10]), limiting their practical applications. These low quantum yields have been attributed to the trapping of E_{11} exciton at quenching sites, including hole-dopants (*e.g.*, protons[43] and oxygen[115]), impurities,[43,115,125] and structural defects, which increase the probability of nonradiative recombination.[36,114] Various strategies have been implemented to minimize the nonradiative decay of E_{11} excitons at these quenching sites.[27,87,124,126-127] For instance, one can avoid the creation of structural defects by the nondestructive SWCNT processing,[27] hole passivation *via* oxygen-excluding surfactant organization,[126] and removal of quenching defects using reducing agents.[87]

Even though these methods can brighten the SWCNT PL, the brightening effects may not be permanent[124] and more importantly, will be limited by the probability distribution of bright exciton population (< 10%) due to the low-lying dark states in the electronic structure of SWCNTs.[38] The intrinsic electronic structure of

SWCNTs is composed of 12 triplet and 4 singlet excitonic states due to the spin degeneracy[18] and intervalley short-range Coulomb interactions.[19] Within the manifold of excitonic states, only one singlet state is optically allowed.[18-19] There are 13 dark states below the bright state, making excitons sink into lower lying 'dark' singlet or triplet states,[20-21] from which energy is typically lost as heat.[128]

Miyauchi *et al.*[37] have reported that the PL quantum yield in oxygen-doped SWCNTs can exceed the limit of intrinsic E_{11} excitons[38,127] by the dimensionality modification of excitons (18% for 0D exciton vs. 1% for 1D exciton). Exciton localization at an oxygen doped site in a SWCNT[71] not only reduce the probability of non-radiative decay of 1D excitons at quenching sites but also confine the exciton in the 0D state, increasing its radiative decay rate. However, the quantum yield enhancement through the dimensionality modification is still limited by the population of bright E_{11} excitons. Because the bright excitons only account for 10% of a total E_{11} exciton population in unfunctionalized (6,5)-SWCNTs,[38] a way to harness the optically inaccessible dark excitons is the key to achieve significant enhancement of the quantum yield of SWCNTs.

Fluorescent quantum defects are sp^3 defect centers that can be synthetically incorporated in SWCNTs by controlled chemical reactions.[13-15] The synthetic quantum emitters trap mobile excitons[57] and allow the trapped excitons to fluoresce as E_{11}^-. Even though the fluorescent quantum defects are analogous to the oxygen-doped state in terms of dimensionality modification, various electronic properties make them distinguishable from other defect systems. For example, the fluorescence quantum defects feature deep trapping potential and the reversed ordering of bright and dark

states in E_{11}^{-} excitons,[60] which may improve the stability of defect PL emission. However, how these properties benefit the optical properties of SWCNTs and how dark excitons behave at the fluorescent quantum defects have not been unambiguously explained.

In this contribution, we report the evidence for dark exciton brightening from fluorescent quantum defects. To access the brightening factor by defect trapped dark excitons, we employed super-resolved hyperspectral PL imaging, which enables direct measurement of spatially localized defect PL spectra of SWCNTs at the single defect level. Remarkably, the quantum yield of defect-trapped excitons is 51.5% in (6,5)-SWCNT-$C_6H_4OCH_3$, which is at least 5 times greater than the fundamental limit of bright excitons in unfunctionalized SWCNTs. To explain the origin of brightening, both extrinsic and intrinsic factors of PL enhancement are analyzed. The unexpected brightening results from the characteristics of fluorescent quantum defects; deep trapping of excitons at the lowest-lying bright defect state. Our findings reveal the contribution of dark exciton brightening in E_{11}^{-} PL (at least by a factor of 1.5) and suggest significant potential for chemically engineered fluorescent quantum defects as an effective system to harness dark excitons.

6.2 Experimental Section

6.2.1 Sample Preparation of Chirality Enriched Long (6,5)-SWCNTs

CoMoCAT SG65i SWCNTs(Southwest Nanotechnologies, lot no. SG65i-L39) were stabilized in ozonated nanopure water as individual particles wrapped with 1 %wt/v sodium deoxycholate (DOC, Sigma Aldrich, > 97%) using gentle stirring at 25 ^{o}C for several months.[25] Chirality pure (6,5)-SWCNTs were then isolated by polymer aqueous two-phase separation.[30] The sorted SWCNTs were stabilized in 1%wt/v DOC-D_2O (Cambridge Isotope Laboratories, Inc., 99.8%) to retain the stability in the aqueous solution.

6.2.2 Covalent Functionalization of Long (6,5)-SWCNTs by 4-Methoxyaryl Defects

For the subsequent functionalization and spectroscopic characterization, the optical density of (6,5)-SWCNT solutions was adjusted 0.06–0.12 at 988 nm by diluting the concentrated (6,5)-SWCNT into 1% SDS-D_2O (Sigma Aldrich, > 98.5%). UV-Vis-NIR absorption spectra were measured with a spectrophotometer equipped with a broadband InGaAs detector (Lambda 1050, PerkinElmer).

The covalent functionalization of aryl defects follows the steps established in ref [53]. An adequate amount of aqueous 4-methoxybenzenediazonium tetrafluoroborate (Sigma Aldrich, 98%) was added to the SWCNT solution. The illumination of 565 nm light (resonating with E_{22} transition of (6,5)-SWCNT) accelerates the covalent functionalization and enables monitoring the reaction progress by *in situ* PL spectroscopy. When the desired defect PL intensity was reached, the functionalization

was quenched by diluting the solution using 4 %wt/v DOC. Adding 2 mL of 4 %wt/v DOC-D_2O to 0.5 mL SWCNT solution is sufficient to stabilize the SWCNT dispersion as well as to stop the further reaction. Also, DOC coating protects SWCNTs from photobleaching by laser excitation during PL imaging. The PL of the SWCNT solutions, (6,5)-SWCNT-$C_6H_4OCH_3$ was characterized with a Horiba Jobin Yvon NanoLog spectrofluorometer equipped with a liquid-N_2 cooled InGaAs array.

6.2.3 Sample Preparation for PL Imaging

For PL imaging using a 100x objective, the substrates were prepared by thermal deposition of 60 nm thick Au and 5 nm thick Ti layers on a silicon wafer. The Au and Ti layers improve the photon collection efficiency by reflecting the NIR light. For imaging with the oil-immersion 150x objective, a cover glass (Ted Pella, Inc., Goldseal® Cover Glass, 0.08–0.13mm thick) was used as a substrate. On the top of the Au/Ti/Si substrate or cover glass, 3% polystyrene (PS) in toluene was spin-coated to form a 50 nm thick layer and then, the substrates were baked at 80 ^oC under vacuum for several hours to remove charge trap states and suppress blinking of SWCNTs.[129-130] We note that the potential variation in the thickness of polystyrene layer is almost independent of the reflectivity in the 850–1550 nm range, where SWCNTs fluoresce (Figure 6-1). To achieve the sparse coverage of SWCNTs on a substrate (1–2 SWCNTs in 100 μm^2), 5 uL of the SWCNTs in 3.4 wt/v% DOC was added on the substrate and immediately blown dry with air.

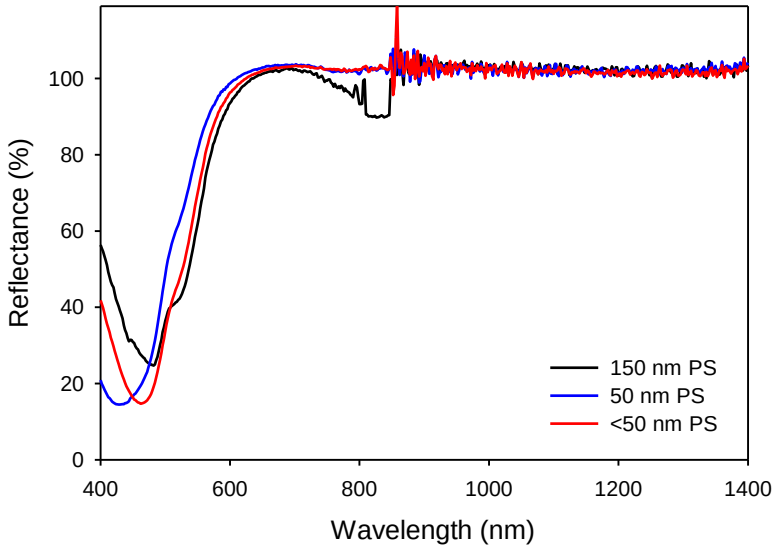

Figure 6-1 Reflectance of PS/Au/Ti/Si substrates in the visible and NIR region. The NIR reflectivity of the substrates is nearly 100% regardless of the thickness of polystyrene layer.

6.2.4 Super-Resolved Hyperspectral PL Imaging

Single tube PL imaging was performed on a custom-built hyperspectral PL imager as shown in Figure 6-2. The instrument comprises an inverted microscope (Nikon, Eclipse Ti-U) equipped with a 100x objective (LCPLN100XIR, NA = 0.85, Olympus) and a 150x objective (UAPON150XOTIRF, NA=1.45, Olympus). SWCNTs were excited with continuous-wave diode lasers at 730 nm (Shanghai Dream Lasers Technology) and 561 nm (Cobolt) at <100 W/cm^2 power density. The power density of excitation sources was modulated by controlling the input current (only for 730 nm laser) and placing a neutral density filter (Edmund Optics) in the excitation light path (NDF in Figure 6-2). The excitation power density at the sample stage was measured with an optical power meter (Newport 1916-C) and silicon detector (Newport 918-

SLOD3). The emission wavelengths were selected by a volume Bragg grating, which allows broad-field imaging at 4 nm spectral resolution in the NIR (850–1550nm), providing a high-throughput tool for studying a large number of SWCNTs in the field of view. Because the angular selectivity of the grating results in a gradient in wavelength (50 nm) across the field of view in the vertical axis in each PL image, a stack of PL images was rectified to obtain a hyperspectral cube with monochromatic images. The PL emission was collected using a liquid-N_2 cooled 2D InGaAs detector with 648×520 pixels (Cougar 640, Xenics, Inc.) using Read While Integrate mode (RWI). The RWI mode reads the accumulated photoelectrons non-destructively during the integration period without resetting the buffering capacitors, enabling ultra-low noise levels (few electrons per second). The nonlinear responses to wavelength and intensity of each pixel were calibrated using a calibrated light source (Ocean Optics, HL-3P-INT-CAL-EXT) and integrating sphere (Thorlabs, IS200). Because the detector displays the accumulated charge as the counts in analog-to-digital converter units (ADU), we generated a correction cube for wavelength calibration that converts the ADU to the absolute photon counts, emitting from a sample at each wavelength. A series of Matlab algorithms was implemented for post-processing of the data.

To collect the blinking profiles of E_{11} and E_{11}^- PL in a field of view, appropriate longpass or bandpass filter, denoted by LP or BP in Figure 6-2 (Thorlabs, FB980-10 and FELH1100) were used instead of the volume Bragg grating system. The videos of SWCNT blinking were recorded for 10 min with a frame rate of 2–6 frames-per-second. After the video recording, the blinking profiles were obtained from the linear regression of the raw data. Differential images of the blinking profiles were analyzed

to find the on/off blinking from particular defect sites. Each spot in a differential image was then fitted by a 2D Gaussian profile with the plug-in GDSC SMLM (ImageJ), as used in single molecule localization microscopy,[131-133] to retrieve the emitter localization with sub-diffraction precision.

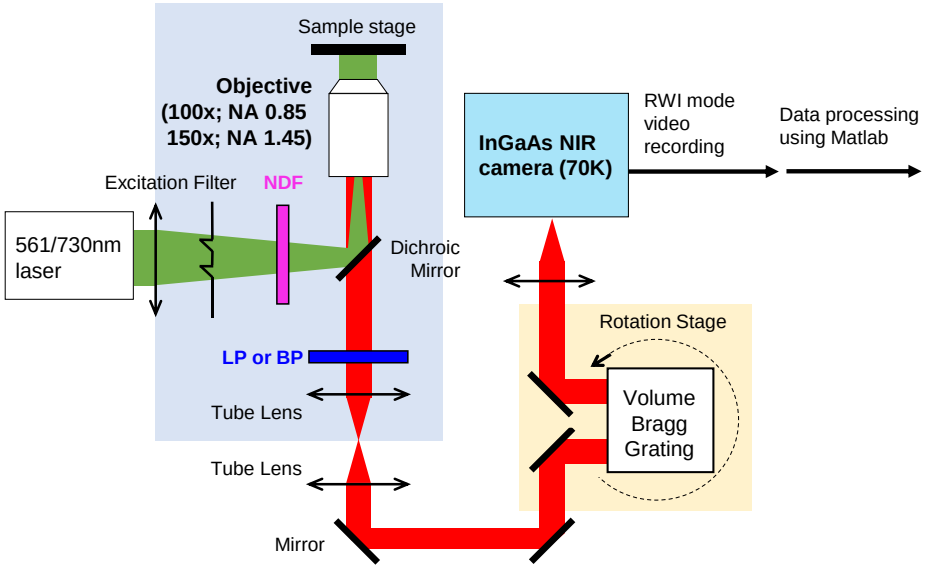

Figure 6-2 Schematic of the super-resolved hyperspectral imaging system.

6.3 Results and Discussions

6.3.1 Incorporation of Spatially Isolated Fluorescent Quantum Defects

Figure 6-3 shows the PL spectra of the unfunctionalized and functionalized (6,5)-SWCNT-$C_6H_4OCH_3$ in 1% SDS-D_2O. To resolve individual fluorescent quantum defects from single tube imaging, we functionalized SWCNTs with a low density of 4-methoxyaryl defects. The density of defects was adjusted to few defects in a SWCNT, where the E_{11} PL (centered at 988 nm) decreases to less than 10% of its initial intensity and the E_{11}^- (centered at 1128 nm) is observed as a small peak in the ensemble PL spectrum. The new PL is distinguishable from a low intensity shoulder peak at 1110 nm, which arises from K-momentum dark excitons.[23-24] The E_{11}^- emission wavelength is a signature of 4-methoxyaryl defects in (6,5)-SWCNTs,[14] confirming the covalent attachment of aryl defects to SWCNTs.

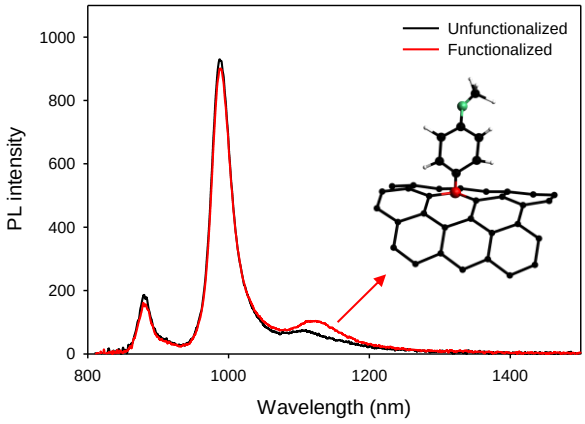

Figure 6-3 PL spectra of the unfunctionalized starting (6,5)-SWCNT (black) and 4-methoxyaryl functionalized (6,5)-SWCNT in 1% SDS-D_2O (red). The peak at 878 nm corresponds to E_{11} of (6,4)-SWCNT. The molecular structure of the fluorescent quantum defect is given in the plot. The excitation wavelength was 565 nm.

6.3.2 Defect PL Blinking Control by Excitation

SWCNT PL should be stable during the acquisition of a reliable hyperspectral cube (~10 min). Conversely, to super-localize defects, blinking profiles of E_{11}^- PL are required. To obtain both the spectral profile and sub-diffraction limit localization information on the same tube, we first determine conditions, that can reversibly control the blinking behavior of SWCNT PL. Thus, we studied the E_{11} and E_{11}^- PL blinking at varying the power and wavelength of the excitation sources. The E_{11} and E_{11}^- PL were recorded by placing 980 nm bandpass and 1100 nm longpass filters to the emission light path, respectively, so that the entire field of view selectively displays the E_{11} and E_{11}^- of (6,5)-SWCNT. The frame time was 0.5 s, and the PL profiles were monitored for 10 min.

For 730 nm excitation, we varied the excitation power densities from 5 W/cm^2 to 60 W/cm^2. Within the power density regime, both E_{11} and E_{11}^- PL intensities are proportional to the excitation power density (r^2 = 0.995 for Figure 6-4a and r^2 = 0.960 for Figure 6-4b) and the noise levels of E_{11} and E_{11}^- emission are comparable to that of background signal (Figure 6-4b,d). These indicate that blinking was completely suppressed over the video recording and the excitation condition is suitable to collect hyperspectral cubes.

For 561 nm excitation, E_{11} PL was stable and linear to varying the power density from 10 W/cm^2 to 80 W/cm^2, consistent with previous observation on blinking of unfunctionalized SWCNTs.[134] Conversely, we have observed the nonlinear E_{11}^- PL response for at the power density higher than 19.7 W/cm^2 since strong 561 nm excitation induces the blinking of E_{11}^- PL (Figure 6-5).

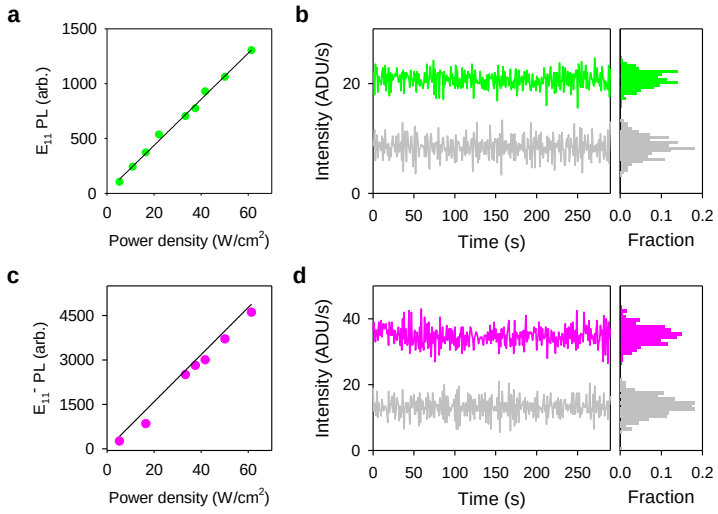

Figure 6-4 Power dependence of **a,** E_{11} and **c,** E_{11}^- PL intensities of (6,5)-SWCNT-$C_6H_4OCH_3$ on a PS/glass substrate under 730 nm excitation. The solid lines in the plots are linear fitting of the correlations. The **b,** E_{11} (green) and **d,** E_{11}^- (pink) intensity traces over time and the histogram of the time traces. The gray traces are background signal. The time correlated PL traces were collected under the power density of 60 W/cm^2. The frame rate was 2 frames per second.

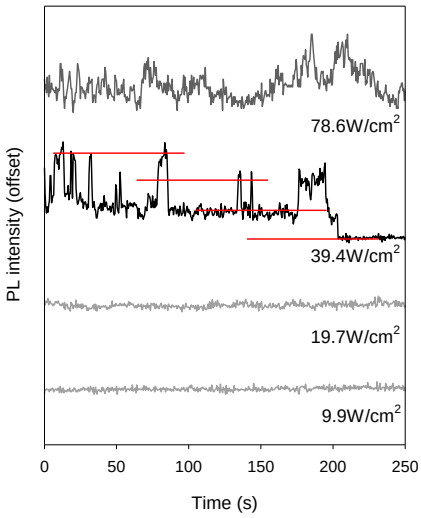

Figure 6-5 Power dependence of E_{11}^- PL intensities of (6,5)-SWCNT-$C_6H_4OCH_3$ on a PS/glass substrate under 561 nm excitation. The plots are the E_{11}^- intensity traces over time at the excitation power densities of 9.9, 19.7, 39.4, and 78.6 W/cm^2. At the power density higher than 39.4 W/cm^2, the blinking dominates the E_{11}^- PL intensity. Red lines guide three-step blinking in the E_{11}^- emitting area.

Although the blinking mechanism is still unclear, we have confirmed that the power dependence of blinking is reproducible. In addition, the blinking frequency is related to the power density. When the power density is increased to 78.6 W/cm^2 at 561 nm excitation, we no longer observe the clear on-off blinking at the given frame time (0.5 s) but the intensity profile appears to be flickering due to the frequent blinking. Given by the slow exciton generation rate at the excitation condition (few excitons per nanosecond) and long lifetime of off state, the blinking is not caused by exciton-exciton interactions at a fluorescent quantum defect,[135] *e.g.* exciton-exciton annihilation[66,106-107] and phonon-assisted up-conversion at defects.[72] We suspect that the PL blinking is attributed to optical generation of transient quenching states in SWCNTs.[134] Strong electrostatic potential in the vicinity of quantum defects makes the defects as an antenna to generate optical quenchers.[cite Hartmann Nanoscale]

In contrast to 730 nm excitation, which is weakly resonant with (6,5)-SWCNT, 561 nm excitation is slightly off-resonant (~5 nm) from the E_{22} of (6,5)-SWCNTs. Based on the PL excitation spectrum of (6,5)-SWCNT at E_{11} and the literature value of absorption cross section of (6,5) E_{22} (0.61×10^{-17}cm^2/C),[136] we derive absorption cross sections for 730 nm and 561 nm as 0.07×10^{-17}cm^2/C and 0.41×10^{-17}cm^2/C, respectively. The difference in the absorption cross sections suggests that the number of photogenerated excitons in (6,5)-SWCNT can be approximately 4 times higher with 561 nm excitation than with 730 nm excitation at the same power density. Therefore, we used 730 nm excitation at <60 W/cm^2 to collect the hyperspectral PL cubes that records the stable PL signal for a relatively long time (~10 min) and at 561 nm excitation at 39.4 W/cm^2 to induce blinking of E_{11}^-.

6.3.3 Super-Resolved Hyperspectral PL Imaging

Figure 6-6 shows the hyperspectral PL imaging of unfunctionalized (6,5)-SWCNT on a PS-coated glass substrate under 730 nm excitation (30 W/cm^2). For the unfunctionalized SWCNT, the PL image at 988 nm displays homogeneous E_{11} intensity profile along SWCNT length. Because the SWCNT ends are effective quenching sites for E_{11} excitons, fitting the E_{11} PL profile using the diffusion equations gives the exciton diffusion length (l_D) in the SWCNT.[38] The calculated exciton diffusion length ranges from 150 to 350 nm (median l_D = 200 nm). The intensity profile perpendicular to the SWCNT axis closely follows the Gaussian fitting with 143 nm standard deviation which approximates a slice of Airy disk for the objective NA of 1.45 and the 988 nm emission wavelength, confirming that the PL is a diffraction-limited image.

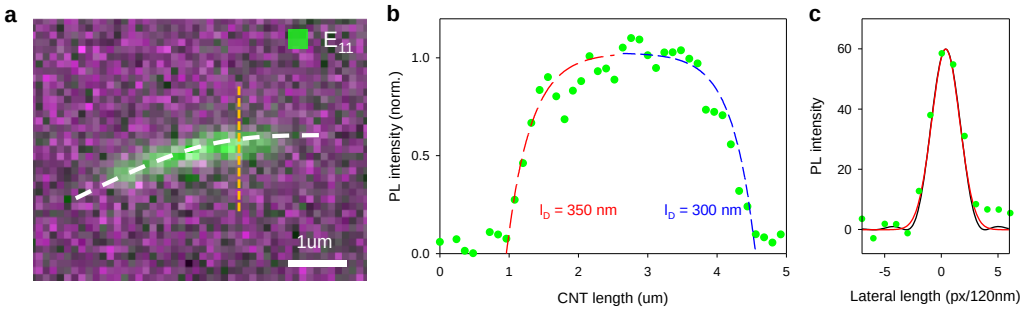

Figure 6-6 Hyperspectral PL imaging of unfunctionalized (6,5)-SWCNT. **a,** E_{11} PL image of a (6,5)-SWCNT on a PS coated cover glass. The white and orange lines guide the intensity cross sections parallel and perpendicular to the SWCNT axis. **b,** Intensity cross section along the SWCNT axis. The red and blue lines indicate the solution of the 1D diffusion equation for different boundary conditions described in the text convolved with the Airy disk. **c,** Intensity cross section perpendicular to the SWCNT axis. Black and red lines indicate the Airy disk and Gaussian fitting for λ = 988 nm and NA = 1.45. The standard deviation of the fitted Gaussian is 143 nm. The excitation wavelength was 730 nm at 60 W/cm^2.

In the hyperspectral cube of a functionalized (6,5)-SWCNT with 4-methoxyaryl defects, an E_{11}^- emitting site is spectrally distinct and spatially resolved along the nanotube while E_{11} emission is continuous in the SWCNT (Figure 6-7). We assigned the E_{11}^- emitting site to the region of interest 2 (ROI 2) and the unfunctionalized region near ROI 2 to ROI 1, as shown in Figure 6-7. The intensity cross section of ROI 2 in any direction can be fitted by a Gaussian function, whose standard deviation is 164 nm, suggesting that ROI 2 is a diffraction-limited image of a single E_{11}^- emitting point. Interestingly, as the PL images of E_{11} and E_{11}^- PL are combined to spatially correlated defect PL to a SWCNT, the E_{11}^- profile is complementary to E_{11} profile, suggesting that the E_{11}^- PL originates from the same (6,5)-SWCNT (Figure 6-7b). The integrated E_{11} PL intensity at ROI 2 is 20% of the integrated E_{11} PL at ROI 1 in the PL spectra (Figure 6-7c). We note that the considerable E_{11} intensity difference between two ROIs is related not only to exciton trapping at the fluorescent aryl defect but also to the position of the defect in the SWCNT. ROI 2 is close to the SWCNT end, which is an effective quenching site for E_{11} excitons. As the E_{11} intensity decays at the SWCNT ends, we should deconvolute the E_{11} intensity reduction into the effects of end quenching and exciton trapping at the fluorescent quantum defect for the quantitative analysis on E_{11} excitons.

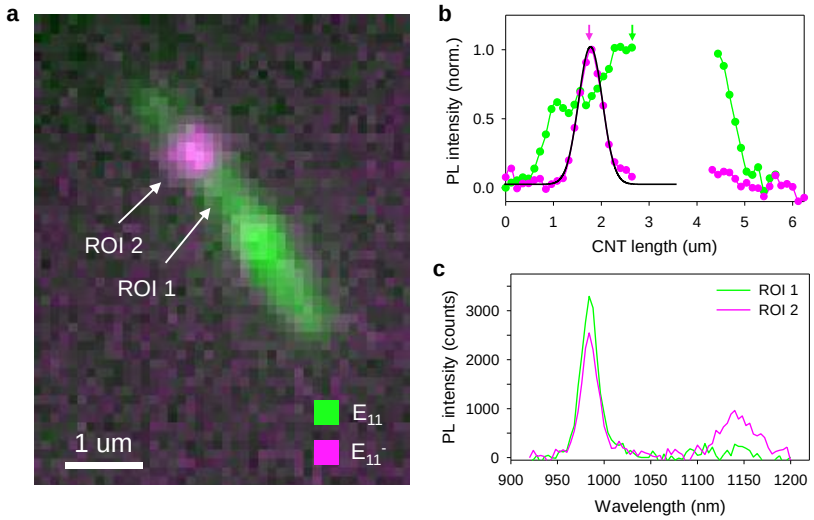

Figure 6-7 Hyperspectral PL imaging of (6,5)-SWCNT-$C_6H_4OCH_3$. **a,** E_{11} (green) and E_{11}^- (pink) PL image of a (6,5)-SWCNT on a PS coated glass substrate. **b,** The E_{11} (green) and E_{11}^- (pink) intensity cross section along the SWCNT axis. A black line is the Gaussian fitting of E_{11}^- PL profile with σ =164 nm, which corresponds to a diffraction-limited profile for 1.45 NA and 1124 nm emission wavelength. **c,** PL spectra of unfunctionalized (ROI 1 in **a** and green arrow in **b**) and functionalized (ROI 2 in **a** and pink arrow in **b**) region in the same (6,5)-SWCNT.

To confirm the number of fluorescent defects at the E_{11}^- emitting site, the E_{11}^- PL intensity traces were recorded for 10 min under 561 nm excitation at 39.4 W/cm^2. By taking the difference of single step blinking, we were able to superlocalize defects in SWCNT. As is well established in super-resolution microscopy,[131-133] the location of each defect site was extracted by fitting the diffraction-limited pattern with a 2D Gaussian function, which approximates the Airy disk for the objective NA of 1.45 and the emission wavelength of 1128 nm:

$$f(x,y) = Aexp\left(-\frac{1}{2}\left(\frac{(x-x_0)^2}{\sigma^2}+\frac{(y-y_0)^2}{\sigma^2}\right)\right) \qquad \text{Eqn. 6-1}$$

in which A is the peak intensity, x_0 and y_0 are the center position of the peak, and σ is the standard deviation for the emission wavelength and the numerical aperture of objective.

We found one-step blinking in ROI 2 and multi-step blinking in another (6,5)-SWCNT-$C_6H_4OCH_3$ with a constant blinking amplitude (Figure 6-8). Based on the blinking profile, we can super-resolve the center position of light emitting sites with a spatial resolution better than 20 nm. The results show the superlocalization of a single defect in ROI 2 and three adjacent defects closer than the diffraction limit (660 nm) in another example. The superlocalization of defects confirms that the integrated E_{11}^- PL in the hyperspectral cube is related to the number of photons emitted from a single fluorescent quantum defect.

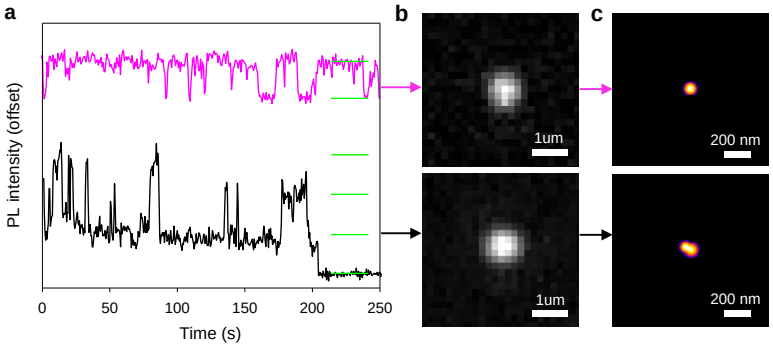

Figure 6-8 Super-resolved fluorescent quantum defects. **a,** E_{11}^- PL profile of ROI 2 (pink) and another defect site of (6,5)-SWCNT-$C_6H_4OCH_3$ (black). The step size of blinking is identical to the same defect type. **b,** Diffraction-limited PL images where the blinking occurs. **c,** Superlocalization of a single defect (top) and three defects (bottom).

6.3.4 Calculating the Brightening Factor of a Defect-Trapped Exciton

The probability of radiative recombination of defect trapped excitons (η_{11}^-) can be defined as the ratio of the number of E_{11}^- photons emitted from a single fluorescent quantum defect (N_{11}^-) and the number of trapped excitons (N_{trapped}).

Considering the diffusion of photogenerated 1D excitons and successive trapping by a local defect state (E_{11}^-), the number of trapped excitons (N_{trapped}) at fluorescent aryl defects can be expressed as:

$$N_{\text{trapped}} = N_{\text{abs}} \frac{k_{dif}}{k_i + k_{dif}} P_{\text{trapped}} \qquad \text{Eqn. 6-2}$$

in which N_{abs} is the number of E_{11} excitons generated after photoabsorption; k_{dif} is the effective decay rate of the E_{11} excitons due to exciton diffusion and successive trapping at the local quenching sites (including intrinsic quenching sites, physisorbed aryldiazonium molecules, and aryl defects); and k_i is the effective decay rate for all possible mechanisms of exciton recombination other than the diffusion-limited processes. In our calculation, we ignored the contribution of k_i ($k_i \ll k_{dif}$) and thereby $\frac{k_{dif}}{k_i + k_{dif}} \sim 1$. The last component of Eqn. 6-2, P_{trapped} refers the probability of diffusing excitons to be trapped at fluorescent quantum defects within SWCNT length and can be expressed as

$$P_{\text{trapped}} = \frac{n_{11}^-}{n_q + n_{11}^-} = \frac{n_{11}^-}{[Q] \cdot l + n_{11}^-} = \frac{n_{11}^-}{(d_q{}^{-1} + l^{-1}) \cdot l + n_{11}^-} \qquad \text{Eqn. 6-3}$$

in which n_q is the number of defects on the SWCNT, induced by intrinsic quenching sites and physisorption of aryldiazonium molecules; and n_{11}^- is the number of fluorescent quantum defects; $[Q]$ is the concentration of effective quenching sites; l is

the SWCNT length; d_q is the sum of the average bulk quenching site distance in the absence of end quenching ($d_q=\pi^{-1/2}l_D$). We note that the conversion factor from a mobile E_{11} exciton to a trapped E_{11}^- exciton is 1 to avoid the overestimation of the quantum yield calculation.

If we consider the trapping probability for a single fluorescent defect, which is isolated from other fluorescent defects at least by $2l_D$ on each side (Figure 6-6b):

$$P_{\text{trapped}} = \frac{n_{11}^-}{(d_q{}^{-1}+l^{-1})\cdot l+n_{11}^-} = \frac{1}{(d_q{}^{-1}+l^{-1})\cdot l+1} = \frac{1}{4\sqrt{\pi}+2} = 0.11\,. \qquad \text{Eqn. 6-4}$$

Thereby, we can simplify the number of trapped excitons at a single fluorescent defect of (6,5)-SWCNTs within the range of $4l_D$ as

$$N_{\text{trapped}} = 0.11\mathrm{N}_{\text{abs}}. \qquad \text{Eqn. 6-5}$$

Based on Eqn. 6-5, we derived the number of trapped excitons at the single fluorescent 4-methoxyaryl defect of the (6,5)-SWCNT under 730 nm excitation at 30 W/cm^2 as 6.62×10^5 photons/s in $4l_D$ (1.2 μm). N_{abs} is calculated by multiplying the excitation photon flux per unit area, the absorption cross section of (6,5)-SWCNT at 730 nm, and the number of carbon atoms in $4l_D$ long (6,5)-SWCNT (~1.4×10^5 atoms).

The number of photons emitted from a fluorescent quantum defect (N_{11}^-) can be directly measured by integrating the PL intensity fitted by 2D Gaussian function over the E_{11}^- emission wavelength (1100–1200 nm in the hyperspectral cube). The calculation gives 3.40×10^5 photons emitted from the single 4-methoxyaryl defect per second under the 730 nm excitation at 30 W/cm^2. Consequently, the quantum yield of defect trapped excitons (η_{11}^-) is as high as 51.3% for (6,5)-SWCNT-$C_6H_4OCH_3$ at room temperature. As a comparison, the quantum yield of E_{11} excitons in the unfunctionalized (6,5)-SWCNT was 5%. Thus, defect-trapped E_{11}^- excitons at 4-

methoxyaryl defects are at least 10-times brighter than free E_{11} excitons and 2.86 times brighter than excitons trapped at oxygen defects in (6,5)-SWCNTs.[37]

6.3.5 Origin of PL Brightening

We attribute the PL brightening to the combined effects of exciton localization[37] and dark exciton harvesting.

Fluorescent quantum defects trap E_{11} excitons before they reach at quenching sites. This exciton trapping reduces the non-radiative decay rate of the trapped excitons by 2 times if the defect-induced E_{11}^- state collects all of the bright E_{11} exciton population (~10%).[38] Once an exciton localizes at a defect site, it has different temperature dependence compared to that of 1D exciton. Although E_{11} PL has a $1/\sqrt{T}$ dependence on the radiative decay rate of E_{11} excitons, arising from the 1D density of states and their thermalization within the exciton band, E_{11}^- PL intensity is independent to temperature because of δ-function like (0D) density of states.[78,137] The different temperature dependence between 1D and 0D excitons leads to the PL enhancement by a factor of 1.6.

In addition, the 0D localization of E_{11}^- excitons introduces additional brightening factor due to the giant-oscillator-strength effect. The defect-induced states carry the large oscillator strength due to the exciton squeezing at the defect center.[63] The radiative decay rate of E_{11}^- exciton is proportional to the square of exciton energy and inversely proportional to the exciton size. Quantum chemical modeling in my previous publication[60] also revealed that the bright E_{11}^- exciton in aryl defect tailored or oxygen-doped SWCNTs is strongly localized on ~ 1 nm length scale, whereas the

E_{11} exciton is delocalized over 5–6 nm in size (see Figure 4-5). As we account for the different energies and the exciton sizes of E_{11} and E_{11}^- excitons, we can expect the additional PL brightening by a factor of 2.2 at 4-methoxy aryl defects.

The PL enhancement factors described above (×7 in total) can be applied to any defect-induced PL and is almost constant over the various chemical nature of defects since either aryl/alkyl defects and oxygen dopant site can trap mobile E_{11} exciton. However, these factors cannot completely cover the brightening (×10 at room temperature) observed in our experiment.

We attribute the rest of brightening (×1.5) to the contribution of dark excitons. Although the energy states of E_{11}^- excitons are analogous to those of E_{11} excitons in terms of the existence of dark states,[37,57,60] the relative spacing and order can be different depending on the types of defects. The time-dependent density functional theory calculations revealed that the lowest excited state is optically allowed for aryl defects.[60] To analyze the effects of energy spacing, the population distributions between dark and bright states in E_{11} and E_{11}^- excitons are modeled as the Boltzmann distribution between the two states. The fraction of bright E_{11} excitons (P_b) is

$$P_b \approx exp(\Delta/k_BT) \qquad \text{Eqn. 6-6}$$

and the fraction of bright E_{11}^- excitons (P_b^-) is

$$P_b^- \approx exp(\Delta^-/k_BT) \qquad \text{Eqn. 6-7}$$

in which Δ and Δ^- are the energy spacing between bright and dark states ($E_{bright} - E_{dark}$) for E_{11} and E_{11}^- excitons, respectively; k_B is the Boltzmann constant; and T is temperature. Δ is known to be –6 meV for chiral SWCNTs[38,138-139] and Δ^- varies as a function of SWCNT chirality and the chemical nature of defects. We modeled the ratio

of P_b^- and P_b as a function of temperature at different Δ^- values, which corresponds to the PL enhancement factor related to the dark excitons (Figure 6-9). The results show that the fraction of excitons staying at the bright E_{11}^- state can be higher in aryl defects compared to excitons in oxygen dopants or native excitonic states, leading to the PL enhancement by a factor of 1.2–2 at room temperature. Based on the fitting, we obtained the dark-bright splitting in aryl defect state (Δ^-) of 4 meV.

Lastly, we note that the deep trapping potential of aryl defects suppresses an Arrhenius type quenching which is associated with thermal detrapping (Eqn. 6-8).[60]

$$\frac{I_{11}}{I_{11}^-} \propto e^{-\Delta E_{thermal}/k_B T} , \qquad \text{Eqn. 6-8}$$

where I_{11} is the integrated PL intensity of E_{11} PL; I_{11}^- is the integrated PL intensity of E_{11}^- PL; $\Delta E_{thermal}$ is the detrapping energy of E_{11}^- excitons; k_B is the Boltzmann constant; and T is temperature. The temperature dependent PL studies revealed that the detrapping energy of oxygen dopant is only 20 meV (Table 4-1), making 30% of E_{11}^- excitons escape the defect state at room temperature (Figure 6-10). In contrast, the thermal detrapping is inefficient at 4-methoxy aryl defect due to its large trapping potential (as large as 117 meV), and thus the quantum yield of E_{11}^- excitons at aryl defects is higher than other defect systems (*e.g.*, 30% brighter than oxygen-doped SWCNT). Note that the phonon-assisted detrapping of E_{11}^- excitons is also inefficient because $\Delta E_{thermal}$ does not match to the optical phonon modes with the energies of ~170–200 meV.

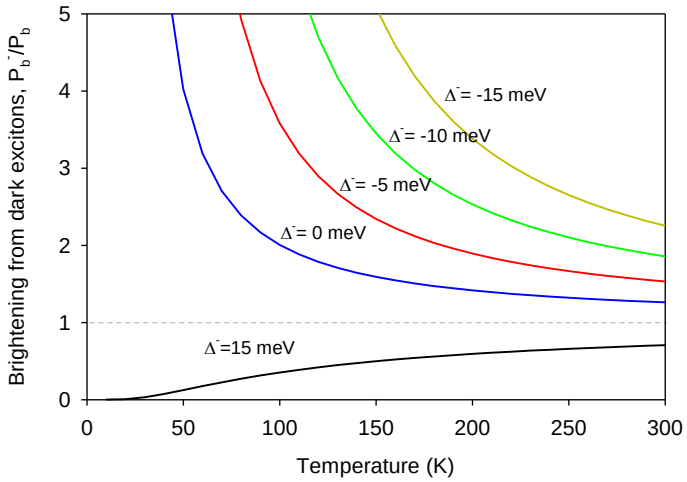

Figure 6-9 Temperature dependence of brightening from dark excitons. As the bright E_{11}^- state is higher than the dark E_{11}^- state ($\Delta^- > 0$), the fraction of bright excitons in E_{11}^- (P_b^-) is similar or lower than that in E_{11} (P_b). Conversely, if the bright E_{11}^- state is same or lower in energy than the dark E_{11}^- state ($\Delta^- \leq 0$), the ratio, P_b^-/P_b is 1.2–2 at room temperature, indicating the dark exciton brightening. The gray dashed line is $P_b^-/P_b = 0$.

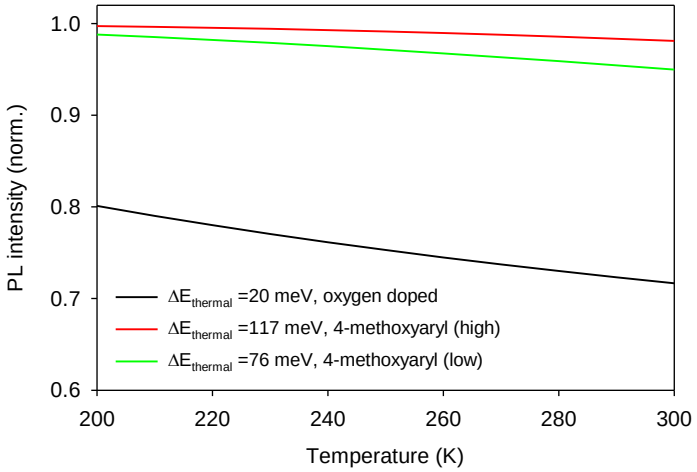

Figure 6-10 Temperature-dependent PL at varying detrapping energy at E_{11}^- state. The detrapping energies of oxygen-doped and 4-methoxyl aryl defects (low and high density of defects) were experimentally derived from the temperature dependent PL spectroscopy.

6.4 Conclusions

We studied the dark exciton brightening at a fluorescent quantum defect. The existence of low-lying dark states in the excitonic energy level is the main reason of low PL quantum yield in unfunctionalized SWCNTs (typically < 1%).[124] Thus, dark exciton is a fundamental issue to the understanding of SWCNT photophysics as well as potential applications. Here we have demonstrated that fluorescent quantum defects offer an efficient channel to harvest dark excitons through deep trapping at the defect site. A super-resolved hyperspectral PL imaging system enables us to probe a single fluorescent aryl defect that is spectrally distinct in the PL spectrum and spatially resolved along the SWCNT in the PL image. From the single tube imaging, we measured the quantum yield of the defect-trapped excitons which is as high as 51.3%. Based on these results, we will further investigate what types of defects provide the highest brightening factor, how the defect PL is correlated to the stability of the SWCNT PL, and how to chemically modulate the local defect state.

7 Summary and Outlook

Single-walled carbon nanotubes have intriguing electronic structure and optical properties, which arise from their 1D nature. The incorporation of fluorescent quantum defects to SWCNTs creates 0D local traps that localize excitons and let the trapped excitons radiatively decay through the defect-induced PL. Understanding the 0D-1D hybrid system is important to chemically control the exciton dynamics and optical properties of SWCNTs and to broaden the applications for quantum light sources, optoelectronics, biological imaging, and more. To enrich our knowledge in this emerging field, my research was directed to provide new insights on chemically-tailored exciton photophysics in fluorescence quantum defects.

7.1 Summary

In this dissertation, I established the structure-property relationships for fluorescent quantum defects in semiconducting SWCNTs to guide the design and synthesis of fluorescent quantum defects. We revealed these relationships based on comparative spectral studies of 14 purified SWCNT chiralities and 30 different functional groups that vary in electron withdrawing capability and bonding configurations. Among the large library of fluorescent quantum defects that are investigated in our studies, the defect emission is tunable by as much as 400 meV in NIR, as a function of SWCNT structure and the chemical nature of the defects. The uncovered insights enable to predict the properties of these fluorescent quantum defects well beyond the set of studied SWCNTs and functional groups. Importantly, our results reveal that the coupling between fluorescent quantum defects and the SWCNT hosts

can be chemically tailored opening the possibility to integrate fluorescent quantum defects directly into electronic devices with desired chemical and quantum properties.

Secondly, I reported the experimental measurement of the trapping depth of excitons at fluorescent quantum defects through temperature dependent PL spectroscopy. Surprisingly, the experimental measurements of the trap depths of the quantum defects show a large energy mismatch between PL spectroscopy and van 't Hoff plots. Through a joint experimental and theoretical effort, we have unambiguously determined that the energy mismatch arises from a substantial reorganization energy between the excited and ground state of carbon nanotubes in the presence of a fluorescent defect. This finding reveals a molecular picture for these quantum defects and suggests the unlimited possibility of chemical tailoring of the electronic properties of carbon nanostructures through chemical engineering. In addition to adding to our understanding of the electronic and optical behavior of these important new defect centers, accurate determination of the relative electronic levels and their relation to the thermal detrapping process are essential for understanding of redox properties of the defect sites, improving PL stability associated with newly revealed single photon emission behavior of the defect sites[48-49], and its relevance to photon upconversion in functionalized SWCNTs[72], which directly arises from thermal detrapping.

Thirdly, I also investigated defect-trapped trions that fluoresce brightly at room temperature. A trion carries a quantum of excitation energy, just like an exciton, but it is electrically charged. Trions are intriguing due to the strong many-body effects and their rich photophysics and optoelectronic properties. However, trions have only ever been observed as a minority species. By the co-localization of an electron and an

exciton at the same quantum defect, we found that it is possible to generate ultra-bright trions in SWCNTs. Due to the deep trapping depth of the fluorescent quantum defects, a defect-trapped trion possesses an extraordinary large binding energy. PL from the defect trapped trions is extremely bright, significantly brighter even than the SWCNT host, and with a PL lifetime more than 100-times longer than the "free" trions. Magnetoluminescence measurements and single molecule imaging suggest that this unexpected brightness arises from the efficient conversion of dark excitons to trions whose lowest energy state is intrinsically bright at the quantum defect site. I anticipate that our findings have a fundamental impact on trion photophysics, dark exciton states, and many-body correlation in low-dimensional materials.

Lastly, I studied how dark excitons behave at fluorescent quantum defects. The low-lying dark states in the excitonic energy level contribute to the low PL quantum yield in unfunctionalized[38,124] and functionalized SWCNTs.[37] To study the contribution of dark excitons at fluorescent quantum defects to PL brightening, we employed a super-resolved hyperspectral PL imaging system, which enables us to probe a single fluorescent aryl defect that is spectrally distinct and spatially resolved along the SWCNT. From the PL imaging, we derived that the quantum yield of a defect-trapped exciton is as high as 51.3% in 4-methoxyaryl defect tailored (6,5)-SWCNT. We have found that fluorescent quantum defects convert dark excitons to bright E_{11}^{-} excitons, leading to at least 1.5 times brightening of E_{11}^{-} PL. Our findings provide important implications to optically access the dark excitons in 0D-1D systems and to design and synthesis efficient NIR emitters for various applications in imaging,[58] quantum light sources, [48-49] and optoelectronics.[123]

7.2 Outlook

SWCNTs are the ideal model systems to study the optical properties of 1D system and to control the carrier mobility by fluorescent quantum defects. Even though it is clear that fluorescent quantum defects have a considerable impact on organic chemistry, solid state physics, and material science, the study of exciton photophysics, electronic structure, and optical properties of defect-tailored SWCNTs is still in its primitive stage. For example, fundamental properties such as fundamental linewidth of defect PL, the trapping efficiency, dark-to-bright conversion ratio at a fluorescent quantum defect have not been unambiguously demonstrated. This lack of information is partially attributed to the difficulty to systematically control the defects by atomic-level precision. Thus, it is important to develop new synthetic methods that can selectively and effectively drive the covalent functionalization in SWCNTs. This work will help to better understand the electronic energy level changes and the degree of coupling and decoupling by the incorporation of fluorescent quantum defects. Another limitation comes from the absence of analytical techniques enabling sensitive detection of fluorescent defects in a single molecular level and simultaneously probe the exciton dynamics. If we can correlate the super-resolved hyperspectral PL imaging to the low temperature, time-resolved PL spectroscopy, this would realize the advance in room-temperature quantum light source and the study of the fundamental linewidth of defect PL to demonstrate indistinguishability of defect PL.

Furthermore, the enhanced optical properties and new functionality by fluorescent quantum defects benefit the numerous applications of SWCNTs such as molecular-scale optoelectronic device,[123] optical sensing,[45] and bioimaging.[12] For the

use of defect-tailored SWCNT in optoelectronics, one should test the electrical gating of defect-tailored SWCNT to induce electroluminescence at fluorescent defects. Preparation of long, defect-free SWCNTs and selective separation of by SWCNT structure[27,30] would allow the fabrication of single tube device with greatly enhanced electroluminescence efficiency at the defect sites. For the biological sensing and imaging, the stability and biocompatibility of the functionalized SWCNTs are key factors to be optimized. Non-covalent wrapping of SWCNTs by biocompatible polymer or DNA resolves these issues for the unfunctionalized SWCNTs.[12,58] However, re-wrapping the functionalized SWCNTs to polymer or DNA is generally low-yield in our preliminary experiments. Thus, it is important to find the effective way to disperse the functionalized SWCNTs in biological media, retaining the desired functionality at high brightness.

Bibliography

1. Radushkevich L.V., L. V. M., O strukture ugleroda, obrazujucegosja pri termiceskom razlozenii okisi ugleroda na zeleznom kontakte (about the structure of carbon formed by thermal decomposition of carbon monoxide on iron substrate). *Zurn. Fisic. Chim.* **1952**, *26*, 88-95.
2. Iijima, S., Helical microtubules of graphitic carbon. *Nature* **1991**, *354*, 56.
3. Ebbesen, T. W.; Ajayan, P. M., Large-scale synthesis of carbon nanotubes. *Nature* **1992**, *358*, 220.
4. Berber, S.; Kwon, Y.-K.; Tománek, D., Unusually high thermal conductivity of carbon nanotubes. *Phys. Rev. Lett.* **2000**, *84*, 4613-4616.
5. Bethune, D. S.; Kiang, C. H.; de Vries, M. S.; Gorman, G.; Savoy, R.; Vazquez, J.; Beyers, R., Cobalt-catalysed growth of carbon nanotubes with single-atomic-layer walls. *Nature* **1993**, *363*, 605.
6. Iijima, S.; Ichihashi, T., Single-shell carbon nanotubes of 1-nm diameter. *Nature* **1993**, *363*, 603.
7. Bockrath, M.; Cobden, D. H.; Lu, J.; Rinzler, A. G.; Smalley, R. E.; Balents, L.; McEuen, P. L., Luttinger-liquid behaviour in carbon nanotubes. *Nature* **1999**, *397*, 598.
8. Dukovic, G.; Wang, F.; Song, D.; Sfeir, M. Y.; Heinz, T. F.; Brus, L. E., Structural dependence of excitonic optical transitions and band-gap energies in carbon nanotubes. *Nano Lett.* **2005**, *5*, 2314-2318.
9. Wang, F.; Dukovic, G.; Brus, L. E.; Heinz, T. F., The optical resonances in carbon nanotubes arise from excitons. *Science* **2005**, *308*, 838.

10. O'Connell, M. J.; Bachilo, S. M.; Huffman, C. B.; Moore, V. C.; Strano, M. S.; Haroz, E. H.; Rialon, K. L.; Boul, P. J.; Noon, W. H.; Kittrell, C.; Ma, J.; Hauge, R. H.; Weisman, R. B.; Smalley, R. E., Band gap fluorescence from individual single-walled carbon nanotubes. *Science* **2002**, *297*, 593-596.

11. Högele, A.; Galland, C.; Winger, M.; Imamoğlu, A., Photon antibunching in the photoluminescence spectra of a single carbon nanotube. *Phys. Rev. Lett.* **2008**, *100*, 217401.

12. Hong, G.; Diao, S.; Antaris, A. L.; Dai, H., Carbon nanomaterials for biological imaging and nanomedicinal therapy. *Chem. Rev.* **2015**, *115*, 10816-10906.

13. Zhang, Y.; Valley, N.; Brozena, A. H.; Piao, Y.; Song, X.; Schatz, G. C.; Wang, Y., Propagative sidewall alkylcarboxylation that induces red-shifted near-IR photoluminescence in single-walled carbon nanotubes. *J. Phys. Chem. Lett.* **2013**, *4*, 826-830.

14. Piao, Y.; Meany, B.; Powell, L. R.; Valley, N.; Kwon, H.; Schatz, G. C.; Wang, Y., Brightening of carbon nanotube photoluminescence through the incorporation of sp^3 defects. *Nat. Chem.* **2013**, *5*, 840-845.

15. Kwon, H.; Furmanchuk, A.; Kim, M.; Meany, B.; Guo, Y.; Schatz, G. C.; Wang, Y., Molecularly tunable fluorescent quantum defects. *J. Am. Chem. Soc.* **2016**, *138*, 6878-6885.

16. Saito, R.; Dresselhaus, G.; Dresselhaus, M. S., Trigonal warping effect of carbon nanotubes. *Phys. Rev. B* **2000**, *61*, 2981-2990.

17. Manzoni, C.; Gambetta, A.; Menna, E.; Meneghetti, M.; Lanzani, G.; Cerullo, G., Intersubband exciton relaxation dynamics in single-walled carbon nanotubes. *Phys. Rev. Lett.* **2005**, *94*, 207401.

18. Zhao, H.; Mazumdar, S., Electron-electron interaction effects on the optical excitations of semiconducting single-walled carbon nanotubes. *Phys. Rev. Lett.* **2004**, *93*, 157402.

19. Ando, T., Effects of valley mixing and exchange on excitons in carbon nanotubes with Aharonov–Bohm flux. *J. Phys. Soc. Jpn.* **2006**, *75*, 024707.

20. Spataru, C. D.; Ismail-Beigi, S.; Capaz, R. B.; Louie, S. G., Theory and ab initio calculation of radiative lifetime of excitons in semiconducting carbon nanotubes. *Phys. Rev. Lett.* **2005**, *95*, 247402.

21. Capaz, R. B.; Spataru, C. D.; Ismail-Beigi, S.; Louie, S. G., Diameter and chirality dependence of exciton properties in carbon nanotubes. *Phys. Rev. B* **2006**, *74*, 121401.

22. Perebeinos, V.; Tersoff, J.; Avouris, P., Effect of exciton-phonon coupling in the calculated optical absorption of carbon nanotubes. *Phys. Rev. Lett.* **2005**, *94*, 027402.

23. Torrens, O. N.; Zheng, M.; Kikkawa, J. M., Energy of *K*-momentum dark excitons in carbon nanotubes by optical spectroscopy. *Phys. Rev. Lett.* **2008**, *101*, 157401.

24. Chou, S. G.; Plentz, F.; Jiang, J.; Saito, R.; Nezich, D.; Ribeiro, H. B.; Jorio, A.; Pimenta, M. A.; Samsonidze, G. G.; Santos, A. P.; Zheng, M.; Onoa, G. B.; Semke, E. D.; Dresselhaus, G.; Dresselhaus, M. S., Phonon-assisted excitonic

recombination channels observed in DNA-wrapped carbon nanotubes using photoluminescence spectroscopy. *Phys. Rev. Lett.* **2005**, *94*, 127402.

25. Subbaiyan, N. K.; Parra-Vasquez, A. N. G.; Cambré, S.; Cordoba, M. A. S.; Yalcin, S. E.; Hamilton, C. E.; Mack, N. H.; Blackburn, J. L.; Doorn, S. K.; Duque, J. G., Bench-top aqueous two-phase extraction of isolated individual single-walled carbon nanotubes. *Nano Res.* **2015**, *8*, 1755-1769.

26. Graf, A.; Zakharko, Y.; Schießl, S. P.; Backes, C.; Pfohl, M.; Flavel, B. S.; Zaumseil, J., Large scale, selective dispersion of long single-walled carbon nanotubes with high photoluminescence quantum yield by shear force mixing. *Carbon* **2016**, *105*, 593-599.

27. Wang, P.; Kim, M.; Peng, Z.; Sun, C.-F.; Mok, J.; Lieberman, A.; Wang, Y., Superacid-surfactant exchange: Enabling nondestructive dispersion of full-length carbon nanotubes in water. *ACS Nano* **2017**, *11*, 9231-9238.

28. Liu, H.; Nishide, D.; Tanaka, T.; Kataura, H., Large-scale single-chirality separation of single-wall carbon nanotubes by simple gel chromatography. *Nat. Commun.* **2011**, *2*, 309.

29. Ao, G.; Streit, J. K.; Fagan, J. A.; Zheng, M., Differentiating left- and right-handed carbon nanotubes by DNA. *J. Am. Chem. Soc.* **2016**, *138*, 16677-16685.

30. Subbaiyan, N. K.; Cambré, S.; Parra-Vasquez, A. N. G.; Hároz, E. H.; Doorn, S. K.; Duque, J. G., Role of surfactants and salt in aqueous two-phase separation of carbon nanotubes toward simple chirality isolation. *ACS Nano* **2014**, *8*, 1619-1628.

31. Jorio, A.; Saito, R.; Hafner, J. H.; Lieber, C. M.; Hunter, M.; McClure, T.; Dresselhaus, G.; Dresselhaus, M. S., Structural (*n*,*m*) determination of isolated single-wall carbon nanotubes by resonant raman scattering. *Phys. Rev. Lett.* **2001**, *86*, 1118-1121.

32. Dresselhaus, M. S.; Dresselhaus, G.; Saito, R.; Jorio, A., Raman spectroscopy of carbon nanotubes. *Phys. Rep.* **2005**, *409*, 47-99.

33. Telg, H.; Fouquet, M.; Maultzsch, J.; Wu, Y.; Chandra, B.; Hone, J.; Heinz, T. F.; Thomsen, C., G– and G+ in the raman spectrum of isolated nanotube: A study on resonance conditions and lineshape. *Phys. Status Solidi B* **2008**, *245*, 2189-2192.

34. Powell, L. R.; Kim, M.; Wang, Y., Chirality-selective functionalization of semiconducting carbon nanotubes with a reactivity-switchable molecule. *J. Am. Chem. Soc.* **2017**, *139*, 12533-12540.

35. Wu, X.; Kim, M.; Kwon, H.; Wang, Y., Photochemical creation of fluorescent quantum defects in semiconducting carbon nanotube hosts. *Angew. Chem. Int. Ed.* **2018**, *57*, 648-653.

36. Hertel, T.; Himmelein, S.; Ackermann, T.; Stich, D.; Crochet, J., Diffusion limited photoluminescence quantum yields in 1-d semiconductors: Single-wall carbon nanotubes. *ACS Nano* **2010**, *4*, 7161-7168.

37. Miyauchi, Y.; Iwamura, M.; Mouri, S.; Kawazoe, T.; Ohtsu, M.; Matsuda, K., Brightening of excitons in carbon nanotubes on dimensionality modification. *Nat. Photon.* **2013**, *7*, 715-719.

38. Crochet, J. J.; Duque, J. G.; Werner, J. H.; Lounis, B.; Cognet, L.; Doorn, S. K., Disorder limited exciton transport in colloidal single-wall carbon nanotubes. *Nano Lett.* **2012**, *12*, 5091-5096.

39. Singh, P.; Campidelli, S.; Giordani, S.; Bonifazi, D.; Bianco, A.; Prato, M., Organic functionalisation and characterisation of single-walled carbon nanotubes. *Chem. Soc. Rev.* **2009**, *38*, 2214-2230.

40. Liang, F.; Sadana, A. K.; Peera, A.; Chattopadhyay, J.; Gu, Z.; Hauge, R. H.; Billups, W. E., A convenient route to functionalized carbon nanotubes. *Nano Lett.* **2004**, *4*, 1257-1260.

41. Deng, S.; Zhang, Y.; Brozena, A. H.; Mayes, M. L.; Banerjee, P.; Chiou, W.-A.; Rubloff, G. W.; Schatz, G. C.; Wang, Y., Confined propagation of covalent chemical reactions on single-walled carbon nanotubes. *Nat. Commun.* **2011**, *2*, 382.

42. Strano, M. S.; Dyke, C. A.; Usrey, M. L.; Barone, P. W.; Allen, M. J.; Shan, H.; Kittrell, C.; Hauge, R. H.; Tour, J. M.; Smalley, R. E., Electronic structure control of single-walled carbon nanotube functionalization. *Science* **2003**, *301*, 1519.

43. Cognet, L.; Tsyboulski, D. A.; Rocha, J. D.; Doyle, C. D.; Tour, J. M.; Weisman, R. B., Stepwise quenching of exciton fluorescence in carbon nanotubes by single-molecule reactions. *Science* **2007**, *316*, 1465-1468.

44. Usrey, M. L.; Lippmann, E. S.; Strano, M. S., Evidence for a two-step mechanism in electronically selective single-walled carbon nanotube reactions. *J. Am. Chem. Soc.* **2005**, *127*, 16129-16135.

45. Kwon, H.; Kim, M.; Meany, B.; Piao, Y.; Powell, L. R.; Wang, Y., Optical probing of local ph and temperature in complex fluids with covalently functionalized, semiconducting carbon nanotubes. *J. Phys. Chem. C* **2015**, *119*, 3733-3739.

46. Dickson, R. M.; Cubitt, A. B.; Tsien, R. Y.; Moerner, W. E., On/off blinking and switching behaviour of single molecules of green fluorescent protein. *Nature* **1997**, *388*, 355.

47. Barone, P. W.; Baik, S.; Heller, D. A.; Strano, M. S., Near-infrared optical sensors based on single-walled carbon nanotubes. *Nat. Mater.* **2004**, *4*, 86.

48. He, X.; Hartmann, N. F.; Ma, X.; Kim, Y.; Ihly, R.; Blackburn, J. L.; Gao, W.; Kono, J.; Yomogida, Y.; Hirano, A.; Tanaka, T.; Kataura, H.; Htoon, H.; Doorn, S. K., Tunable room-temperature single-photon emission at telecom wavelengths from sp^3 defects in carbon nanotubes. *Nat. Photon.* **2017**, *11*, 577-582.

49. Srinivasan, K.; Zheng, M., Nanotube chemistry tunes light. *Nat. Photon.* **2017**, *11*, 535-537.

50. Cognet, L.; Tsyboulski, D. A.; Weisman, R. B., Subdiffraction far-field imaging of luminescent single-walled carbon nanotubes. *Nano Lett.* **2008**, *8*, 749-753.

51. Shiraki, T.; Onitsuka, H.; Shiraishi, T.; Nakashima, N., Near infrared photoluminescence modulation of single-walled carbon nanotubes based on a molecular recognition approach. *Chem. Commun.* **2016**, *52*, 12972-12975.

52. Shiraki, T.; Shiraishi, T.; Juhasz, G.; Nakashima, N., Emergence of new red-shifted carbon nanotube photoluminescence based on proximal doped-site design. *Sci. Rep.* **2016**, *6*, 28393.

53. Powell, L. R.; Piao, Y.; Wang, Y., Optical excitation of carbon nanotubes drives localized diazonium reactions. *J. Phys. Chem. Lett.* **2016**, *7*, 3690-3694.

54. Delgado, J. L.; de la Cruz, P.; Langa, F.; Urbina, A.; Casado, J.; Lopez Navarrete, J. T., Microwave-assisted sidewall functionalization of single-wall carbon nanotubes by diels-alder cycloaddition. *Chem. Commun.* **2004**, 1734-1735.

55. Bachilo, S. M.; Strano, M. S.; Kittrell, C.; Hauge, R. H.; Smalley, R. E.; Weisman, R. B., Structure-assigned optical spectra of single-walled carbon nanotubes. *Science* **2002**, *298*, 2361-2366.

56. Kataura, H.; Kumazawa, Y.; Maniwa, Y.; Umezu, I.; Suzuki, S.; Ohtsuka, Y.; Achiba, Y., Optical properties of single-wall carbon nanotubes. *Synth. Met.* **1999**, *103*, 2555-2558.

57. Hartmann, N. F.; Velizhanin, K. A.; Haroz, E. H.; Kim, M.; Ma, X.; Wang, Y.; Htoon, H.; Doorn, S. K., Photoluminescence dynamics of aryl sp^3 defect states in single-walled carbon nanotubes. *ACS Nano* **2016**, *10*, 8355-8365.

58. Godin, A. G.; Varela, J. A.; Gao, Z.; Danné, N.; Dupuis, J. P.; Lounis, B.; Groc, L.; Cognet, L., Single-nanotube tracking reveals the nanoscale organization of the extracellular space in the live brain. *Nat. Nanotech.* **2016**, *12*, 238-243.

59. Dresselhaus, M. S.; Dresselhaus, G.; Saito, R., Carbon fibers based on c_{60} and their symmetry. *Phys. Rev. B* **1992**, *45*, 6234-6242.

60. Kim, M.; Adamska, L.; Hartmann, N. F.; Kwon, H.; Liu, J.; Velizhanin, K. A.; Piao, Y.; Powell, L. R.; Meany, B.; Doorn, S. K.; Tretiak, S.; Wang, Y., Fluorescent carbon nanotube defects manifest substantial vibrational reorganization. *J. Phys. Chem. C* **2016**, *120*, 11268-11276.

61. Danné, N.; Kim, M.; Godin, A. G.; Kwon, H.; Gao, Z.; Wu, X.; Hartmann, N. F.; Doorn, S. K.; Lounis, B.; Wang, Y.; Cognet, L., Ultrashort carbon nanotubes that fluoresce brightly in the near-infrared. *ACS Nano* **2018**, *12*, 6059-6065.

62. Hartmann, N. F.; Yalcin, S. E.; Adamska, L.; Haroz, E. H.; Ma, X.; Tretiak, S.; Htoon, H.; Doorn, S. K., Photoluminescence imaging of solitary dopant sites in covalently doped single-wall carbon nanotubes. *Nanoscale* **2015**, *7*, 20521-20530.

63. Takagahara, T.; Hanamura, E., Giant-oscillator-strength effect on excitonic optical nonlinearities due to localization. *Phys. Rev. Lett.* **1986**, *56*, 2533-2536.

64. Charton, M., The application of the hammett equation to ortho-substituted benzene reaction series. *Can. J. Chem.* **1960**, *38*, 2493-2499.

65. Artem, R. C.; Vladimir, I. G.; Rafael, A. C., The problem of the quantitative evaluation of the inductive effect: Correlation analysis. *Russ. Chem. Rev.* **1996**, *65*, 641.

66. Iwamura, M.; Akizuki, N.; Miyauchi, Y.; Mouri, S.; Shaver, J.; Gao, Z.; Cognet, L.; Lounis, B.; Matsuda, K., Nonlinear photoluminescence spectroscopy of carbon nanotubes with localized exciton states. *ACS Nano* **2014**, *8*, 11254-11260.

67. Ohfuchi, M., Ab initio study on oxygen doping of (5,4), (6,4), (6,5), and (8,6) carbon nanotubes. *J. Phys. Chem. C* **2015**, *119*, 13200-13206.

68. Shiraishi, T.; Juhász, G.; Shiraki, T.; Akizuki, N.; Miyauchi, Y.; Matsuda, K.; Nakashima, N., Determination of precise redox properties of oxygen-doped single-walled carbon nanotubes based on in situ photoluminescence electrochemistry. *J. Phys. Chem. C* **2015**.

69. Brozena, A. H.; Leeds, J. D.; Zhang, Y.; Fourkas, J. T.; Wang, Y., Controlled defects in semiconducting carbon nanotubes promote efficient generation and luminescence of trions. *ACS Nano* **2014**, *8*, 4239-4247.

70. Ma, X.; Adamska, L.; Yamaguchi, H.; Yalcin, S. E.; Tretiak, S.; Doorn, S. K.; Htoon, H., Electronic structure and chemical nature of oxygen dopant states in carbon nanotubes. *ACS Nano* **2014**, *8*, 10782-10789.

71. Ghosh, S.; Bachilo, S. M.; Simonette, R. A.; Beckingham, K. M.; Weisman, R. B., Oxygen doping modifies near-infrared band gaps in fluorescent single-walled carbon nanotubes. *Science* **2010**, *330*, 1656-1659.

72. Akizuki, N.; Aota, S.; Mouri, S.; Matsuda, K.; Miyauchi, Y., Efficient near-infrared up-conversion photoluminescence in carbon nanotubes. *Nat. Commun.* **2015**, *6*, 8920.

73. Frisch, M. J. T., G. W.; Schlegel, H. B.; Scuseria, G. E.; Robb, M. A.; Cheeseman, J. R.; Scalmani, G.; Barone, V.; Mennucci, B.; Petersson, G. A.; et al. *Gaussian 09*, Gaussian, Inc.: Wallingford, CT, 2009.

74. Yanai, T.; Tew, D. P.; Handy, N. C., A new hybrid exchange–correlation functional using the Coulomb-attenuating method (CAM-B3LYP). *Chem. Phys. Lett.* **2004**, *393*, 51-57.

75. Cossi, M.; Rega, N.; Scalmani, G.; Barone, V., Energies, structures, and electronic properties of molecules in solution with the c-pcm solvation model. *J. Comput. Chem.* **2003**, *24*, 669-681.

76. Blakemore, J. S., *Semiconductor statistics*. Pergamon Press: Oxford, UK, 1962.

77. Andersen, O. K.; Veje, E., Experimental study of the energy-band structure of porous silicon. *Phys. Rev. B* **1996**, *53*, 15643-15652.

78. Mouri, S.; Miyauchi, Y.; Iwamura, M.; Matsuda, K., Temperature dependence of photoluminescence spectra in hole-doped single-walled carbon nanotubes: Implications of trion localization. *Phys. Rev. B* **2013**, *87*, 045408.

79. Perebeinos, V.; Tersoff, J.; Avouris, P., Radiative lifetime of excitons in carbon nanotubes. *Nano Lett.* **2005**, *5*, 2495-2499.

80. Berciaud, S.; Cognet, L.; Lounis, B., Luminescence decay and the absorption cross section of individual single-walled carbon nanotubes. *Phys. Rev. Lett.* **2008**, *101*, 077402.

81. Matsunaga, R.; Miyauchi, Y.; Matsuda, K.; Kanemitsu, Y., Symmetry-induced nonequilibrium distributions of bright and dark exciton states in single carbon nanotubes. *Phys. Rev. B* **2009**, *80*, 115436.

82. Graham, M. W.; Ma, Y.-Z.; Green, A. A.; Hersam, M. C.; Fleming, G. R., Pure optical dephasing dynamics in semiconducting single-walled carbon nanotubes. *J. Chem. Phys.* **2011**, *134*, 034504.

83. Schilling, D.; Mann, C.; Kunkel, P.; Schöppler, F.; Hertel, T., Ultrafast spectral exciton diffusion in single-wall carbon nanotubes studied by time-resolved hole burning. *J. Phys. Chem. C* **2015**, *119*, 24116-24123.

84. Hansch, C.; Leo, A.; Taft, R. W., A survey of Hammett substituent constants and resonance and field parameters. *Chem. Rev.* **1991**, *91*, 165-195.

85. Hammouda, B., Temperature effect on the nanostructure of sds micelles in water. *J. Res. Natl. Inst. Stand. Technol.* **2013**, *118*, 151-167.

86. Niyogi, S.; Densmore, C. G.; Doorn, S. K., Electrolyte tuning of surfactant interfacial behavior for enhanced density-based separations of single-walled carbon nanotubes. *J. Am. Chem. Soc.* **2009**, *131*, 1144-1153.

87. Siitonen, A. J.; Tsyboulski, D. A.; Bachilo, S. M.; Weisman, R. B., Surfactant-dependent exciton mobility in single-walled carbon nanotubes studied by single-molecule reactions. *Nano Lett.* **2010**, *10*, 1595-1599.

88. Lain-Jong, L.; Nicholas, R. J.; Chien-Yen, C.; Darton, R. C.; Baker, S. C., Comparative study of photoluminescence of single-walled carbon nanotubes wrapped with sodium dodecyl sulfate, surfactin and polyvinylpyrrolidone. *Nanotechnology* **2005**, *16*, S202.

89. Duque, J. G.; Chen, H.; Swan, A. K.; Shreve, A. P.; Kilina, S.; Tretiak, S.; Tu, X.; Zheng, M.; Doorn, S. K., Violation of the Condon approximation in semiconducting carbon nanotubes. *ACS Nano* **2011**, *5*, 5233-5241.

90. Jones, M.; Engtrakul, C.; Metzger, W. K.; Ellingson, R. J.; Nozik, A. J.; Heben, M. J.; Rumbles, G., Analysis of photoluminescence from solubilized single-walled carbon nanotubes. *Phys. Rev. B* **2005**, *71*, 115426.

91. Shreve, A. P.; Haroz, E. H.; Bachilo, S. M.; Weisman, R. B.; Tretiak, S.; Kilina, S.; Doorn, S. K., Determination of exciton-phonon coupling elements in single-walled carbon nanotubes by Raman overtone analysis. *Phys. Rev. Lett.* **2007**, *98*, 037405.

92. Kilina, S.; Ramirez, J.; Tretiak, S., Brightening of the lowest exciton in carbon nanotubes via chemical functionalization. *Nano Lett.* **2012**, *12*, 2306-2312.

93. Ramirez, J.; Mayo, M. L.; Kilina, S.; Tretiak, S., Electronic structure and optical spectra of semiconducting carbon nanotubes functionalized by diazonium salts. *Chem. Phys.* **2013**, *413*, 89-101.

94. Ma, X.; Hartmann, N. F.; BaldwinJon, K. S.; Doorn, S. K.; Htoon, H., Room-temperature single-photon generation from solitary dopants of carbon nanotubes. *Nat Nanotech.* **2015**, *10*, 671-675.

95. Ma, X.; Baldwin, J. K. S.; Hartmann, N. F.; Doorn, S. K.; Htoon, H., Solid-state approach for fabrication of photostable, oxygen-doped carbon nanotubes. *Adv. Func. Mater.* **2015**, *25*, 6157-6164.

96. Nagashima, Y., Experiments on positronium negative ions. *Phys. Rep.* **2014**, *545*, 95-123.

97. De Greve, K.; Yu, L.; McMahon, P. L.; Pelc, J. S.; Natarajan, C. M.; Kim, N. Y.; Abe, E.; Maier, S.; Schneider, C.; Kamp, M.; Hofling, S.; Hadfield, R. H.; Forchel, A.; Fejer, M. M.; Yamamoto, Y., Quantum-dot spin-photon entanglement via frequency downconversion to telecom wavelength. *Nature* **2012**, *491*, 421-425.

98. Brinkmann, D.; Kudrna, J.; Gilliot, P.; Hönerlage, B.; Arnoult, A.; Cibert, J.; Tatarenko, S., Trion and exciton dephasing measurements in modulation-doped quantum wells: A probe for trion and carrier localization. *Phys. Rev. B* **1999**, *60*, 4474-4477.

99. Watanabe, K.; Asano, K., Trions in semiconducting single-walled carbon nanotubes. *Phys. Rev. B* **2012**, *85*, 035416.

100. Patton, B.; Langbein, W.; Woggon, U., Trion, biexciton, and exciton dynamics in single self-assembled CdSe quantum dots. *Phys. Rev. B* **2003**, *68*, 125316.

101. Puls, J. M., G. V.; Henneberger, F.; Yakovlev, D. R.; Waag, A.; Faschinger, W., Laser action of trions in a semiconductor quantum well. *Phys. Rev. Lett.* **2002**, *89*, 287402.

102. Zhang, Y. J.; Oka, T.; Suzuki, R.; Ye, J. T.; Iwasa, Y., Electrically switchable chiral light-emitting transistor. *Science* **2014**, *344*, 725.

103. Lampert, M. A., Mobile and immobile effective-mass-particle complexes in nonmetallic solids. *Phys. Rev. Lett.* **1958**, *1*, 450-453.

104. Bracker, A. S.; Stinaff, E. A.; Gammon, D.; Ware, M. E.; Tischler, J. G.; Park, D.; Gershoni, D.; Filinov, A. V.; Bonitz, M.; Peeters, F.; Riva, C., Binding energies of positive and negative trions: From quantum wells to quantum dots. *Phys. Rev. B* **2005**, *72*, 035332.

105. Rønnow, T. F.; Pedersen, T. G.; Cornean, H. D., Correlation and dimensional effects of trions in carbon nanotubes. *Phys. Rev. B* **2010**, *81*, 205446.

106. Santos, S. M.; Yuma, B.; Berciaud, S.; Shaver, J.; Gallart, M.; Gilliot, P.; Cognet, L.; Lounis, B., All-optical trion generation in single-walled carbon nanotubes. *Phys. Rev. Lett.* **2011**, *107*, 187401.

107. Yuma, B.; Berciaud, S.; Besbas, J.; Shaver, J.; Santos, S.; Ghosh, S.; Weisman, R. B.; Cognet, L.; Gallart, M.; Ziegler, M.; Hönerlage, B.; Lounis, B.; Gilliot, P., Biexciton, single carrier, and trion generation dynamics in single-walled carbon nanotubes. *Phys. Rev. B* **2013**, *87*, 205412.

108. Park, J. S.; Hirana, Y.; Mouri, S.; Miyauchi, Y.; Nakashima, N.; Matsuda, K., Observation of negative and positive trions in the electrochemically carrier-doped single-walled carbon nanotubes. *J. Am. Chem. Soc.* **2012**, *134*, 14461-14466.

109. Jakubka, F.; Grimm, S. B.; Zakharko, Y.; Gannott, F.; Zaumseil, J., Trion electroluminescence from semiconducting carbon nanotubes. *ACS Nano* **2014**, *8*, 8477-8486.

110. Koyama, T.; Shimizu, S.; Miyata, Y.; Shinohara, H.; Nakamura, A., Ultrafast formation and decay dynamics of trions in *p*-doped single-walled carbon nanotubes. *Phys. Rev. B* **2013**, *87*, 165430.

111. Matsunaga, R.; Matsuda, K.; Kanemitsu, Y., Observation of charged excitons in hole-doped carbon nanotubes using photoluminescence and absorption spectroscopy. *Phys. Rev. Lett.* **2011**, *106*, 037404.

112. Zhang, D. K.; Kidd, D. W.; Varga, K., Excited biexcitons in transition metal dichalcogenides. *Nano Lett.* **2015**, *15*, 7002-7005.

113. Zheng, M.; Diner, B. A., Solution redox chemistry of carbon nanotubes. *J. Am. Chem. Soc.* **2004**, *126*, 15490-15494.

114. Liu, T.; Xiao, Z., Exact and closed form solutions for the quantum yield, exciton diffusion length, and lifetime to reveal the universal behaviors of the photoluminescence of defective single-walled carbon nanotubes. *J. Phys. Chem. C* **2011**, *115*, 16920-16927.

115. Crochet, J. J.; Duque, J. G.; Werner, J. H.; Doorn, S. K., Photoluminescence imaging of electronic-impurity-induced exciton quenching in single-walled carbon nanotubes. *Nat. Nanotech.* **2012**, *7*, 126-132.

116. Nishihara, T.; Yamada, Y.; Okano, M.; Kanemitsu, Y., Trion formation and recombination dynamics in hole-doped single-walled carbon nanotubes. *Appl. Phys. Lett.* **2013**, *103*, 023101.

117. Barros, E. B.; Capaz, R. B.; Jorio, A.; Samsonidze, G. G.; Souza Filho, A. G.; Ismail-Beigi, S.; Spataru, C. D.; Louie, S. G.; Dresselhaus, G.; Dresselhaus, M. S., Selection rules for one- and two-photon absorption by excitons in carbon nanotubes. *Phys. Rev. B* **2006**, *73*, 241406.

118. Shaver, J.; Kono, J., Temperature-dependent magneto-photoluminescence spectroscopy of carbon nanotubes: Evidence for dark excitons. *Laser Photon. Rev.* **2007**, *1*, 260-274.

119. Srivastava, A.; Htoon, H.; Klimov, V. I.; Kono, J., Direct observation of dark excitons in individual carbon nanotubes: Inhomogeneity in the exchange splitting. *Phys. Rev. Lett.* **2008**, *101*, 087402.

120. Bondarev, I. V., Relative stability of excitonic complexes in quasi-one-dimensional semiconductors. *Phys. Rev. B* **2014**, *90*, 245430.

121. Cherkasov, A. R.; Galkin, V. I.; Cherkasov, R. A., The problem of the quantitative evaluation of the inductive effect: Correlation analysis. *Russ. Chem. Rev.* **1996**, *65*, 641-656.

122. Heller, D. A.; Jeng, E. S.; Yeung, T.-K.; Martinez, B. M.; Moll, A. E.; Gastala, J. B.; Strano, M. S., Optical detection of DNA conformational polymorphism on single-walled carbon nanotubes. *Science* **2006**, *311*, 508.

123. Avouris, P.; Freitag, M.; Perebeinos, V., Carbon-nanotube photonics and optoelectronics. *Nat. Photon.* **2008**, *2*, 341.

124. Lee, A. J.; Wang, X.; Carlson, L. J.; Smyder, J. A.; Loesch, B.; Tu, X.; Zheng, M.; Krauss, T. D., Bright fluorescence from individual single-walled carbon nanotubes. *Nano Lett.* **2011**, *11*, 1636-1640.

125. Tomio, Y.; Suzuura, H., Impurity-induced valley mixing of excitons in semiconducting carbon nanotubes. *Physica E: Low-dimensional Systems and Nanostructures* **2010**, *42*, 783-786.

126. Ju, S. Y.; Kopcha, W. P.; Papadimitrakopoulos, F., Brightly fluorescent single-walled carbon nanotubes via an oxygen-excluding surfactant organization. *Science* **2009**, *323*, 1319-1323.

127. Lefebvre, J.; Austing, D. G.; Bond, J.; Finnie, P., Photoluminescence imaging of suspended single-walled carbon nanotubes. *Nano Lett.* **2006**, *6*, 1603-1608.

128. Shaver, J.; Kono, J.; Portugall, O.; Krstić, V.; Rikken, G. L. J. A.; Miyauchi, Y.; Maruyama, S.; Perebeinos, V., Magnetic brightening of carbon nanotube

photoluminescence through symmetry breaking. *Nano Lett.* **2007**, *7*, 1851-1855.

129. Ai, N.; Walden-Newman, W.; Song, Q.; Kalliakos, S.; Strauf, S., Suppression of blinking and enhanced exciton emission from individual carbon nanotubes. *ACS Nano* **2011**, *5*, 2664-2670.

130. Walden-Newman, W.; Sarpkaya, I.; Strauf, S., Quantum light signatures and nanosecond spectral diffusion from cavity-embedded carbon nanotubes. *Nano Lett.* **2012**, *12*, 1934-1941.

131. Betzig, E.; Patterson, G. H.; Sougrat, R.; Lindwasser, O. W.; Olenych, S.; Bonifacino, J. S.; Davidson, M. W.; Lippincott-Schwartz, J.; Hess, H. F., Imaging intracellular fluorescent proteins at nanometer resolution. *Science* **2006**, *313*, 1642.

132. Rust, M. J.; Bates, M.; Zhuang, X., Sub-diffraction-limit imaging by stochastic optical reconstruction microscopy (STORM). *Nat. Methods* **2006**, *3*, 793-795.

133. Möckl, L.; Lamb, D. C.; Bräuchle, C., Super-resolved fluorescence microscopy: Nobel prize in chemistry 2014 for eric betzig, stefan hell, and william e. Moerner. *Angew. Chem. Int. Ed.* **2014**, *53*, 13972-13977.

134. Siitonen, A. J.; Bachilo, S. M.; Tsyboulski, D. A.; Weisman, R. B., Evidence for long-lived, optically generated quenchers of excitons in single-walled carbon nanotubes. *Nano Lett.* **2012**, *12*, 33-38.

135. Ma, X.; Hartmann, N. F.; Velizhanin, K. A.; Baldwin, J. K. S.; Adamska, L.; Tretiak, S.; Doorn, S. K.; Htoon, H., Multi-exciton emission from solitary dopant states of carbon nanotubes. *Nanoscale* **2017**, *9*, 16143-16148.

136. Sanchez, S. R.; Bachilo, S. M.; Kadria-Vili, Y.; Lin, C. W.; Weisman, R. B., (*n*,*m*)-specific absorption cross sections of single-walled carbon nanotubes measured by variance spectroscopy. *Nano Lett.* **2016**, *16*, 6903-6909.

137. Citrin, D. S., Long intrinsic radiative lifetimes of excitons in quantum wires. *Phys. Rev. Lett.* **1992**, *69*, 3393-3396.

138. Shaver, J.; Crooker, S. A.; Fagan, J. A.; Hobbie, E. K.; Ubrig, N.; Portugall, O.; Perebeinos, V.; Avouris, P.; Kono, J., Magneto-optical spectroscopy of highly aligned carbon nanotubes: Identifying the role of threading magnetic flux. *Phys. Rev. B* **2008**, *78*, 081402.

139. Jiang, J.; Saito, R.; Samsonidze, G. G.; Jorio, A.; Chou, S. G.; Dresselhaus, G.; Dresselhaus, M. S., Chirality dependence of exciton effects in single-wall carbon nanotubes: Tight-binding model. *Phys. Rev. B* **2007**, *75*, 035407.